PhD School in Earth, Environment and Resources Sciences

- XXXI Cycle -

PhD Thesis

MULTISCALE INVERSION OF POTENTIAL FIELDS: FROM 1D TO 3D DEPTH-WEIGHTED MODELS

Andrea Vitale

Advisor	**PhD Coordinator**
Prof. M. Fedi	*Prof.* M. Fedi

2019

TABLE OF CONTENTS

SUMMARY **2**

INTRODUCTION **2**

1. ELEMENTS OF POTENTIAL FIELDS THEORY **5**

1.1. Gravity field 5
1.2. Magnetic field 7
1.3. Scaled field and homogeneity law 10

2. ELEMENTS OF INVERSION THEORY **14**

2.1. Depth Weighting Function 16

3. [PAPERS] METHODS FOR 1D INVERSION OF POTENTIAL FIELD **21**

4. IMAGING METHODS: THE SCALING FUNCTION **40**

4.1. Estimating the inhomogeneous depth weighting exponent *b* .. 42

5. 2D INVERSION WITH INHOMOGENEOUS DEPTH WEIGHTING FUNCTION **45**

5.1. 2D horizontal line of dipoles 45
5.2. 2D Single buried body (prismatic source) 47
5.3. Two-body sources 50

6. 3D INVERSION WITH INHOMOGENEOUS DEPTH WEIGHTING FUNCTION **55**

6.1. Polygonal source 55
6.2. Two buried bodies: a prismatic source and a source like a vertical intrusion 61
6.3. Real case: Vredefort impact site 66
6.4. Real case: Mt. Vulture (Southern Italy) 74

7. CONCLUSIONS **80**

ACKNOWLEDGEMENTS **83**

APPENDIX A **84**

REFERENCES **86**

Summary

We developed two different approaches of inversion of potential fields:

- A method for 1D inversion of potential fields.

- A method for 2D and 3D self-constrained depth weighted inversion of inhomogeneous potential fields.

Both methods are based on a multiscale approach, that is they involve use of data at different scales or altitudes. These particular approaches bring some benefits.

About the 1D method, the main benefit lies in a greater computationally simplicity, compared to 3D algorithms.

Apart the strong 1D assumption, we can say that it requires less a priori information to constrain the inversion, compared to other algorithms. (see Chapter 3).

The second method is both 2D and 3D. It is based on two steps, the first being the search in the 3D domain of the homogenous degree of the field, and the second being the inversion of the data using a power-law weighting function with a 3D variable exponent. So, differently from the previous method it does not involve directly data at different altitudes, but it is heavily conditioned by a multiscale search of the homogeneity degree.

The main difference between the present approach and the one proposed by Li and Oldenburg algorithm (1996) and Cella and Fedi (2012) is therefore about the depth weighting function, whose exponent is a constant through the whole space in the original Li and Oldenburg and Cella and Fedi approaches, while it is a 3D function in the method which we will discuss here.

Magnetic and gravity anomalies due to simple sources have been synthetically generated to test the proposed approaches; then, data caused by more complex sources have been analyzed. Finally, two real dataset, from the Vredefort impact site and Mt. Vulture area, have been examined to have a further confirmation of the effectiveness of the methods.

Both tests on synthetic and real data showed that using source information retrieved by a multiscale analysis of the data has a great potential to improve the solution.

Introduction

Even if reflection seismic is still the primary exploration method of exploring for reservoir (i.e. oil, ore or gas deposits,

or energy and environmental resources in general), potential field methods are continuously expanding, thanks to their successful contribution in deeper and more challenging environments, such as sub-salt structures and deep sea, to their smaller cost and to new powerful methods of analysis and modelling, which are indeed related to high-quality and high-resolution data.

The final goal, is, obviously, to obtain a good estimate of the in-place volume. Moreover, information provided by inverting 3D sets of potential field data can help to refine the targets and so to efficiently define and focus projects early on, in order to minimize the risk of investigation before the actual potential is defined. These methods are used also to investigate areas that could be contaminated by pollution and modelling the system to prevent future environmental and engineering critical situations.

One of the principal difficulties with the inversion of the potential field data is the inherent non-uniqueness. In fact, by Gauss' theorem we know that there are infinitely many equivalent source distributions that can produce a measured field (**Blakely, 1996**). When the number of model parameters M is greater than the number of observations N, the problem is called *underdetermined* and a unique solution for the inverse problem does not exist. This represents the most common problem in inversion of potential fields. To solve an undetermined problem and obtain a unique solution we need to add a priori information. Prior information takes numerous forms (geological, geophysical or mathematical) and a good inversion algorithm is able to incorporate this information into the inversion. One of the most important and common prior information is a reference model that might be a uniform half space and for some problems just the zero model.

The origin of inversion methods goes back to 1967, when Bott (1967) used this approach to interpret marine magnetic anomalies. Since then many different algorithms were proposed, each one characterized by a different type of a priori information and then to provide different solutions. Green (1975) searched for a density model that minimizes its weighted norm to some reference model. Safon at al. (1977) used the method of linear programming to compute moments of the density distribution. Fisher and Howard (1980) solved a linear least-squares problem constrained for upper and lower density bounds. Last and Kubik (1983) introduced a 'compact' inversion minimizing the body volume. Guillen and Menichetti (1984) assumed as a constraint the minimum momentum of inertia. Barbosa and Silva (1994) suggested allowing compactness along given directions using a priori information. Li and Oldenburg (1996, 1998) introduced model weighting as a function of depth using a subspace algorithm. Pilkington (1997, 2002) used preconditioned Conjugate Gradients (CG) method to solve the system of linear equations. Portniaguine and Zhdanov (1999, 2002) introduced

regularized CG method and focusing using a reweighted least squares algorithm with different focusing functional. Li and Oldenburg (2003) use wavelet compression of the kernel with logarithmic barrier and conjugate gradient iteration. Pilkington (2009) used data space inversion in Fourier domain.

Other relevant ways to introduce a priori information involve "soft constraints", such as positivity constraint for density and magnetization, or "hard constraints", such as empirical laws, constraints for upper and lower density bounds and for a density monotonically increasing with depth (Fisher and Howard, 1980) and external information from well-logs, geological studies and other geophysical investigations.

Obviously, the solution is highly dependent on the prior information and for this reason, an algorithm that solve every geological context does not cannot exist. So, it is very important to choose the correct algorithm according to the geological context of the studied area and according to the available a priori information.

However, even if the literature is filled by 2D and 3D algorithms for inversion of potential field, there are no 1D algorithms equivalent to those applicable to seismic or electromagnetic methods. From a general point of view, this is not surprising, because 1D problems involve a forward problem referring to set of infinitely extended layers, each one homogeneous in the source property. Indeed, in the gravity case, such an assumed model would produce nothing more than a spatially constant field and, therefore, could not explain any gravity anomalies.

To our knowledge, only a single work (**Fedi and Rapolla, 1995**) regards the inversion of "vertical gravity soundings", that is a 1D inversion method, using a forward problem consisting of a finite volume of layers, each of them with its own density and horizontally finite. The authors first formed a gravity vertical profile, by upward continuation of the data above an area including the sounding and then showed how the inversion of such vertical profile could yield a 1D estimation of the density through the volume.

In this work, we generalize the method to the inversion for a source distribution which is inhomogeneous either laterally or vertically. In practice, we will solve a set of linear inverse problems at many locations on the measurement area, inverting for a density model relative to a set of finite and homogeneous layers at each location. Assuming a large number of layers, we so solve an underdetermined problem, since the data number is less than that of the unknown parameters. Density bounds may be applied, in order to constrain the physical property to lie within a geologically reasonable interval. Because all the 1D inversions are independent of each other, we may finally produce a 2D or 3D model of the physical property joining the results obtained for each vertical sounding. The main disadvantage is that 2D and 3D model models are not built by direct

multidimensional inversion, but by approximation from a multi set of 1D models.

Moreover, in this thesis we have studied a different approach for 2D and 3D potential field inversion. It mathematically starts from the algorithm proposed by Li and Oldenburg (2003) but it is optimized very differently: our logic is that the weighting used in the inversion is directly deduced from the field, in order to obtain a better solution of the physical property distribution in the subsurface.

This information, derived from a multiscale analysis which precedes the inversion itself, will be used to setup a particular depth weighting function that could physically account for a source property, the homogeneity degree, which is transferred to the field by the Poisson equation. So, the main difference between our depth weighting function and those proposed by Li and Oldenburg (2003) resides: a) in being not a feature of the block shape but of the source property; b) in its exponent, that in our case is spatially variable instead of being a constant value for the entire model volume. This last feature reflects the fact that a complex source distribution is characterized by a variable homogeneity degree and that a constant value could yield only average source-model distributions.

1. Elements of Potential fields theory

Gravitational and magnetic fields are both potential fields. In the mass-free space, potential fields obey Laplace's equation, which states that the sum of the rates of change of the field gradient in three orthogonal directions is zero (**Kearey et al., 2002**).

In Cartesian coordinates, Laplace's equation is:

$$\frac{\partial^2 \phi}{\partial x^2} + \frac{\partial^2 \phi}{\partial y^2} + \frac{\partial^2 \phi}{\partial z^2} = 0 \qquad (1)$$

where ϕ refers to a gravitational or magnetic field and is a function of (x, y, z).

Any function satisfying the Laplace's equation, has continuous, single-valued derivatives and has second derivatives (Blakely, 1996). If a function is harmonic in a region R has its maxima and minima on boundaries of the region. Gravity and magnetic fields, are both potential fields and obey all the physical laws mentioned above.

1.1. Gravity field

The gravitational acceleration due to a point of mass m is:

$$\boldsymbol{g}(P) = -\gamma \frac{m}{r^2}\boldsymbol{r} \tag{2}$$

where γ is the Gravitational Constant and **r** is a unity vector that point from mass *m* to the observation point *P*. This gravitational attraction is a conservative field so it can be expressed as the gradient of a scalar potential *U*

$$U(P) = \gamma \frac{m}{r} \tag{3}$$

The gradient of *U* represents the gravity **g**, and the first-order directional derivatives of *U* are the components of gravity in the corresponding direction (**Kearey et al., 2002**) and it is defined as:

$$\boldsymbol{g} = \nabla U = \frac{\partial U}{\partial x}\boldsymbol{i} + \frac{\partial U}{\partial y}\boldsymbol{j} + \frac{\partial U}{\partial z}\boldsymbol{k} \tag{4}$$

where **i**, **j** and **k** are the unit vectors in the positive direction of *x*, *y* and *z* axes respectively. Being a harmonic function, at all the points outside of the mass, $\nabla^2 U = 0$, but in the space occupied by masses:

$$\nabla^2 U = -4\pi\gamma\rho \tag{5}$$

where ρ is the density of the mass distribution at a given point. Equation (5) is the Poisson's equation describing the potential at all points of the mass distribution.

In geophysical exploration, gravimeters measure only the vertical component of the gravity, as given by:

$$g_z = \frac{\partial U}{\partial z} \tag{6}$$

Before the results of a gravity survey can be analyzed and interpreted it is necessary to correct for all variation in the Earth's gravitational field which do not result from the differences of density in the underlying rocks.

The observed gravity is the sum of the following components (**Blakely, 1996**):

- Theoretical gravity, referred to the reference ellipsoid,
- Free air effect, due to the elevation above the sea level,

- Bouguer slab and terrain effects, the normal mass above the sea,
- Tidal and instrumental drift effects, time-dependent variations,
- Eötvös effect, due to moving platform (airborne and shipborne surveys),
- Isostatic effects, accounting for the effects of masses supporting topographic loads,
- Effect of crust and upper mantle density variations.

Isolating the last quantity is the goal of the gravity reductions.

The mean value of gravity at the Earth's surface is about 9.8 ms^{-1}. Variations in gravity caused by density variations in the subsurface are of the order of 100 µm s^{-1}. The *cgs* unit of acceleration due to gravity (1 cm s^{-1}) is the Gal, in honor of Galileo, and its sub-unit milliGal is common in gravity survey (**Kearey et al., 2002**).

1.2. Magnetic field

The magnetic scalar potential *V(r)* of a dipole source whose magnetic moment is **m**, can be written as:

$$V(r) = -\mathbf{m} \cdot \nabla\left(\frac{1}{r}\right) \tag{7}$$

where *r* is the distance modulus.

The magnetic field may also be defined in terms of a force field produced by electric currents. If an electric current *I*, is flowing in a loop of radius *r*, the magnetic strength at the center of the loop is *H = I/2r*.

Materials can be magnetized by acquiring the component of magnetization in the presence of an external magnetic field and it is called induced magnetization which is in the same (or reverse) direction of the external magnetic field as:

$$\mathbf{M} = \chi \mathbf{H} \tag{8}$$

The constant χ in the equation (8) is called the magnetic susceptibility.

Susceptibility is a dimensionless quantity but differs in magnitude if expressed in emu or in SI units. Its definition involves the magnetic permeability μ:

$$\begin{aligned}\mathbf{B} &= \mu_0(\mathbf{H} + \mathbf{M}) \\ &= \mu_0(\mathbf{H} + \chi\mathbf{H}) \\ &= \mu_0(1 + \chi)\mathbf{H} \\ &= \mu\mathbf{H} \\ \mu &= \mu_0(1 + \chi)\end{aligned} \qquad (9)$$

The relationship between **M** and **H** is not necessarily linear because the magnetic susceptibility χ may vary with the field intensity, may be negative, and may be represented more accurately in some materials as a tensor (**Blakely, 1996**). Susceptibility is a measure of how susceptible a material is to become magnetized (**Reynolds, 1997**). There are many kinds of magnetizations and their understanding is important to understand how the variations of magnetic properties produce the magnetic anomalies (**Hinze et al., 2013**). These properties can be defined as:

Diamagnetism, for example, is an inherent property of all matter. In the presence of external magnetic field, the orbital path of the electron rotates in a way that induced magnetization is small and in the opposite sense to the applied field. Consequently, diamagnetic susceptibility is negative.

Paramagnetism, is a property of those solids that have atomic magnetic moments because in this substance, the electron shells are incomplete, so the unpaired electrons produce a magnetic field. When it is placed in an external magnetic field, the atomic moments or unpaired electrons partially align parallel to the applied field thereby producing a net magnetization in the direction of the applied field. This is still, however a relatively weak effect. However, all minerals are diamagnetic, and some are paramagnetic or ferromagnetic but, in both cases, their magnetizations do not have significant contributors to the geomagnetic field.

Though, there is a class of magnetism that have great importance on geomagnetic studies. Certain materials not only have atomic moments, but neighbouring moments interact strongly with each other. This interaction is a result of a quantum mechanical effect called exchange energy. Suffice is to say that the exchange energy causes a spontaneous magnetization that is many times greater than paramagnetic or diamagnetic effects (**Blakely, 1996**). These types of materials are called *ferromagnetic*. There are several types of ferromagnetic materials, depending on the alignment of their atomic moments. If the atomic moment aligned parallel to one another, results ferromagnetism; if the atomic moments are aligned antiparallel to one another and total moment is neutralized, results anti-ferromagnetism; and the last is the ferrimagnetism, in which atomic moments are antiparallel but, having different

magnitudes, do not cancel. The strength of the magnetization of ferromagnetic and ferrimagnetic materials decreases with temperature and disappears at the Curie temperature (**Kearey et al., 2002**).

The spontaneous magnetization of ferromagnetic materials can be very large at the scale of individual mineral grain but, due to their random orientation, the net magnetization may be negligible at outcrop scale. Due to the presence of ferromagnetic minerals, rocks will acquire a magnetization $\mathbf{M_i}$, called induced magnetization in the direction of applied field **H** can be denoted as:

$$\mathbf{M_i} = \chi \mathbf{H} \tag{10}$$

If the rock is placed in a field-free environment, the induced magnetization falls to zero (**Blakely, 1996**). However, ferromagnetic materials have a special ability to retain a permanent magnetization even in the absence of external magnetic fields and it is called remanent magnetization, may be denoted by $\mathbf{M_r}$. The remanent magnetization of crustal rock depends not only on their atomic structure, crystallographic and chemical composition, but also on their geological, tectonic and thermal history. In geophysical studies, it is usual to consider the total magnetization **M** of the rock as the vector summation of induced and remanent magnetization, that is:

$$\mathbf{M} = \mathbf{M_i} + \mathbf{M_r} = \chi \mathbf{H} + \mathbf{M_r} \tag{11}$$

The ratio between remanent magnetization and induced magnetization is expressed by the Koenigsberger ratio as the following:

$$Q = \frac{|\mathbf{M_r}|}{|\mathbf{M_i}|} = \frac{|\mathbf{M_r}|}{|\chi \mathbf{H}|} \mathbf{g}(P) = -\gamma \frac{m}{r^2} \mathbf{r} \tag{12}$$

These magnetizations may be oriented in different directions and may differ significantly in magnitude. The magnetic effects of a rock arise from the resultant **M** of the two magnetization vectors. Magnetic anomalies caused by the rocks are superposed to the geomagnetic field similar to gravity anomalies which are superposed to the gravitational field. However, the magnetic field is more complex, due to the variation in amplitude and in direction of the geomagnetic field. Consequently, knowledge of the behavior of the magnetic field is necessary both in the reduction of magnetic data to a suitable datum and in the interpretation of the resulting anomalies. The magnetic field is geometrically more complex than the gravity field of the Earth and exhibits irregular variation in both orientation and magnitude with latitude, longitude and time (**Kearey et al.,**

2002). Total-field magnetometers are usually the instrument of choice for airborne and shipborne magnetic surveys. As the name implies, total-field magnetometers measure the magnitude of the total magnetic field without regard to its magnetic direction.

The total field **T** is given by:

$$\mathbf{T} = \mathbf{F} + \Delta\mathbf{F} \tag{13}$$

where **F** is the geomagnetic field and Δ**F** represents the perturbation of **F** due to some crustal magnetic sources. The total-field anomaly is calculated from total-field measurements by subtracting the magnitude of a suitable regional field, usually the IGRF model appropriate for the date of the survey. If **T** represents the total field at any point, and F is the regional field at the same point, then the total-field anomaly is given by (**Blakely, 1996**):

$$\Delta\mathbf{T} = |\mathbf{T}| - |\mathbf{F}| \tag{14}$$

If |**F**| >> |Δ**F**|, the total field Δ**T** can be considered as the component of the anomalous field Δ**F** in the direction of **F** and thus it can be considered a harmonic function (e.g., **Blakely, 1996**). This condition is usually verified in crustal magnetic studies.

The SI unit of magnetic field strength is the tesla (T). For the magnetic variation due to rock, a sub-unit, the nanotesla (nT), is commonly used; 1 nT=10^{-9} T. The strength of F varies from about 25000 nT in equatorial regions to about 70000 nT at the poles (**Kearey et al., 2002**).

1.3. Scaled field and homogeneity law

As described in Fedi et al. (2015), scaling laws allow modelling the Earth as a scaling medium and are important to describe its degree of complexity. If one tries to classify physical source-distributions in terms of their complexity, statistical models of growing complexity have been used, following scaling laws either monofractal, in which the scaling is expressed by a power law valid globally, or multifractal, in which the scaling is expressed by a local power law, changing at each position/scale. For instance, fractal models of both the types have been used in geophysics to describe the well logs of susceptibility, seismic wave speed and other physical properties of the Earth's rocks (e.g. **Pilkington & Todoeschuck 1993; Hermann 1997; Marsan & Bewan 1999**).

Other classes of source distributions have been used in applied geophysics to deal with a simplified medium, and so describe the source distribution at different levels of

complexity. We will here refer to fields following one specific kind of scaling-law, called homogeneity law.

The source-distributions of such fields may be generated by restricting the solutions of the integral equations of the gravity and magnetic fields (or of their derivatives) to a set of homogeneous density distributions with very simple geometrical shapes, such as spheres and infinitely extended cylindrical or planar distributions of density or susceptibility. Some of these simple source distributions are called one-point sources, because their field f can be represented as a field generated by a source distribution having its support in just one-point $\mathbf{r}_0(x_0, y_0, z_0)$

The most important property of the fields of one-point sources is that they are homogeneous functions of degree n, meaning that they satisfy the following scaling law, called homogeneity equation, in the region R at any observation points $\mathbf{r}(x, y, z)$ and $\mathbf{r}_t(x_t, y_t, z_t)$:

$$f(tx, ty, tz) = t^n f(x, y, z) \tag{15}$$

where $t > 0$ and n is the homogeneity degree.

Based on this equation, Euler's theorem (e.g. **Olmsted 1991**) shows that if f is continuously differentiable and homogeneous of degree n in R, the homogeneity of the field may be expressed by the differential equation:

$$\nabla f(\mathbf{r}) \cdot \mathbf{r} = -nf(\mathbf{r}) \tag{16}$$

When the source position is $\mathbf{r}_0(x_0, y_0, z_0)$, eq. (16) assumes the form:

$$\nabla f(\mathbf{r}) \cdot (\mathbf{r} - \mathbf{r_0}) = -nf(\mathbf{r}) \tag{17}$$

The differential form of Euler equation is important because it assesses the homogeneity properties in a local sense. Thompson (1982) and then Reid et al. (1990) introduced a popular algorithm based on eq. (17), namely the Euler deconvolution, allowing the computation of the unknown source-coordinates $\mathbf{r}_0(x_0, y_0, z_0)$ from the field values within a moving window $W(\mathbf{r})$ on the measurement plane.

This innovation was important because it opened the way to automated methods of source depth estimation, which have been used especially in industry to process massive data sets in a short computation time. Many other 'Euler deconvolution' algorithms were since then proposed, applying it to different fields (field derivatives, modulus of the analytic signal, Hilbert transforms) and the unknowns were extended to include other parameters, e.g. a constant background term B and to the

so called structural index, N, usually defined as the opposite of the homogeneity degree (n) for the magnetic field of ideal sources. A summary of many of the main Euler algorithms can be found in Fitzgerald et al. (2004). Euler deconvolution was also reformulated in a multiscale framework by Florio & Fedi (2006, 2014) and Fedi et al. (2009).

The most obvious one-point sources are the pole-source in the gravity case and the dipole-source in the magnetic case. As is well known, such sources generate homogeneous fields of homogeneity degrees equal to −2 and −3, in the gravity and magnetic case, respectively. Other ideal sources have been however considered, all characterized by the degree of homogeneity of their homogeneous

fields, which, in the magnetic case, corresponds to an integer ranging from −3 to 0. In fact, the ideal sources considered in the Euler deconvolution are the infinite line of dipoles (n = −2), the semi-infinite thin sheet (n = −1) and the bottomless contact (n = 0).

Besides these cases, all characterized by a global kind of scaling law, homogeneous fields may be used as suitable models to approximate the behavior of any real field even when the potential fields are not homogeneous in the sense of eq. (1), meaning that homogeneity equation is not valid in the whole harmonic region, while holding on in selected sub-areas of the harmonic region. This is likely to happen when the source distribution is more complex than any of the ideal sources. For instance, Florio et al. (2014) recently analyzed the behavior of the magnetic field of a cube.

Steenland (1968) was probably the first to show that, for the most realistic cases of inhomogeneous potential fields, n can be fractional and is varying with the distance to the source, being dependent on the depth and kind of source distribution.

It was empirically shown that when the sources are different from the one-point sources and the estimated n is not integer, the estimated depth is not relative to the source top or center, but to a point somewhere positioned between the top and the center of the source (**Keating & Pilkington 2004**; **Gerovska et al. 2005**). However, it is important to stress that it has been recently shown that homogeneous sources and corresponding fields may exist, whose homogeneity degree may be fractional as well (**Fedi et al. 2012**; **Fedi et al. 2015**). They are characterized by having some intermediate properties between those corresponding to two subsequent one-point sources of integer n, as shown in Fig. 1, where the gravity anomalies are drawn for a pole (Fig. 1a), its fractional integration of order α = −0.5 (Fig. 1b) and for a bottomless vertical line mass (Fig. 1c). Basing on that, we may so extend the range of allowed homogeneity degrees to any real value within the range: $-3 \leq n \leq 0$.

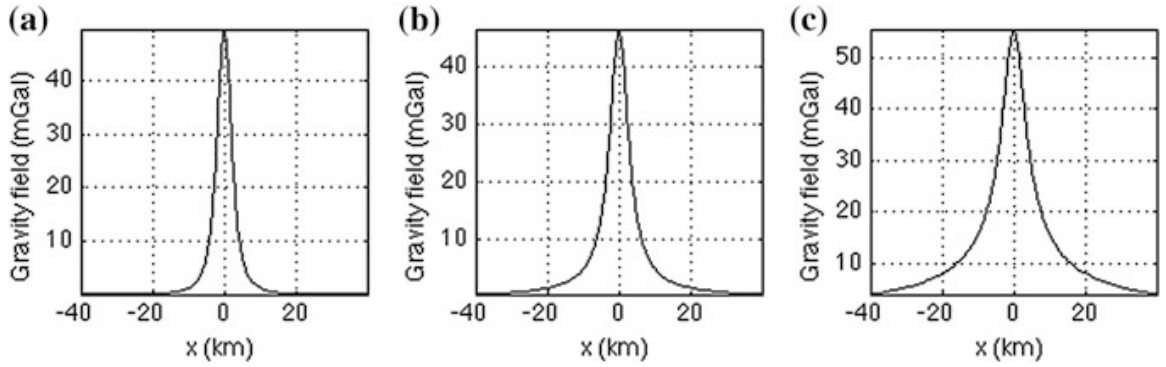

*Figure 1: The gravity anomalies due to a pole source (a), to a fractional order α = -0.5 integration of a pole source (b) and to a bottomless vertical line mass (c). (from **Fedi, 2016**)*

Following strictly Fedi (2016) we may say that, similar to what happens for random source models, where the fractal scaling-law has been generalized into a multifractal law, the homogeneity law could be generalized into the following multihomogeneity law:

$$f(ax, ay, az) = a^{n(x,y,z)} f(x, y, z) \tag{18}$$

so that the differential Euler equation becomes:

$$\nabla f(\mathbf{r}) \cdot (\mathbf{r} - \mathbf{r_0}) = -n(\mathbf{r}) f(\mathbf{r}) \tag{19}$$

and *n* may now assume fractional or integer values as well. This generalization takes into account that real fields are essentially inhomogeneous and typically present a fractional and spatially varying homogeneity-degree.

Starting from this law, we will see in chapter 4 that this varying homogeneity-degree may be is used directly in the inversion of potential fields, as an exponent of a specifically designed weighting function.

2. Elements of Inversion Theory

If N measurements are performed in a particular experiment, one might consider their values as the elements of a vector **d** of length N. Similarly, the model can be represented as a vector **m** of length M, whose elements are the source strength in specified sub-volumes of the source volume.

$$\begin{aligned} &data: && \mathbf{d} = [d_1, \dots, d_N]^T \\ &model: && \mathbf{m} = [m_1, \dots, m_M]^T \end{aligned} \tag{20}$$

The basic statement of an inverse problem is that the model and the data are in some way related. Usually the relationship takes the form of one or more formulas that the data and model are expected to follow.

The simplest and best-understood inverse problems are the linear ones, that can be represented with the explicit equation:

$$\mathbf{Am} = \mathbf{d} \tag{21}$$

The matrix **A** (with $N \times M$ dimension) is called kernel. This is the basic equation of discrete inverse theory. Many important inverse problems that arise in the physical sciences involve precisely this equation.

Others, while involving more complicated equations, can often be solved through linear and iterative approximations (**Menke, 1989**).

When the number of the data (N) is lower than the number of model elements (M) the problem in equation (21) is an underdetermined problem. For these problems it is possible to find more than one solution for which the prediction error E is zero. A priori information helps us in this task.

The first kind of a priori assumption we shall consider is the expectation that the solution to the inverse problem is simple, where the notion of simplicity is quantified by some measure of the length of the solution. One such measure is simply the Euclidean length of the solution:

$$L = \mathbf{m^T m} = \sum m_i^2 \tag{22}$$

A solution is therefore defined to be simple if it is small when measured under the L^2 norm. We pose the following problem: find the solution $\mathbf{m_{est}}$ that minimizes equation (22) subject to the constraint that **e** = **d** - **Am** = **0** and we obtain the **minimum length solution:**

$$\mathbf{m} = \mathbf{A}^{\mathbf{T}}[\mathbf{A}\mathbf{A}^{\mathbf{T}}]^{-1}\mathbf{d} \quad (23)$$

There are many instances in which $L = \mathbf{m}^{\mathbf{T}}\,\mathbf{m}$ is not a very good measure of solution simplicity. One may not want to find a solution that is smallest in the sense of closest to zero but one that is smallest in the sense that it is closest to some known model $\mathbf{m_0}$. The obvious generalization of equation (22) is then (**Menke, 1989**):

$$L = (\mathbf{m} - \mathbf{m_0})^T(\mathbf{m} - \mathbf{m_0}) \quad (24)$$

Where $\mathbf{m_0}$ is the a **priori value** of the model parameters.

Often, the whole idea of length as a measure of simplicity is inappropriate and then we can introduce a weighting matrix $\mathbf{W_m}$ that may introduce a priori information. So, equation (24) becomes:

$$L = (\mathbf{m} - \mathbf{m_0})^T\mathbf{W_m}(\mathbf{m} - \mathbf{m_0}) \quad (25)$$

Frequently some observations are made with more accuracy than others. In this case one would like the prediction error **e**, of the more accurate observations to have a greater weight in the quantification of the overall error E than the inaccurate observations. To accomplish this weighting, we define a generalized prediction error:

$$E = \mathbf{e}^{\mathrm{T}}\mathbf{W_d}\mathbf{e} \quad (26)$$

where the matrix $\mathbf{W_d}$ defines the relative contribution of each individual error to the total prediction error (**Menke, 1989**).

When the problem is affected by numerical instability and by inherent ambiguity, it is called 'ill-posed'. This problem needs to be regularized to be solved. The most common and well-known form of regularization is the one known as Tikhonov regularization (**Tikhonov and Arsenin, 1977**)

$$\mathbf{m}_\mu = \arg\min\{\|\mathbf{A}\mathbf{m} - \mathbf{d}\|_2^2 + \mu^2\|\mathbf{m}\|_2^2\} \quad (27)$$

where the regularization parameter, μ controls the weight given to minimization of the side constraint relative to minimization of the residual norm. Clearly, a large value of μ, (equivalent to a large amount of regularization) favours a small solution semi-norm at the cost of a large residual norm, while a small, (i.e., a small amount of regularization) has the opposite effect. This parameter also controls the sensitivity of the regularized solution **m** to perturbations in **A** and **d**, and the perturbation bound is proportional to μ^{-1}.

Other two methods to solve the inverse problem for underdetermined cases involve QR factorization and Lagrange multipliers.

QR factorization is based on the decomposition of the matrix $\mathbf{A}^{\mathbf{T}}$ into the product of two different matrices, **Q** and **R**, where **Q** is an orthogonal matrix and **R** is an upper triangular matrix.

The QR factorization (if implemented properly) allows the construction of stable solutions of the system **Am**=**d**. However, it is costly in terms of speed but can also be applied to rectangular systems.

The Lagrange multipliers method is instead a particular tool to solve an inverse problem with a priori constraints, including the constraint equations (of the form **Fm**=**h**) as row in **Am**=**d**, forcing the prediction error to zero at the expense of increasing the prediction error of the other equations.

In this case the objective function is:

$$\varphi(\mathbf{m}) = \sum_{i=1}^{N}\left[\sum_{j=1}^{M} A_{ij}m_j - d_i\right]^2 + 2\sum_{i=1}^{p}\lambda_i\left[\sum_{j=1}^{M} F_{ij}m_j - h_i\right] \tag{28}$$

Where p is the number of constraints and $2\lambda_i$ are the Lagrange multipliers (Menke, 2006).

2.1. Depth Weighting Function

As we have just said in the previous paragraph, the minimum length solution can be defined as the solution for the underdetermined problem. This hypothesis on the solution is the first and the most common a priori information that can be used.

This kind of minimization, without other constraints, provides solutions with model elements of low value near the surface, because in this case the solution is the shortest, as we required in the minimum length formulation. This because the kernel decays with distance and so the simplest (minimum length) solution will be that being the most concentrated, this implying that having the lowest values in a smaller volume. This obviously means that such solution cannot be deep (in this case higher values and larger volume would be involved) and it will be instead near the surface (Figure 2b).

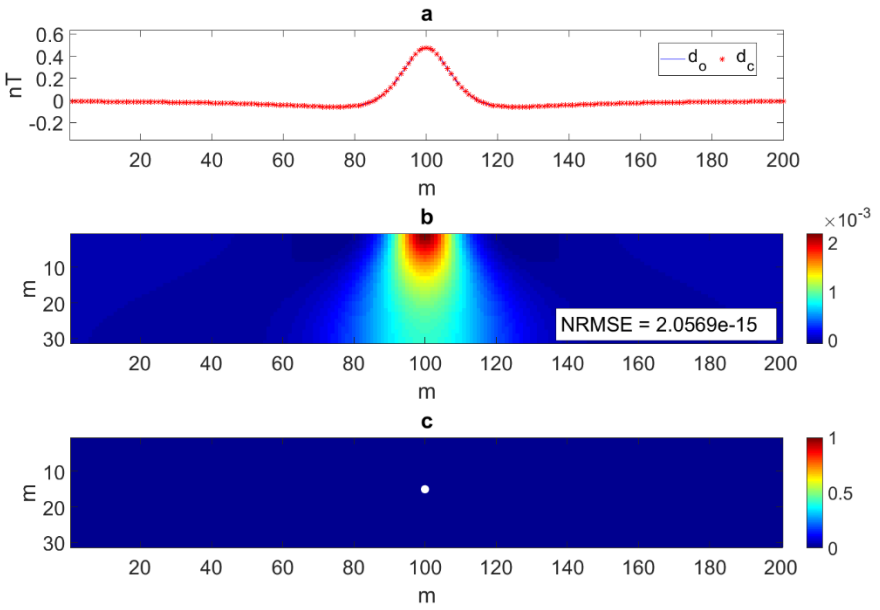

Figure 2: (a) Magnetic field due to a dipole horizontal line shown in (c) by the white dot. Blue solid line is the observed data and the red asterisks are the calculated data of (b) the Minimum Length solution.

We repeat that this kind of density distribution does not depend on the characteristics of the observed data, but it is a direct consequence of the supplied a priori information.

To avoid this too strong influence of the minimum length hypothesis, we need to introduce more a priori information. Li and Oldenburg (1996) were the first that studied this problem and introduced a *depth-weighting function*:

$$w_z = \frac{1}{(z + z_0)^{\beta/2}} \tag{29}$$

where z is the depth of each layer in the 3D model and the value of z_0 depends upon the observation height and cell size (**Oldenburg and Li, 2005**). Li and Oldenburg propose to use for β a value equal to 3 in the magnetic case (**Li and Oldenburg, 1996**) and equal to 2 in the gravity case (**Li and Oldenburg, 1998**), assuming 3 and 2 as the rate decay of the magnetic or gravity field of a single, small, roughly cubic cell.

Oldenburg and Li (2005) later suggested that the exponent value used in a particular inversion could be chosen, by finding the best performance of different exponent values applied to trial inversions of synthetic data from forward models similar to the expected solution.

Cella and Fedi (2012) showed instead that the appropriate value of β must be related to N, the structural index of the source (Table 1), rather than to the power-law decay of the field generated by a single cell.

Source	N(grav)	N(mag)
Point mass or dipole sources, spheres	2+k	3+k
Line or masses of dipoles infinite	1+k	2+k
Semi-infinite plane, thin dike, sill	0+k	1+k
Contact	-1+k	0+k

Table 1 – Structural Index (k = order of differentiation)

Moreover, Ialongo et al. (2014) have shown the connection between the depth weighting exponent β and the regularization parameter μ, where this last one is chosen by using the generalized cross-validation method (GCV).

The structural index may be estimated with standard methods such as Euler Deconvolution or the study of the scaling function (**Fedi, 2007; Florio et al., 2009; Barbosa et al., 1999; Fedi and Florio, 2006**). We will see in detail chapter 4, how to estimate the structural index by the scaling function method.

For all the inversion performed in this work we will use the Li and Oldenburg (2003) algorithm, which allows solving underdetermined problems, with the number of cells significantly larger than the amount of available data. The related objective function is satisfied by many different solution models that generate practically the same data. This goal is reached using appropriate weighting functions whose parameters are empirically selected, based on numerical modeling and qualitative analysis of typical gravity or magnetic anomalies.

The solution is obtained by the following minimization problem (**Oldenburg and Li, 2005**):

$$\begin{aligned} &\text{minimize } \varphi = \varphi_d + \mu\varphi_m \\ &\text{subject to } \mathbf{m}_{min} \leq \mathbf{m} \leq \mathbf{m}_{max} \end{aligned} \tag{30}$$

where $\mathbf{m}_{min}$ and $\mathbf{m}_{max}$ are vectors containing the lower and upper bounds on the model values, and $\mathbf{m}$ is the vector containing model values. Besides that and the weighting function, other prior information that this algorithm allows to introduce might be: knowledge of a background or reference model and a general assumption that the structures should be smooth or, alternatively, that they have sharp edges at least locally (**Oldenburg and Li, 2005**).

The algorithm uses the *logarithmic barrier method* with the *conjugate gradient* technique (CG) as the central solver. In the logarithmic barrier method, the bound constraints are implemented as a logarithmic barrier term.

The objective function is given by (**Gill et al. 1991**):

$$\varphi(\lambda) = \varphi_d + \mu\varphi_m - 2\lambda \sum_{j=1}^{M} \left[ln\left(m_j - m_j^{min}\right) + ln\left(m_j^{max} - m_j\right) \right] \tag{31}$$

where μ is the regularization parameter, λ is the barrier parameter, φ_d is the weighted data misfit and φ_m is the model objective function. The weighted data misfit is given by:

$$\varphi_d = \|\mathbf{W_d}(\mathbf{d} - \mathbf{d_{obs}})\|^2 \tag{32}$$

where $\mathbf{d}$ are the predicted data, $\mathbf{d_{obs}}$ are the observed data-vector and $\mathbf{W_d}$ is the inverse data-covariance matrix.

$$\begin{aligned}\varphi_m(m) = \alpha_s \int_{vol} w_s w^2(z)(\mathbf{m} - \mathbf{m_0})^2 dv \\ + \alpha_x \int_{vol} w_x \left(\frac{\partial w(z)(\mathbf{m} - \mathbf{m_0})}{\partial x}\right)^2 dv + \cdots \\ + \alpha_y \int_{vol} w_y \left(\frac{\partial w(z)(\mathbf{m} - \mathbf{m_0})}{\partial y}\right)^2 dv + \cdots \\ + \alpha_z \int_{vol} w_z \left(\frac{\partial w(z)(\mathbf{m} - \mathbf{m_0})}{\partial z}\right)^2 dv\end{aligned} \tag{33}$$

where $\mathbf{m}$ is the unknown model, $\mathbf{m_0}$ is a reference model and $w(z)$ is the depth-weighting function (29).

The terms w_s, w_x, w_y, w_z are spatially dependent weighting functions to input additional prior information about density or susceptibility model. In particular, the weights w_x, w_y, w_z, with or without a reference model, control the degree of smoothness of the solution along the three directions (**Oldenburg and Li, 2005**); finally, α_s, α_x, α_y and α_z are coefficients controlling the importance of each term.

The logarithmic barrier term forms a barrier along the boundary of the feasible domain and prevents the minimization from crossing over to the infeasible region. The method solves a sequence of nonlinear minimizations with decreasing λ and, as λ approaches zero, the sequence of solutions approaches the solution of equation (30).Further details on how a numerical solution is obtained discretizing the model objective function can be found in Oldenburg and Li (1994).Instead of carrying out the full minimization at each iteration, it is common to take a Newton step for each value of λ and adjust the step length so that the updated model remains positive (**Gill et al. 1991**). The step length is also used to determine the decreased value of the barrier parameter λ for the next iteration (**Li and Oldenburg, 2003**).

The barrier iteration continues until the value of λ is sufficiently small such that barrier term has a negligible contribution to the total objective function (31) and the

iteration stops when the objective function is changing less than 1%.

Looking at the equation of the objective model function (33), it is easy to understand the key role of the depth weighting function $w(z)$, where, accordingly to Cella and Fedi (2012), the exponent β must be related to N.

For this reason, we decided to create a β function, estimating N in every single point of our source-domain. In this way the equation (29) will be:

$$w(x,y,z) = \frac{1}{z^{\beta(x,y,z)/2}} \tag{34}$$

We will call the equation (34) inhomogeneous depth weighting function.

In order to build this function, we need to estimate β in every point of our domain. We decided to use an approach based on the scaling function method (**Fedi et al 2006**), which will be described in Chapter 4.

3. [Papers] Methods for 1D inversion of potential field

In this chapter we show two papers published in international scientific journals that describe the 1D method developed under this thesis project, for the inversion of potential fields.

The first one describes the theoretical aspects of this new method, with applications on synthetic and real gravity data, in the Frenchman Flat (Nevada) sedimentary basis, where the obtained density model is in good agreement with the results of density log.

The second one shows the application on magnetic real data, under a joint interpretation with other information from TDEM. One relevant result is that our joint cooperative interpretation allows a significant interpretation of the Drybones kymberlites, Canada, with an improved modelling either laterally or in depth.

GEOPHYSICS, VOL. 83, NO. 2 (MARCH-APRIL 2018); P. G15–G23, 8 FIGS.
10.1190/GEO2017-0186.1

A method for inversion of 1D vertical soundings of gravity anomalies

Andrea Vitale[1], Domenico Di Massa[1], Maurizio Fedi[1], and Giovanni Florio[1]

ABSTRACT

We have developed a method to interpret potential fields, which obtains 1D models by inverting vertical soundings of potential field data. The vertical soundings are built through upward continuation of potential field data, measured on either a profile or a surface. The method assumes a forward problem consisting of a volume partitioned in layers, each of them homogeneous and horizontally finite, but with the density changing versus depth. The continuation errors, increasing with the altitude, are automatically handled by determining the coefficients of a third-order polynomial function of the altitude. Due to the finite size of the source volume, we need a priori information about the total horizontal extent of the volume, which is estimated by boundary analysis and optimized by a Markov chain process. For each sounding, a 1D inverse problem is independently solved by a nonnegative least-squares algorithm. Merging of the several inverted models finally yields approximate 2D or 3D models that are, however, shown to generate a good fit to the measured data. The method is applied to synthetic models, producing good results for either perfect or continued data. Even for real data, i.e., the gravity data of a sedimentary basin in Nevada, the results are interesting, and they are consistent with previous interpretation, based on 3D gravity inversion constrained by two gamma-gamma density logs.

INTRODUCTION

The purpose of this work is to develop a 1D method for analyzing anomalies of potential fields.

The scientific literature is extraordinarily rich in algorithms concerning 2D and 3D potential field data inversion (e.g., Last and Kubik, 1983; Guillen and Menchetti, 1984; Litinsky, 1989; Li and Oldenburg, 1996; Barbosa and Silva 1994; Silva and Barbosa, 2004, 2006; Cella and Fedi, 2012; Paoletti et al., 2014; Silva Dias et al., 2009; Wijns and Kowalczyk, 2007). However, there are no 1D algorithms equivalent to those applicable to seismic or electromagnetic methods. From a general point of view, this is not surprising because 1D problems involve a forward problem referring to a set of infinitely extended layers, each one homogeneous in the source property. Indeed, in the gravity case, such an assumed model would produce nothing more than a spatially constant field and, therefore, it could not explain any gravity anomalies.

To our knowledge, only a single work (Fedi and Rapolla, 1995) regards the inversion of "vertical gravity soundings," that is, a 1D inversion method, using a forward problem consisting of a finite volume of layers, each of them with its own density and horizontally finite. The authors first form a gravity vertical profile, by upward continuation of the data above an area including the sounding and then show how the inversion of such a vertical profile could yield a 1D estimation of the density through the volume.

In this work, we generalize the method to the inversion for a source distribution, which is inhomogeneous either laterally or vertically. In practice, we will solve a set of linear inverse problems at many locations on the measurement area, inverting for a density model relative to a set of finite and homogeneous layers at each location. Assuming a large number of layers, we, therefore, solve an underdetermined problem because the data number is less than that of the unknown parameters. Density bounds may be applied to constrain the physical property to lie within a geologically reasonable interval. Because all the 1D inversions are independent of each other, we may finally produce a 2D or 3D model of the physical property joining the results obtained for each vertical sounding. The main disadvantage is that 2D and 3D models are not built by direct multidimensional inversion but by approximation from a multiset of 1D models.

We tested our method by analyzing either synthetic or real data. To make realistic simulations, we also interpreted synthetic cases with data generated by upward continued data.

1D VERTICAL SOUNDINGS

The basic idea of the vertical gravity soundings (Fedi and Rapolla, 1995) was that the vertical distribution of density could

Manuscript received by the Editor 22 March 2017; revised manuscript received 25 September 2017; published ahead of production 13 November 2017; published online 28 December 2017.
[1]Università di Napoli "Federico II", Dipartimento di Scienze della Terra, dell'Ambiente e delle Risorse, Napoli, Italy. E-mail: andrea.vitale@unina.it; domenico.dimassa@hotmail.it; fedi@unina.it; gflorio@unina.it.

be deduced by the gravitational field known at different altitudes.

Following Fedi and Rapolla (1995), we start from the relation that defines the gravitational field generated at the point of coordinates $r = (x, y, z)$ by a distribution of mass density $\rho(r')$ in a volume V':

$$g(r) = \gamma \int_{V'} \rho(r') \frac{z' - z}{|r - r'|^3} dv', \tag{1}$$

where γ is the gravitational constant and

$$|r - r'| = \sqrt{(x - x')^2 + (y - y')^2 + (z - z')^2}. \tag{2}$$

If the density varies just vertically (1D model),

$$\rho(r') = \rho(z'). \tag{3}$$

Consider now a vertical sounding with N measurements at $r_j(\bar{x}, \bar{y}, z_1, \ldots, z_N)$, where the altitudes vary as $z_1, \ldots, z_N$, with $j = 1, \ldots, N$, and the horizontal coordinates $(\bar{x}, \bar{y})$ are fixed.

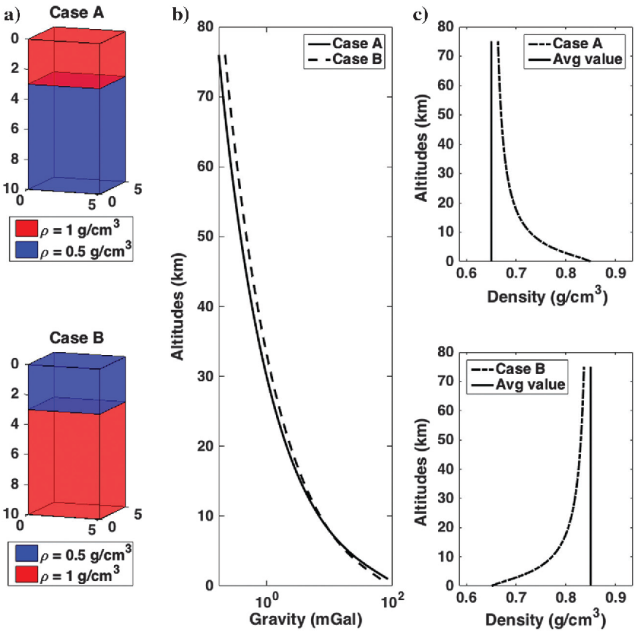

Figure 1. Vertical variations of the gravity field and the apparent density of a two-layered source. We study two cases (a): a denser upper layer at the top (case A) or a denser bottom layer (case B). (b) Model A (solid line) is stronger at lower altitudes than 8 km compared with model B (the dashed line). At 8 km, they are equal, and at altitudes higher than 8 km, the field from model B has the highest values. (c) Apparent density. The solid vertical lines indicate the average density of the bodies, weighted by the thicknesses of the layers of each body.

Then, equation 1 becomes

$$g(r_j) = \gamma \int_{V'} \rho(z') \frac{Z' - z_j}{|r_j - r'|^3} dv', \tag{4}$$

where

$$|r_j - r'| = \sqrt{(\bar{x} - x')^2 + (\bar{y} - y')^2 + (z_j - z')^2}. \tag{5}$$

This equation describes the 1D forward problem of a continuous unknown function $\rho(z)$, linearly related to the measured gravity data. If we now assume a discrete number M of layers in each of them, the density is homogeneous, we have

$$g(r_j) = \sum_{i-1}^{M} \rho_i G_{ij}, \tag{6}$$

where

$$G_{ij}(r_j) = \gamma \int_{V_i} \frac{z' - z_j}{|r_j - r'|^3} dv, \tag{7}$$

and $\{\rho_i\}$, $\{V_i\}$ are, respectively, the densities and the volumes of the M layers with $i = 1, \ldots, M$.

To better understand if the field at different altitudes allows information about the sources, we now analyze two simple cases. The first one (case A in Figure 1a) is relative to a prismatic source built by two layers with the upper one being denser; the second one (case B in Figure 1a) has instead the upper layer less dense. The two models have the same geometry and dimensions (the upper layer is $5 \times 5 \times 3$ km, and the bottom layer is $5 \times 5 \times 7$ km). Consider now two profiles built at the center of the two blocks. Figure 1b shows that the field from the model A (solid line) is stronger at low altitudes than that from the model B (dashed line), at 8 km they are equal, and so also the corresponding apparent densities (Figure 1c), at altitudes higher than 8 km, the field from model B has the highest values.

Following Fedi and Rapolla (1995), we may have another way to distinguish the effects from the two sources, by introducing a quantity called the apparent density $\langle \rho(z_j) \rangle$

$$\langle \rho(z_j) \rangle = \frac{\int_V \rho(z') \frac{z' - z_j}{|r_j - r'|^3} dv}{\int_V \frac{z' - z_j}{|r_j - r'|^3} dv}. \tag{8}$$

The apparent density is a normalized gravity that has the physical dimension of density. It is, in fact, obtained through the division of the field by a gravity field relative to the same volume,

where the density is homogeneous and equal to 1 g/cm^3. Apparent density is really meaningful in distinguishing between the two cases: In fact, at low altitudes, in the cases A (solid line) and B (dashed line), it has a close value to each one's own true density of the top (Figure 1c). On the contrary, at high altitudes, it asymptotically tends to the respective weighted average of the two layers' densities, the weighting being the thicknesses of the two layers.

This example clearly shows that there is information about the source property distribution within a vertical gravity sounding. However, it is not easy to handle this quantity because we need to know exactly the normalizing volume. In addition, as shown by Fedi and Rapolla (1995), a linear system involving the equivalent density (equation 8) is equivalent to that formed by that related to the 1D gravity problem (equation 6) because the gravity data and the kernel are divided by the same quantity, that is, the normalizing factor in equation 8.

Therefore, we turn to the original 1D gravity problem, based on equation 6:

$$\mathbf{g} = \mathbf{Gm}, \tag{9}$$

where $\mathbf{g}$ represents the vector of dimensions N formed by the data, $\mathbf{m}$ represents the density vector of dimensions M refers to the volume, and $\mathbf{G}$ represents the matrix of the theoretical kernel of dimensions $(M \times N)$ defined in equation 7.

The presence of experimental errors ($\Delta\mathbf{d}$) implies that the fitting between experimental data and theoretical data ($\mathbf{Gm}$) is searched according to

$$\mathbf{g} - \Delta\mathbf{g} \le \mathbf{Gm} \le \mathbf{g} + \Delta\mathbf{g}. \tag{10}$$

Besides, to reduce the number of possible models that are the solution to our problem, we may constrain the solution by a priori information about the density of each layer

$$\delta\rho_L \le \delta\rho_i \le \delta\rho_H. \tag{11}$$

With these inequalities, the solution may be found by solving the optimization problem of minimizing $\|\mathbf{m}\|_2$ subject to inequality constraints (Menke [1989], pp. 130–131).

The problem 9 is transformed into

$$\mathbf{G}'\mathbf{m}' = \mathbf{g}', \tag{12}$$

where

$$\mathbf{G}' = \begin{bmatrix} \mathbf{F}^{\mathrm{T}} \\ \mathbf{h}^{\mathrm{T}} \end{bmatrix}; \quad \mathbf{g}' = \begin{bmatrix} \mathbf{0} \\ 1 \end{bmatrix}. \tag{13}$$

The matrix $\mathbf{F}$ contains both the kernel $\mathbf{G}$, of dimensions $(M \times N)$, relative to the vertical sounding data $\mathbf{g}$ of dimensions N and the matrices associated with additional constraints. Similarly, the vector $\mathbf{h}$ of dimensions $(2N + 2M)$ contains the data vector $\mathbf{g}$ and the values of the constraints ($m_L = \delta\rho_L$ and $m_H = \delta\rho_H$) as

$$\mathbf{F} = \begin{bmatrix} \mathbf{G} \\ -\mathbf{G} \\ \mathbf{I} \\ -\mathbf{I} \end{bmatrix}, \quad \mathbf{h} = \begin{bmatrix} \mathbf{g} - \Delta\mathbf{g} \\ -(\mathbf{g} + \Delta\mathbf{g}) \\ \mathbf{m}_L \\ -\mathbf{m}_H \end{bmatrix}, \tag{14}$$

where M is the number of layers in the model volume and N is the number of altitudes of each sounding. The functions $\mathbf{F}$ and $\mathbf{h}$ may be used to solve the problem in particular conditions, such as those relating to mitigate the effect of a trend or noisy data (we will discuss that later with equation 18 and system 19).

Our problem is solved (Menke, 1989) by searching for the solution $\mathbf{m}'$ that minimizes

$$\mathbf{e}' = \|\mathbf{g}' - \mathbf{G}'\mathbf{m}'\|_2, \quad \text{subject to } \mathbf{m}' \ge \mathbf{0}, \tag{15}$$

noting that if the prediction error $\mathbf{e}' \neq \mathbf{0}$, the constraints $\mathbf{Fm} \ge \mathbf{h}$ are consistent and the solution of the problem is

$$m_i = -\frac{e'_i}{e'_{M+1}} \quad \text{with } i = 1, \ldots, M. \tag{16}$$

It is intuitive to understand that inequalities 10 and 11 allow for managing the overall tolerance of this technique. Refer to Menke (1989, pp. 130–131, equations 7.52–7.58) for the complete description of the algorithm.

To generate a synthetic data set, we used an algorithm to generate gravity data of a prism-like source at different altitudes (Plouff, 1976). For each synthetic model, a map of gravity anomalies is generated at each altitude, related to a density distribution synthetically defined. From each map, a profile is extracted, passing through the center of the anomaly, each consisting of K measurement stations. The kth measurement station along the horizontal profile ($1 \le k \le K$) will indicate the spatial position of the kth vertical sounding P_k, formed by the N measurements related to that station at different N altitudes (Figure 2). The altitudes are chosen following the rationale that the solution does not change adding the field at altitudes greater than some level.

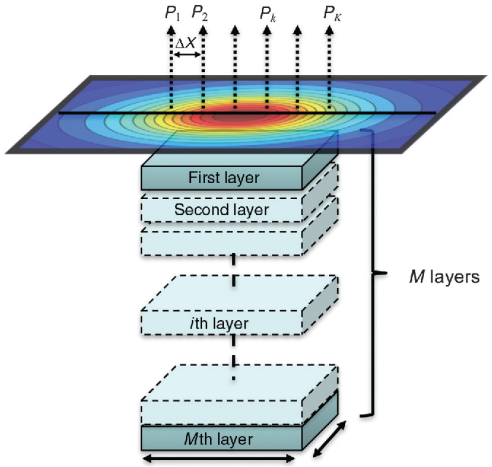

Figure 2. Generic theoretical volume of M layers for a set of K vertical soundings (P_k). The measurement level is taken as the zero level, in which the measured anomaly field is shown.

In this paper, we will invert a set of vertical soundings, such as those in Figure 2, to the end of producing approximated models of the density distributions of 2D or 3D complex bodies.

We use a procedure similar to other kinds of 1D modeling in geophysics, such as resistivity vertical electric sounding, for which a set of infinitely extended horizontal layers is assumed at each sounding and the result is assigned just at the sounding location.

In our case, for each sounding, we assume that the source volume is made of a set of homogeneous layers: They are not infinitely extended, but they are as large as the boundary analysis defines (Figure 2). Then, the depth-density model found is assigned to the corresponding sounding position. Therefore, we refer to a single vertical sounding, say P_1 in Figure 2. After inverting for the layer densities in the source, the result is attributed to a set of layers sized ΔX, i.e., the step size of the vertical soundings along the profile, and centered at the profile position. Repeating this procedure for all the soundings, we obtain an approximate 2D model of the source distribution along the profile.

Forming and inverting a set of vertical soundings

As shown in Figure 2, the theoretical volume is composed of M layers of constant thickness. The total thickness T and the horizontal extension must be fixed by a priori information. Boundary analysis can be used for this task (e.g., Bott, 1962; Blakely and Simpson, 1986). We applied here the enhanced horizontal derivative (EHD) method (Fedi and Florio, 2001) that is based on the total horizontal derivative of the weighted sum of the vertical derivatives of increasing order. Appropriate weighting helps to define accurate boundaries of the source. In complex cases, with sources lying at different depths, EHD provides the best edge definition among edge estimators, as shown in Cella et al. (2009). The source boundaries can be outlined by considering the locations of the maxima of the EHD function, as shown in Figure 3b (the red-contoured area highlighted by dots) for the gravity anomaly in Figure 3a. In this case, the series consider the terms from the field to the fourth derivative, using a weighting factor of one for each of the five terms. The maxima are represented by the white dots, and they were calculated using a Canny edge detection function in MATLAB. The source is a prism with a 50 m depth to the top, a 250 m depth to the bottom, and a 0.5 g/cm^3 density contrast. Its horizontal dimensions are 110 m along the x-axis and 130 m along the y-axis.

We have now specified the vertical and horizontal size of the source volume. Therefore, we can proceed to form the vertical soundings for each profile, according to equations 6 and 7. This means that at the kth sounding position, we will form the system

$$\begin{bmatrix} \mathbf{G}_k \\ -\mathbf{G}_k \\ \mathbf{I} \\ -\mathbf{I} \end{bmatrix} \mathbf{m}_{\text{est}} = \begin{bmatrix} \mathbf{g}_k - \Delta\mathbf{g} \\ -(\mathbf{g}_k + \Delta\mathbf{g}) \\ \mathbf{m}_L \\ -\mathbf{m}_H \end{bmatrix}, \tag{17}$$

where $\mathbf{I}$ is the identity matrix of dimensions $(M \times M)$, $\mathbf{G}_k$ is the kernel of the kth sounding of dimensions $(M \times N)$, and $\mathbf{g}_k$ is the data vector of dimension N. In this way, we built the matrix $\mathbf{F}$ of dimensions $[(2N + 2M) \times M]$ and the vector $\mathbf{h}$ of dimensions $(2N + 2M)$:

$$\mathbf{F} = \begin{bmatrix} \mathbf{G}_k \\ -\mathbf{G}_k \\ \mathbf{I} \\ -\mathbf{I} \end{bmatrix}, \quad \mathbf{h} = \begin{bmatrix} \mathbf{g}_k - \Delta\mathbf{g} \\ -(\mathbf{g}_k + \Delta\mathbf{g}) \\ \mathbf{m}_L \\ -\mathbf{m}_H \end{bmatrix}. \tag{18}$$

The system 17 takes into account all the constraints, errors ($\Delta\mathbf{g}$), and density bounds ($\mathbf{m}_L$ and $\mathbf{m}_H$).

However, data are hardly measured at varying altitudes, so that we will calculate the data at a set of altitudes by upward continuation of the data from the measurement level (e.g., Baranov [1975], pp. 48–56; Blakely [1996], pp. 313–319). Upward continuation strictly holds for an infinitely extended measurement region S and for data known there continuously. Therefore, in a real case, i.e., that of a finite region and discrete data sets, the continuation formulas do not hold exactly, but only approximately, so that the upward-continued data must be regarded as being affected by some errors, due to imperfect continuation. For further details, we remind the reader of a previous paper in which this issue was specifically discussed by Fedi et al. (2012). In

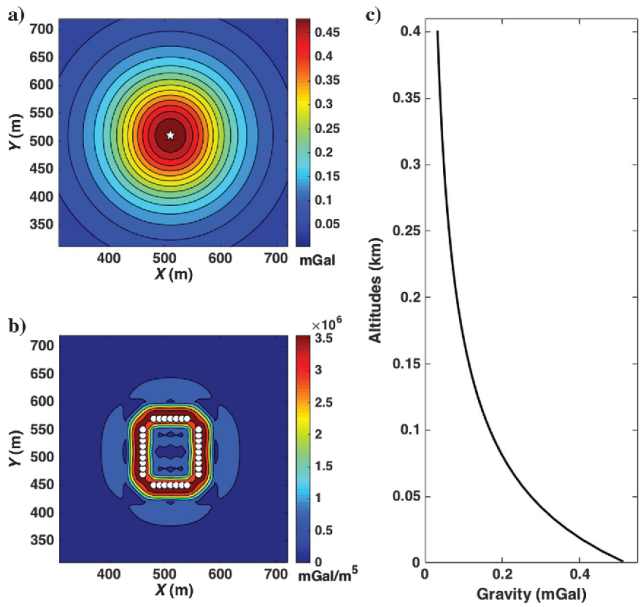

Figure 3. Boundary analysis for estimating the source size. (a) Gravity map produced by a synthetic buried body (see text). (b) EHD considering the series from the field to the fourth order of the vertical derivatives and weighting factor of one for each of the five terms (the white dots highlight the maxima). (c) Vertical gravity sounding at the position marked in (a) by the white star.

particular, we follow Castaldo et al. (2014), which approximated the continuation error by a third-order polynomial:

$$H(z) = c_1 + c_2 z + c_3 z^2 + c_4 z^3, \tag{19}$$

where c_1, c_2, c_3, and c_4 are unknown coefficients to be estimated during the inversion process. This polynomial can account for errors due to the upward continuation operator and errors due to trends of no interest in our analysis, such as that caused, for example, by a deeper source.

At this point, our system 17 must be changed to add the constraints due to the polynomial, which results in increasing the number of unknowns:

$$\begin{bmatrix} \mathbf{S}_k \\ -\mathbf{S}_k \\ \mathbf{I}_p \\ -\mathbf{I}_p \end{bmatrix} \begin{bmatrix} \mathbf{m}_{\text{est}} \\ \mathbf{c} \end{bmatrix} = \begin{bmatrix} \mathbf{g}_k - \Delta\mathbf{g} \\ -(\mathbf{g}_k + \Delta\mathbf{g}) \\ \mathbf{m}_L \\ -\mathbf{m}_H \end{bmatrix}, \tag{20}$$

where $\mathbf{c}$ is the vector formed by the third-order polynomial coefficients in equation 19, $\mathbf{S}_k$ of dimensions $[(M+4)\times N]\times[(M+4)\times N]$ is $\mathbf{G}_k$ plus the four polynomial coefficients, and $\mathbf{I}_p$ is the identity matrix of dimensions $(M+4)\times(M+4)$.

SYNTHETIC EXAMPLES

Let us now describe the multisounding inversion for a synthetic case related to a single buried body as described in the previous section (Figure 3). We begin with a prism having a 50 m depth to the top, a 250 m depth to the bottom, and a 0.5 g/cm^3 density contrast. Let us assume a gravity profile, extracted from the anomaly shown in Figure 3a at $y = 510$ m, and assume the y-axis as the strike direction.

The altitudes for the vertical soundings range from 1 to 401 m with an 8.2 m step. We will consider 33 vertical soundings, spaced horizontally 10 m along the x-axis. For each sounding, we assume a set of 100 layers, each 5 m thick, to have a satisfactory depth resolution and a 500 m model depth limit for the source thickness.

The last important parameter to set is the horizontal extent of the source volume that we retrieved quite precisely using the EHD method (the white dots in Figure 3b). As already said, the series consider the terms from the field to the fourth derivative, using a weighting factor of one for each of the five terms.

We now consider two cases: The first is relative to perfect data, which is of profiles built with data generated at the various altitudes by Plouff's formula and using strong constraints ($0 \le \delta\rho \le 0.5$ g/cm^3) (Figure 4a) or weaker constraints ($0 \le \delta\rho \le 1$ g/cm^3). The second case is that of profiles built from upward continued of the map data shown in Figure 3a. We fixed the experimental error on the data to $\Delta g = 2\times10^{-12}$ mGal because we are simulating a perfect data case. We show the results for only weak constraints (Figure 4c).

The results are consistent with the true model (the white box in Figure 4a–4c). The density contrast is consistent with the true model. Moreover, the obtained density distribution allows for an unambiguous estimation of the depth to the top of the structure in all three cases. The source bottom could be very well estimated in the perfect data case (Figure 4a and 4b), whereas there is some resolution loss in the case of upward-continued data (Figure 4c).

We have above obtained for a simple source a good estimate of the horizontal source extension (Figure 3b). However, in a real case, this task could not be so easy and some estimation errors are possible, not only considering errors in estimates of the edges but also possible estimation issues due to the particular geometry of the source. However, we may improve the quality of our estimates by using a Markov chain approach.

The Markov chain is a stochastic process in which the conditional distribution at any future time $t+1$ for a given past state and a present state depends only on the present state:

$$\begin{aligned} P_{ij}(t+1) &= P\{X(t+1) = j | X(t) = i, \\ &\quad X(t-1) = i_{t-1}, \ldots, X(0) = i_0\} \\ &= P\{X(t+1) = j | X(t) - i\}, \end{aligned} \tag{21}$$

where i is the outcome of the kth trial of the process $X(k)$ when $k = t$ and $P_{ij}(t+1)$ is the probability that the outcome of the stochastic process will be j at the trial $k = t+1$ (Sen and Stoffa, 2013). From equation 21, we can easily understand that the probability of the outcome of a given trial depends only on the outcome of the previous trial. This statistical approach is used in several research fields (e.g., Bengio et al., 2017; Didelot et al., 2017; Hartemink et al., 2017) with the purpose of optimizing the parameters of a study.

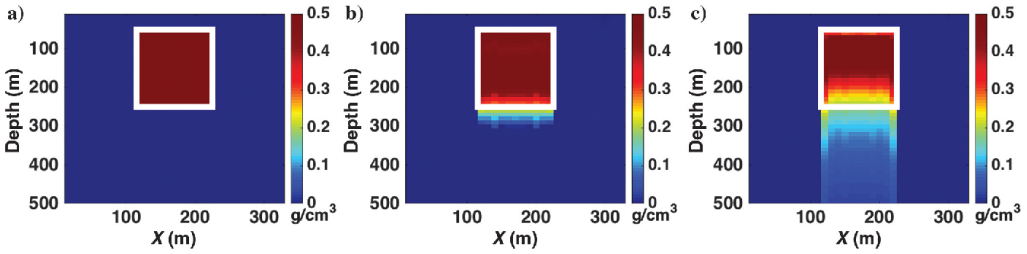

Figure 4. Source reconstructed after inversion for 33 vertical soundings relative for a prismatic source (see the text). (a) Model after inversion with perfect data and constraints $0 \le \delta\rho \le 0.5$ g/cm^3 and $\Delta g = 2\times10^{-12}$ mGal. (b) Model after inversion with perfect data and constraints $0 \le \delta\rho \le 1$ g/cm^3 and $\Delta g = 2\times10^{-12}$ mGal. (c) Model after inversion with upward-continued data and constraints $0 \le \delta\rho \le 1$ g/cm^3 and $\Delta g = 2\times10^{-12}$ mGal. The white box outlines the true body.

Let us now describe the workflow that we used in this paper. Starting from the data map at the lowest altitude, we first perform a boundary analysis using the EHD to have an initial estimation of the source horizontal dimension. In general, the form of the source is not regular, so we can approximate its shape by subdividing the source into a set of thin prisms, as shown in Figure 5c. This gives different estimates for the north–south sizes, moving, for instance, along a west–east profile. Consequently, the system in equation 20 will now become relative to a set of layers of complex shape, according to the results of the boundary analysis. Because we may expect that the estimates of the prism size are affected by error, we may optimize the north–south size of each thin prism, at each iteration of the Markov chain (equation 21), in such a way as to improve the fitting among observed and calculated data. We assume increments or decrements comparing the observed and the calculated data. If the calculated data underestimate the observed data, the prism size should be bigger. If the calculated data overestimate the observed data, the prism size should be smaller. This logic was used for a positive anomaly, whereas an inverse logic was used for a negative anomaly (such as a sedimentary basin). To this end, we may assume increments or decrements of a small fixed quantity per each iteration step. We obtained good results assuming this quantity is equal to the data spacing ΔX.

At this point, the model volume was changed according to this procedure and the inversion process proceeds to the next iteration. During the inversion, when inverting for prism k, the obtained density model is assigned only to prism q. In the match between the observed and calculated fields, we consider the densities computed for each qth inversion, respectively, related to the qth prism. The final model is the sum of the effects of the whole set of Q prisms. After the inversion, the misfit is calculated again, and if needed the sizes of the prisms are changed. The cycle of iterations will end when a prefixed misfit error is reached.

We used the same setup of the source of the synthetic example described above, with perfect data, but subdivide the model volume into 11 prismatic sources. To test this approach, we decided to use for each of the 11 prismatic sources horizontal dimensions randomly distributed between 150 and 90 m and obtained the results shown in Figure 6 for three iterations of the entire process, namely, at the 1st, 5th, and 10th steps. About the constraints, we used the strong constraints on densities that we mention above ($0 \leq \delta\rho \leq 0.5$ g/cm^3). The function Δg is set initially to a relatively

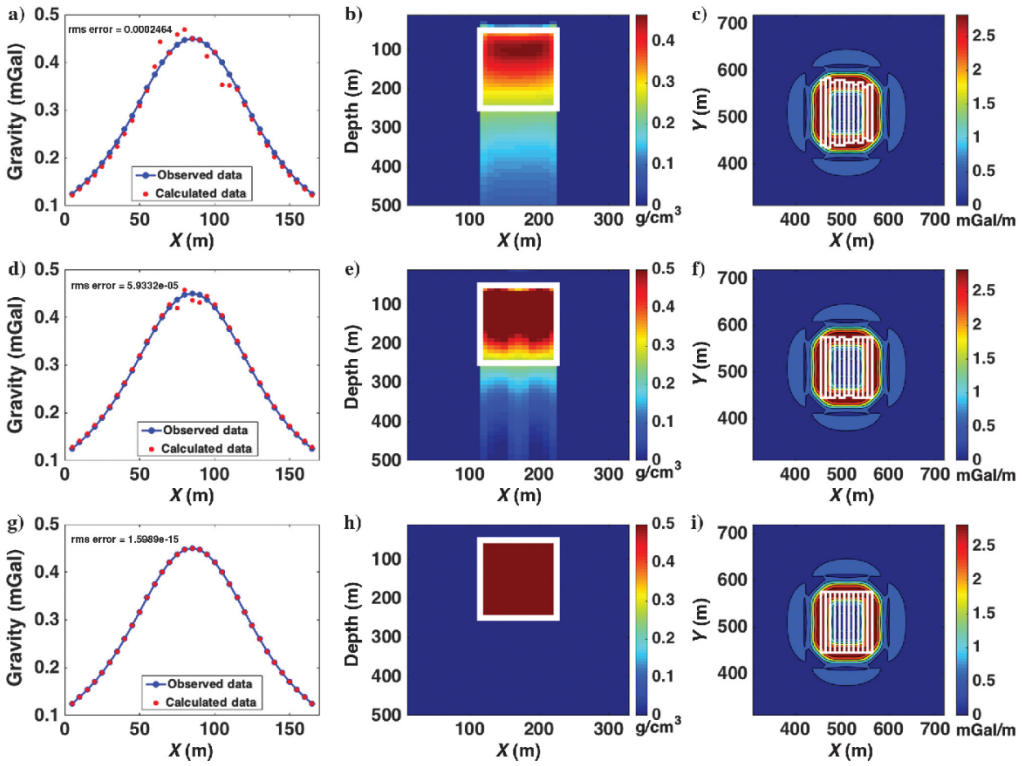

Figure 5. Markov chain process for estimating the optimal size of the source. First iteration: (a) observed (blue solid line) and calculated (red dots) gravity anomalies. (b) Inverted model and (c) estimated boundary (the white boxes highlight the dimensions used for the different prisms). (d-f) and (g-i) are the same as (a-c) for, respectively, 5th iteration and 10th iteration.

high value, say, 10^{-3} mGal, because the initial model is rough. As the iterations proceed, Δg can be reduced to improve the fit. The results are relative to the modeled anomaly (the red points in Figure 6a, 6d, and 6g), the inverted source density (Figure 6b, 6e, and 6h), and the estimated sizes of the 13 prisms (Figure 6c, 6f, and 6i). In particular, we may see that the results at the first iteration (Figure 6a–6c) are the worst, as expected, whereas they undoubtedly improve at the fifth iteration (iteration, Figure 6d–6f), and they become very good at the last iteration (Figure 6g–6i). The root-mean-square errors are 2×10^{-4}, 5×10^{-5}, and 1×10^{-15}, respectively, at the first, fifth, and at the last iteration.

The estimates of the density contrast and the depths to the top and the bottom obtained at the last iteration are very well consistent with the synthetic model (Figure 4a).

CASE HISTORY

We will now discuss the application of this method to real data, related to the sedimentary basin of Frenchman Flat, Nevada Test Site (NTS), USA. Fedi and Rapolla (1995) have already analyzed a single vertical sounding of a synthetic sedimentary basin, obtaining good results about its vertical density distribution (their Figure 9). However, they notice that a model volume with horizontal dimensions a bit smaller than what detected by boundary analysis is needed. Here, we apply our multisoundings method to a real data case following this advice.

The Frenchman Flat is a Cenozoic Basin located within the southeastern edge of the NTS. It is filled with Quaternary and Tertiary volcanic and sedimentary deposits that lie unconformably on faulted and folded Palaeozoic and pre-Cambrian strata. Phelps and Graham (2002) have estimated the depth of the basin in Frenchman Flat using a gravity inversion model, constrained by two gamma-gamma density logs.

According to Phelps and Graham (2002), the basin bottom is located at 2.4 km depth in the northeast sector of the basin, as shown in Figure 6a. We digitized the gravity isostatic map in Figure 2 of Phelps and Graham (2002).

Figure 6 shows the isostatic gravity map (Figure 6a) and its EHD (Figure 6b), which consider the terms from the field to the fourth derivative, using a weighting factor of one for each of the five terms. The vertical soundings will be made along the line as shown in Figure 6a (the white dots).

Our first step was defining the shape of the basin through a boundary analysis. The EHD analysis led to a complex shape, as shown in Figure 6b by white dots, with an average extension of approximately 10 km along north–south direction and approximately 12.5 km in the west–east direction. Note that we ignored the EHD maxima at $y > 20$ km, according to the geology of the area, which links the northwestern portion of the gravity anomaly to a different basin, the Yucca Flat.

To build the vertical soundings, we upward continued the zero-level data set to altitudes from 1 m to 9 km with a 112.5 m step. Then, we considered 50 vertical soundings, spaced 0.5 km, along the profile in Figure 7a.

Phelps and Graham (2002) interpret the gravity data with a 0.4 g/cm^3 density contrast, based on previous geologic knowledge and two gamma-gamma density logs. Therefore, about the density contrast bounds, we preferred to use a wide range, from −0.8 to 0.1 g/cm^3, in order not to constrain the density model too much, and $\Delta g = 0.2$ mGal.

We then performed the 1D inversion for all the vertical soundings according to the system 20 and to the source parameters described as in the following. To account for such a complex shape, we decided to subdivide along the west–east direction the source volume in 22 thin prisms of variable north–south length, each one 0.5 km thick. Because it regards the total thickness, in the synthetic cases, we showed that the total thickness of the model volume should be greater than the source thickness (Figure 3). Therefore, considering that Phelps and Graham interpreted the basin with a model reaching the deepest depth of 2.4 km, we decided to assume the bottom depth of the volume to be equal to a 5 km depth. The source volume was then subdivided in a set of 200 layers.

Similar to the synthetic case described in the previous section, a Markov chain algorithm was used to select the best north–south size extent for the assumed 22 thin prisms. At the first step, we used the estimates provided by the boundary analysis, shown in Figure 7a. The inverted densities for each sounding were then merged to build a 2D model at each iteration of the Markov chain. For each of them, the resulting field was compared with the true data along the profile

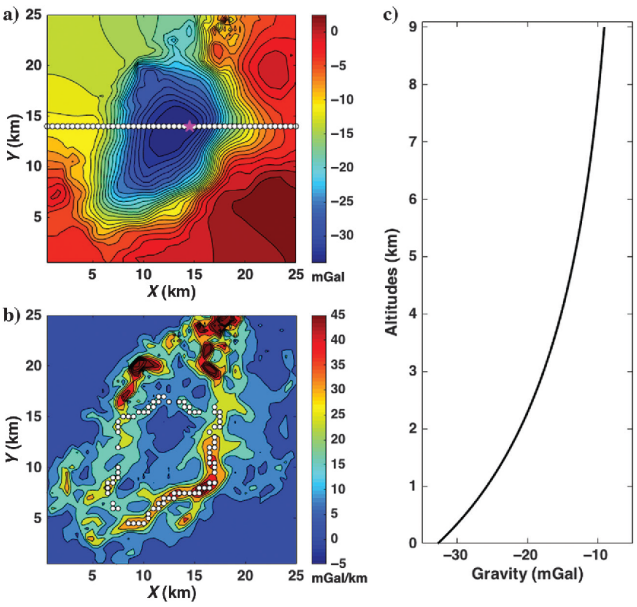

Figure 6. (a) Isostatic gravity map of the Frenchman Flat sedimentary basin and vertical sounding positions (white dots). (b) EHD of the gravity map in (a), using terms from the field to the fourth derivative and unit weights; the basin boundary is marked by the white dots. (c) Vertical gravity sounding at the position marked in (a) by the purple star.

in Figure 6a, and the relative misfit was computed. After 20 iterations, we stopped the Markov chain iterations and obtained the best misfit error, corresponding to the north–south size extents shown in Figure 7b.

We can find the final 2D model in Figure 8d. It may be seen that the fit with the original data (solid blue line) and the interpreted model (red dots) is very good (Figure 8a). In this figure, the polynomial trend recovered during the inversion of each vertical sounding, shown in Figure 8b, is added back to the model data. The interpreted basin model extends mainly from the zero-level toward a maximum depth of approximately 2.5 km, as indicated by the black solid line, below which weaker density contrasts less than 0.1 g/cm^3 are estimated. This broadening somewhat of the density model versus depth is an unavoidable feature of this method and was also observed for the synthetic case (Figure 4c). However, it is important to see that the estimated density model well agrees with the model proposed by Phelps and Graham (2002), as illustrated in Figure 8d, in which the red line is the estimated density contrast highlighted by the black line $A - A'$ in Figure 8c and the blue line is the model proposed by the authors.

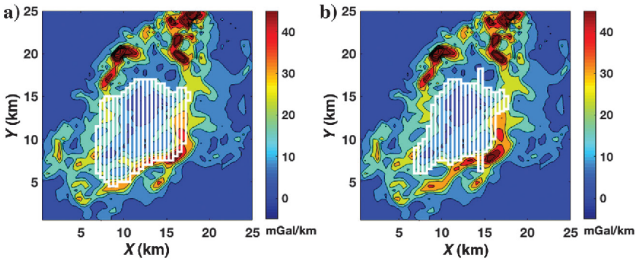

Figure 7. EHD of the gravity map in Figure 6a; the basin was subdivided in 22 prisms (the white boxes). (a) The white boxes show the sizes (a) at the 1st iteration and (b) at the 20th iteration of the Markov chain process for the 22 prisms. See the text for further details.

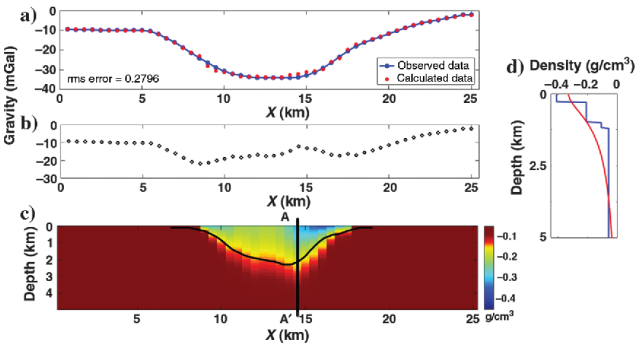

Figure 8. Inversion of the anomaly in the Frenchman Flat basin (Nevada, USA). (a) Gravity anomaly (blue line) versus estimated gravity anomaly by the inversion model (red dots). (b) Polynomial trend as recovered during the inversion. (c) Our depth model after inversion, which well reconstructs the basin geometry, as compared with the basement estimated by Phelps and Graham (2002) (the black line). (d) Estimated density contrast (the red line) versus depth, referred to the part highlighted by the black line $A - A'$ in (c), compared with the density model (the blue line) by Phelps and Graham (2002).

CONCLUSION

We have described a 1D method for inverting gravity data, which has several aspects of interest.

One relevant feature is that it is, to our knowledge, one of the few algorithms allowing 1D inversion of potential fields. As any 1D algorithms in geophysics, it is a flexible tool: it can be used for producing a local image of the source distribution, as our real-data case shows in the case of a density log, or to produce sections and even volumes of source distribution, as our synthetic and real cases demonstrate. In this last case, the method will obviously produce only an approximate characterization of the underground source distribution, which should be better interpreted with more refined 2D/3D algorithms. However, our examples show the usefulness of producing this kind of source distribution model.

The main difficulty is to have a good estimate of the dimensions of the source, necessary for building a reasonable model volume. Regarding the thickness and the depth of this volume, we can adopt a thickness much larger than expected from a priori information, so that it does not appear a difficult parameter to estimate, or, in other words, it is a problem not too different than that in any inverse algorithm. The horizontal dimension of the source volume is instead a critical parameter of this inversion, and we tried to outline a valid strategy for its estimation based on two steps:

1) boundary analysis, to have our first estimate of the source extent, and
2) a Markov chain approach, to search for the optimal value of the horizontal extent along the strike-length direction, which yields the best data misfit for each sounding.

A good feature of this algorithm is that once conditions (1 and 2) are relatively well satisfied, bounds for the density constraints are not critical and wide bounds may be safely adopted.

The second problem is that these soundings are built through upward-continued data; that is, they contain some continuation error, increasing versus the altitude. In this case, we provide a rather good solution by subtracting for each sounding a third-order polynomial function of the altitude. Synthetic cases of a single buried body provided good results for either the geometry and the density contrast of the source, even if we use upward-continued data and relatively wide bounds for the density.

About the computational requirements of our algorithm, on a Mac Pro (early 2009), when all the starting parameters are chosen, the elapsed time for the first iteration was approximately five minutes.

The method is automatic, provided some trials for the weights are made, so the interpreter is called to choose the best setting for EHD transformation giving the best continuity of the boundaries.

We tested this new method on a real case of a sedimentary basin in the USA (Frenchman Flat basin, Nevada). Also using wide bounds

for the density contrast, we obtained a fairly good result, comparable with that obtained by others using a gravity inversion model constrained by two gamma-gamma density well-log results.

Extension of the method to the magnetic case is possible and will be discussed in a future paper.

ACKNOWLEDGMENTS

The authors are grateful to the associate editor and to M. Pilkington, S. Goussev, and another anonymous reviewer for stimulating numerous improvements to the original manuscript.

REFERENCES

Baranov, W., 1975, Potential fields and their transformations in applied geophysics: Gebrüder Borntraeger.
Barbosa, V. C. F., and J. B. C. Silva, 1994, Generalized compact gravity inversion: Geophysics, **59**, 57–68, doi: 10.1190/1.1443534.
Bengio, Y., T. Mesnard, A. Fischer, S. Zhang, and Y. Wu, 2017, STDP as presynaptic activity times rate of change of postsynaptic activity approximates backpropagation: Neural Computation, **29**, 555–577, doi: 10.1162/NECO_a_00934.
Blakely, R. J., 1996, Potential theory in gravity and magnetic applications: Cambridge University Press.
Blakely, R. J., and R. W. Simpson, 1986, Approximating edges of source bodies from magnetic or gravity anomalies: Geophysics, **51**, 1494–1498, doi: 10.1190/1.1442197.
Bott, M. H. P., 1962, A simple criterion for interpreting negative gravity anomalies: Geophysics, **27**, 376–381, doi: 10.1190/1.1439026.
Castaldo, R., M. Fedi, and G. Florio, 2014, Multiscale estimation of excess mass from gravity data: Geophysical Journal International, **197**, 1387–1398, doi: 10.1093/gji/ggu082.
Cella, F., and M. Fedi, 2012, Inversion of potential field data using the structural index as weighting function rate decay: Geophysical Prospecting, **60**, 313–336, doi: 10.1111/j.1365-2478.2011.00974.x.
Cella, F., M. Fedi, and G. Florio, 2009, Toward a full multiscale approach to interpret potential fields: Geophysical Prospecting, **57**, 543–557, doi: 10.1111/j.1365-2478.2009.00808.x.
Didelot, X., C. Fraser, J. Gardy, and C. Colijn, 2017, Genomic infectious disease epidemiology in partially sampled and ongoing outbreaks: Molecular Biology and Evolution, **34**, 997–1007.
Fedi, M., and G. Florio, 2001, Detection of potential fields source boundaries by enhanced horizontal derivative method: Geophysical Prospecting, **49**, 40–58, doi: 10.1046/j.1365-2478.2001.00235.x.
Fedi, M., G. Florio, and L. Cascone, 2012, Multiscale analysis of potential fields by a ridge consistency criterion: The reconstruction of the Bishop basement: Geophysical Journal International, **188**, 103–114, doi: 10.1111/j.1365-246X.2011.05259.x.
Fedi, M., and A. Rapolla, 1995, Vertical gravity and magnetic soundings: Forward problem formulation and data inversion: Bollettino di Geofisica Teorica ed Applicata, **37**, 191–205, doi: 10.1093/molbev/msw275.
Guillen, A., and V. Menichetti, 1984, Gravity and magnetic inversion with minimization of a specific functional: Geophysics, **49**, 1354–1360, doi: 10.1190/1.1441761.
Hartemink, N., T. I. Missov, and H. Caswell, 2017, Stochasticity, heterogeneity, and variance in longevity in human populations: Theoretical Population Biology, **114**, 107–116, doi: 10.1016/j.tpb.2017.01.001.
Last, B. J., and K. Kubik, 1983, Compact gravity inversion: Geophysics, **48**, 713–721, doi: 10.1190/1.1441501.
Li, Y., and D. W. Oldenburg, 1996, 3-D inversion of magnetic data: Geophysics, **61**, 394–408, doi: 10.1190/1.1443968.
Litinsky, V. A., 1989, Concept of effective density: Key to gravity depth determinations for sedimentary basins: Geophysics, **54**, 1474–1482, doi: 10.1190/1.1442611.
Menke, W., 1989, Geophysical data analysis: Discrete inverse theory: Academic Press (Elsevier).
Paoletti, V., P. C. Hansen, M. F. Hansen, and M. Fedi, 2014, A computationally efficient tool for assessing the depth resolution in large-scale potential-field inversion: Geophysics, **79**, no. 4, A33–A38, doi: 10.1190/geo2014-0017.1.
Phelps, G. A., and S. E. Graham, 2002, Preliminary gravity inversion model of Frenchman Flat basin, Nevada Test Site, Nevada: U.S. Geological Survey Open-File Report 02–363.
Plouff, D., 1976, Gravity and magnetic fields of polygonal prisms and application to magnetic terrain corrections: Geophysics, **41**, 727–741, doi: 10.1190/1.1440645.
Sen, M. K., and P. L. Stoffa, 2013, Global optimization methods in geophysical inversion: Cambridge University Press.
Silva, J. B. C., and V. C. Barbosa, 2004, Generalized radial inversion of 2D potential-field data: Geophysics, **69**, 1405–1413, doi: 10.1190/1.1836815.
Silva, J. B. C., and V. C. Barbosa, 2006, Interactive gravity inversion: Geophysics, **71**, no. 1, J1–J9, doi: 10.1190/1.2168010.
Silva Dias, F. J., V. C. Barbosa, and J. B. C. Silva, 2009, 3D gravity inversion through an adaptive-learning procedure: Geophysics, **74**, no. 3, J9–J21, doi: 10.1190/1.3092775.
Wijns, C., and P. Kowalczyk, 2007, Interactive geophysical inversion using qualitative geological constraints: Exploration Geophysics, **38**, 208–212, doi: 10.1071/EG07021.

Journal of Applied Geophysics 158 (2018) 48–56

Contents lists available at ScienceDirect

Journal of Applied Geophysics

journal homepage: www.elsevier.com/locate/jappgeo

Joint interpretation of AEM and aeromagnetic data acquired over the Drybones kimberlite, NWT (Canada)

Domenico Di Massa [a,*], Maurizio Fedi [b], Giovanni Florio [b], Andrea Vitale [b], Andrea Viezzoli [c], Vlad Kaminski [c]

[a] Geophysical Consultant at DIMMS CONTROL Srl, Italy
[b] Univerity of Naples Federico II, Italy
[c] Aarhus Geophysics Aps, Denmark

ARTICLE INFO

Article history:
Received 24 March 2018
Accepted 4 July 2018
Available online 22 July 2018

Keywords:
Kimberlite detection
Joint interpretation
1D vertical magnetic soundings
IP effects
VTEM data

ABSTRACT

We present the joint interpretation of airborne electromagnetic and aeromagnetic data, acquired to study kimberlite pipes. We analyse the data surveyed in 2005 over Drybones Bay, Archean Slave Province of the Northwest Territories, northern Canada. This area hosts a recently discovered kimberlite province with >150 kimberlite pipes.

Magnetic and electromagnetic data were each one modelled by 1D inversion. For magnetic data we inverted vertical soundings built through upward continuations of the measured data at various altitudes. The validity of the method was prior verified by tests on synthetic data. Electromagnetic data were processed and inverted using the modified AarhusINV code, with Cole-Cole modelling, in order to take into account induced polarization effects, consisting in negative voltages and otherwise skewed transients.

The integrated study of the two kinds of data has led to a better understanding of the structures at depth, even though the comparison between the magnetic and the electromagnetic models shows the different sensitivity of the two methods with respect to the geological structure at Drybones Bay.

1. Introduction

Time domain electromagnetic (TDEM) and magnetic surveys are often performed simultaneously, by a single airborne system carrying both the electromagnetic equipment and the magnetic sensor.

The opportunity of having two distinct datasets over the same area, obeying to different physical principles and thus reflecting the distribution of different physical properties within the Earth is, in principle, of great value. In fact, it makes possible an integrated study of the two types of data with a potentially strong improvement of the final interpretation model.

In this paper, we focused on modelling airborne electromagnetic (AEM) and aeromagnetic data acquired during the same survey in Canada, at Drybones Bay in the Archean Slave Province of the Northwest Territories, northern Canada. In this area, in 1994, a completely underwater kimberlite structure was discovered.

The application of geophysical methods to exploration for kimberlites and their associated diamonds began over 50 years ago with the use of magnetic and gravity measurements. Within a decade, electrical resistivity and, later, induced polarization methods were also applied to the same case. Since 1970's, both ground and airborne methods included magnetic and electromagnetic measurements (Reed and Witherly, 2007).

Kimberlite is an alkali ultramafic igneous rock, formed from the cooling of molten magma that arises from the melt of peridotite in the mantle at depth of 150–200 km. Kimberlite is composed of at least 35% olivine, together with other minerals such as mica, serpentine, and calcite (Kjaarsgard, 1996). During its upward rise into the upper mantle and overlying crust, minerals start to crystallize while the volatile gases expand and exert increasingly higher pressures on the surrounding rocks, eventually breaking some of the surrounding rock and incorporating it into the magma. The kimberlite magma may produce explosive volcanic events. In the Slave Craton and adjacent areas, these eruptions occurred from subaerial to shallow subaqueous environments; consequently, many of the resulting vent systems are vertical or steeply dipping carrot-shaped bodies, equidimensional in a plan section and tapering gradually with depth. Kimberlite intrusions tend to occur in clusters or fields, with the large-scale distribution possibly controlled by deep-seated structural features and local emplacement controlled by shallow zones of weakness, such as faults or the margins of diabase dykes (Power and Hildes, 2007).

The accepted pipe model includes three different zones from top to bottom, each with distinctive morphology and texture: the crater, diatreme and hypabyssal zones (Scott Smith, 1996).

* Corresponding author.
E-mail address: d.dimassa@dimms.it (D. Di Massa).

https://doi.org/10.1016/j.jappgeo.2018.07.004
0926-9851/

Crater kimberlites are usually basin shaped excavations formed at the surface by explosive volcanic eruptions. Crater facies kimberlites are a mixture of tuffaceous kimberlite, surrounding country rock and overlying sediments. Two main categories of rocks are found in facies of crater kimberlites: pyroclastic, deposited by eruptive forces, and epiclastic, which are the same rocks after the interaction with water. In much of the Slave Craton, crater-facies kimberlites include a significant component of shale and mudstone, sometimes with a significant component of entrained organic material. Large blocks of surrounding country rock (xenoliths) shattered from the volcanic vent margins are present in some pipes. A crater-facies kimberlite is often deeply weathered and serpentinized (Kjarsgaard, 1996).

Kimberlite diatremes are cone-shaped bodies with vertical axes and steeply inward dipping margins. Diatreme facies describe an explosive kimberlite breccia composed of fine-grained kimberlite, mantle nodules and angular fragments of the surrounding country rocks. Diatreme facies rocks are generally confined to a central breccia pipe and are generally less altered than crater facies rocks.

Hypabyssal kimberlites consist of unaltered fine-grained kimberlite with mantle nodules and rare fragments of country rock. Hypabyssal kimberlite bodies include dykes, blind intrusions and the root zones of kimberlite pipes.

In each kimberlite field, all three facies may be present at surface because of differential glacial abrasion and quarrying, and because of blind intrusions. The depth of erosion can vary over distances of a few tens of kilometres or less. Our ability to detect a kimberlite deposit by geophysical methods depends on its physical property contrasts with the host rocks. In the Slave Craton region (Canada), magnetic anomalies are commonly associated with kimberlite intrusions, having a higher magnetic susceptibility than surrounding gneisses and granites. In fact, diatreme and hypabyssal facies are readily detected. In addition, they can be affected by remanent magnetization. Instead, for crater facies, the associated magnetic anomalies can be subtle, due to the low magnetic contrast with the surrounding rocks, which in turn depends on the proportion of the non-susceptible sediments present (Power and Hildes, 2007).

In general, the electrical resistivity of kimberlites increases with depth, from crater facies through hypabyssal facies. Consequently, crater facies display the greatest contrast in electrical properties with respect to country rocks, so being well detectable with electromagnetic (EM) methods. In fact, during weathering, a highly conductive clay-rich zone forms in the top of the pipe (Macnae, 1979). Moreover, this top layer can produce a measurable induced polarization (IP) effect, which is related to ability of the material to retain electrical charges.

However, the existence of fine grained glacial-fluvial and lake sediments in the shield regions of northern Canada, with an electrical resistivity and an electrical chargeability comparable to that of the crater facies, makes the discrimination between these sources complicated. When the resistivity contrast is negligible, a potential crater facies of kimberlite target can be still identified indirectly, by assessing if the conductor persists at depth below the overburden thickness (Power and Hildes, 2007). Diatreme and hypabyssal kimberlites have usually low electrical properties contrast with respect to the country rocks. For this reason, they are almost indistinguishable from granitic or gneissic country rocks, as based on the study of the electrical resistivity or electrical chargeability distribution at depth.

In conclusion, a cooperative modelling of magnetic and electromagnetic data is expected to yield a comprehensive information on the whole kimberlite structure, improved with respect to the analysis of just one of the two datasets.

2. Inversion of magnetic data

In this paper, we performed the inversion of magnetic data along vertical profiles. This 1D method has been proposed for gravity data (Fedi and Rapolla, 1995; Vitale et al., 2016) and it is here adapted to the magnetic case, as described below. 1D methods mainly have the advantage of a low computational complexity (Auken and Christiansen, 2004; Lane et al., 2004). The inversion of electromagnetic data (next section) is, on the other hand, commonly performed with 1D models, so our common 1D approach to the inversion of the two different datasets should warrant an easy comparison between the inverted magnetic and EM models. As a matter of fact, 2D and 3D models are built by joining the results from the whole set of independent 1D inversions, resulting in an approximate 3D model.

The basic idea of the 1D algorithm for potential fields is that the physical property distribution can be deduced from the field known at different altitudes (Fedi and Rapolla, 1995). For a set of N magnetic data along a vertical direction (vertical sounding) $[P_{k1}, \ldots, P_{kj}, \ldots, P_{kN}]$, assuming that the magnetization could vary only along the vertical direction (1D assumption), the forward problem for a continuous magnetization J, linearly related to the magnetic data B, is expressed by (Blakely, 1996):

$$B(P_{kj}) = \frac{\mu_0}{4\pi}\hat{\mathbf{F}}\cdot\nabla\int_V \mathbf{J}(r)\cdot\nabla\frac{1}{|r-r_{kj}|}dv \tag{1}$$

where $\hat{\mathbf{F}}$ is the unit-vector along the inducing field direction, k is an index accounting for the horizontal position of the vertical soundings and $j = 1, \ldots, N$ refer to the data positions along each k^{th} vertical sounding.

If the source volume is subdivided in M layers, where in each of them the magnetization is homogeneous, we have:

$$B(P_{kj}) = \sum_{i=1}^{M} J_i C_{ij}(P_{kj}) \tag{2}$$

where

$$C_{ij}(P_{kj}) = \frac{\mu_0}{4\pi}\hat{\mathbf{F}}\cdot\nabla\int_{V_i}\nabla\frac{1}{|r-r_{kj}|}dv \tag{3}$$

is the unit magnetization intensity contribution due to the i^{th} prismatic layer; $[J_1, \ldots, J_i, \ldots, J_M]$ and $[V_1, \ldots, V_i, \ldots, V_M]$ are respectively the magnetizations and the volumes of the M layers.

Eq. (2) may be rewritten in vectorial notation as:

$$\mathbf{B} = \mathbf{GJ} \tag{4}$$

where $\mathbf{B}$ represents the data vector (with dimensions Nx1) of the vertical sounding, $\mathbf{J}$ represents the unknown vector (with dimension Mx1) in the source volume and $\mathbf{G}$ represents the matrix of the theoretical kernel (with dimension NxM), defined by the eq. 3.

Since the number of layers is usually greater than the data number, eq. (4) leads to solve an indeterminate linear problem.

In particular, we search the solution having the minimum Euclidean length:

$$\mathbf{J}^{\mathbf{T}}\mathbf{J} = \sum_{i=1}^{M} J_i^2 = \|\mathbf{J}\|_2^{\,2} = minimum \tag{5}$$

which satisfies some linear inequality constraints:

$$\mathbf{B} - d\mathbf{B} \le \mathbf{GJ} \le \mathbf{B} + d\mathbf{B} \tag{6}$$

$$j_L \le j_i \le j_U, \quad i = 1, \ldots, M \tag{7}$$

where $d\mathbf{B}$ is the vector of the experimental data error, j_L and j_U are the lower and the upper bounds of the model parameters.

The inequality constraints are defined based on the following strategy:

1 the unknown parameters vector must satisfy the forward model, but taking into account experimental data errors $d\mathbf{B}$;
2 the unknown parameters vector is bounded to avoid unrealistic estimates based on a priori knowledge about the subsurface geology.

This is an indeterminate problem with inequality constraints, which may be posed as:

$$\mathbf{FJ} \geq \mathbf{h} \tag{8}$$

where:

$$F = \begin{bmatrix} I \\ -I \\ G \\ -G \end{bmatrix}, h = \begin{bmatrix} J_L \\ -J_U \\ B-\delta B \\ -(B+\delta B) \end{bmatrix} \tag{9}$$

The **F** matrix, containing the identity matrix **I** (*MxM*) and the kernel **G** (*NxM*), has dimension $(2M + 2N)$ x M; the vector **h**, containing the lower and the upper bounds of model parameters and the data with the experimental errors, has dimension $(2M + 2N)$ x 1.

According to Menke (1989), the problem 8 may be transformed into:

$$\mathbf{Eu} = \mathbf{f} \rightarrow \begin{bmatrix} \mathbf{F}^T \\ \mathbf{h}^T \end{bmatrix}; \mathbf{u} = \begin{bmatrix} 0 \\ 1 \end{bmatrix} \tag{10}$$

Thus, the inversion problem reduces to find the vector **u** that minimizes:

$$\mathbf{e} = \|\mathbf{f} - \mathbf{Eu}\|_2 \; subject\ to: \mathbf{u} \geq 0 \tag{11}$$

It can be shown (Menke, 1989) that if the prediction error, **e**, is null then the constraints $\mathbf{FJ} \geq \mathbf{h}$ are inconsistent, but if $\mathbf{e} \neq 0$, constraints $\mathbf{FJ} \geq \mathbf{h}$ are consistent and the solution of the problem is:

$$J_i = -\frac{e^T{}_i}{e^T{}_{M+1}} \text{ with } i = 1 : M. \tag{12}$$

Before applying the inversion method to real cases, we tested it on synthetic magnetic dataset.

The multilevel dataset, representing the vertical soundings, were built by first computing the magnetic response of a prismatic source on a large surface at a single height, and then at a set of altitudes by upward continuation (e.g., Baranov, 1976; Blakely, 1996) of these data.

However, the upward continuation operator introduces some errors in the calculated data. This because we approximate the continuous problem with a finite and discrete set of data, on a finite region. Following Castaldo et al. (2014), the effects of this error can be mitigated by using a third-order polynomial:

$$H(z) = c_1 + c_2 z + c_3 z^2 + c_4 z^3 \tag{13}$$

where c_1, c_2, c_3 and c_4 are unknown coefficients that should be estimated during the inversion process.

For this test, we used a single prismatic source with horizontal dimensions equal to (250, 150) m and extending at depth from 100 m to 300 m. The magnetization contrast with the surrounding volume is 3 A/m. We considered in this case only that the magnetization is purely induced, with 60° inclination and 0° declination. The magnetic anomaly generated by this source and calculated at the ground surface is shown in Fig. 1.

The vertical soundings consist of magnetic data continued at 20 different altitudes from the first level at 5 m up to the last level at 100 m, with a 5 m constant vertical step. The horizontal positions of the vertical soundings are shown in Fig. 1 by the green points, while the magnetic anomalies along the profile and at different heights, are shown in Fig. 2.

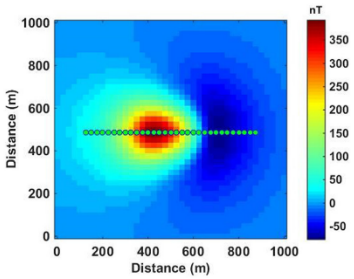

Fig. 1. Magnetic anomaly generated by a single buried prismatic source. The green dots represent the horizontal positions of the vertical soundings.

For the calculation of the kernel, a source volume has been defined with horizontal dimensions and the directions of the magnetization that agree with those of the true source. The vertical dimension of this volume is defined in such a way to completely contain the source of anomaly and it is discretized with 100 layers having an equal thickness of 10 m (Fig. 3).

To perform the inversion, for each vertical sounding, we computed, at its position along the selected profile, the kernel G_{ik}.

In this way, each vertical sounding is inverted independent of each other.

The procedure may be described as follows. Let us first consider a single vertical sounding, in Fig. 3. After inverting for the magnetization of the source layers, the result is then attributed to a set of layers sized as ΔX, i.e., the step size of the vertical soundings along the profile, and centred at the sounding position. Repeating this procedure for all the soundings we are finally allowed reconstructing an approximate 2D model of the source distribution along the profile.

For this test, we used the correct magnetization contrasts for the lower and the upper bounds, setting the lower bound equal to 0 and the upper bound equal to 3 A/m. The experimental error is set to a low value, equal to $5 \cdot 10^{-2}$ nT.

As shown in Fig. 4, the Vertical Soundings inversion can correctly recover the depth to the top of the source, and the magnetization contrast is properly estimated (the black rectangle in figure identifies the exact location of the buried body).

However, the model presents a gradual decreasing of the magnetization with the depth, so that an accurate estimation of the depth of the bottom is difficult.

From the model of Fig. 4, we calculated the estimated data along the profile, at a single altitude (in this case the first height, 5 m), and we

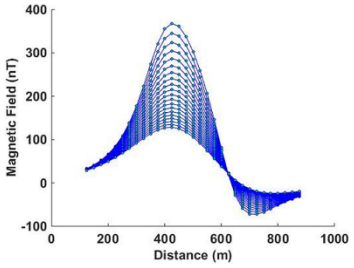

Fig. 2. Magnetic profiles at different altitudes: 5 m up to 100 m, with a 5 m constant vertical step, along the profile in Fig. 1 .

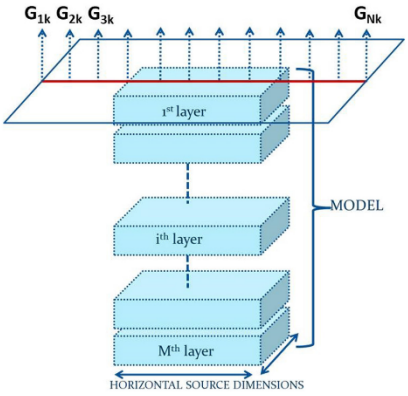

Fig. 3. Schematic picture of the finite layers forming the source volume. Dashed arrows indicate the horizontal positions of the vertical soundings. The single kernels, G_{ik} ($i = 1$–N), are computed according to the spatial coordinates of the relative sounding.

compared them with the observed data (Fig. 5). The observed data are very well reproduced all along the profile.

The good quality of this result is noteworthy, if we consider that the 2D model is built by simply joining and interpolating the 1D inverted models obtained by independent vertical soundings.

3. VTEM survey over Drybones kimberlite

We now analyse the EM and magnetic data related to the Versatile Time Domain Electromagnetic (VTEM) survey flown in 2005 over Drybones kimberlite (Kaminski et al., 2010; Kaminski and Oldenburg, 2012).

In 1991, in the Archean Slave Province of the Northwest Territories (NWT), northern Canada, a significant new kimberlite province, hosting >150 kimberlite pipes was discovered (Kretchmar, 1995).

The Slave Province is an Archean segment of the North American Craton, composed of granites, gneisses and supracrustal rocks. Sialic basement remnants, well documented in this province, include some of the oldest rocks in the world as the Acasta gneisses in the western part of the province, which have been dated at 3.96 Ga (Bowring and Housch, 1995). Metasedimentary and metavolcanic rocks of the Yellowknife Supergroup, deposited mainly between 2.71 Ga and 2.61 Ga, are the most abundant rocks of the crustal sequences. At least five swarms of Proterozoic diabase dykes cut the older units in the central Slave Province (Le Cheminant and van Breemen, 1994; Le Cheminant et al.,

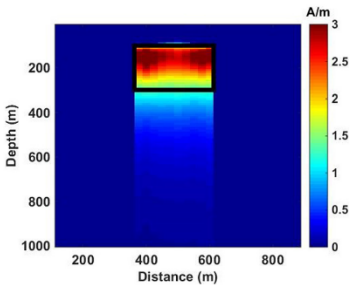

Fig. 4. Vertical Soundings inversion of the magnetic data produced by a single buried prismatic source and continued at 20 different altitudes. The black rectangle identifies the horizontal and vertical positions of the anomaly source.

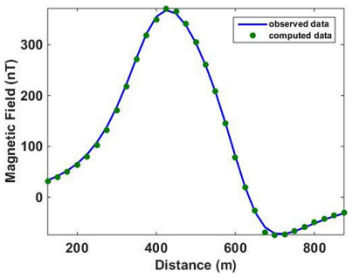

Fig. 5. Comparison between observed and computed data.

1996). The Slave Province is a classic setting for diamondiferous kimberlites: a stable Archean craton with a cool mantle root, which is necessary for the development of the diamond stability field (Haggerty, 1986; Janse, 1993). Kimberlite intrudes granites, metasedimentary rocks and, in some cases, diabase dykes. After the kimberlite emplacement, the area was covered by Laurentide ice during the Late Wisconsinan glaciation (Pell, 1995).

Middle Jurassic-, Late Ordovician-, and Cambrian-aged kimberlites have been discovered, some of which have good economic potential. Most of the kimberlites in the Slave Province do not crop out at surface; they have been identified using a combination of heavy mineral sampling, geophysical techniques and drilling. Many of the pipes are characterized by either high or low magnetic anomalies and low resistivity values.

The Drybones kimberlite is in Drybones Bay, situated approximately 45 km SE from the town of Yellowknife (NWT, Canada; Fig. 6a). The kimberlite was discovered in 1994 with a single drill hole and lies completely under the water of the Great Slave lake, at an average depth of 35–40 m; a thickness of 65–75 m of lake sediments (clay, till and sand), further covers the kimberlite (Kretchmar, 1995). The morphology of the pipe, in Fig. 6b, shows a spatially elongated intrusion (900 m by 400 m), consisting of crater, pyroclastic and diatreme facies (Kretchmar, 1995).

A geological cross-section (Fig. 6c), along the profile AA', has been drawn based on drilling information (Kretchmar, 1995).

The bedrock geology in Drybones area consists of Archean granite, granodiorite and tonalite (Kretchmar, 1995). Metasediments of Yellowknife supergroup are also present (Dunn et al., 2001). In addition, there are several known faults near the kimberlite area while a diabase dike in the northern part crosses the area from E to W (Dunn et al., 2001).

The helicopter borne geophysical survey used the VTEM system for the EM data and a caesium magnetometer for the aeromagnetic data (Witherly et al., 2004). The EM system is concentric and oriented along the vertical direction. The receiver coils were towed at a mean distance of 45 m below the aircraft. The VTEM decay was sampled using 25 time-measurement gates in the range from 0.130 to 6.340 ms after the time-off. The strength of magnetic field is measured by a magnetic sensor mounted in a separate bird, 20 m below the helicopter. The VTEM survey was carried out in 2005 along 9 flight lines spaced 100 m, on average, with orientation approximately N—S (Fig. 7). The EM data, as shown in Fig. 7, display an evident IP effect in the central part of the profiles above Drybones Bay, where the kimberlite is located. This IP effect has been identified across all flight lines, showing the existence of negative voltage data in transients.

EM data were inverted using a 1D Spatially Constrained Inversion (SCI) approach (Viezzoli et al., 2008) implemented in a modified AarhusINV code, with capability of Cole-Cole modelling (Cole and Cole, 1942; Fiandaca et al., 2012). In fact, it is common to ignore the IP effects in VTEM data by simply removing negative voltage data before the inversion. This operation can however cause a loss of resolution at

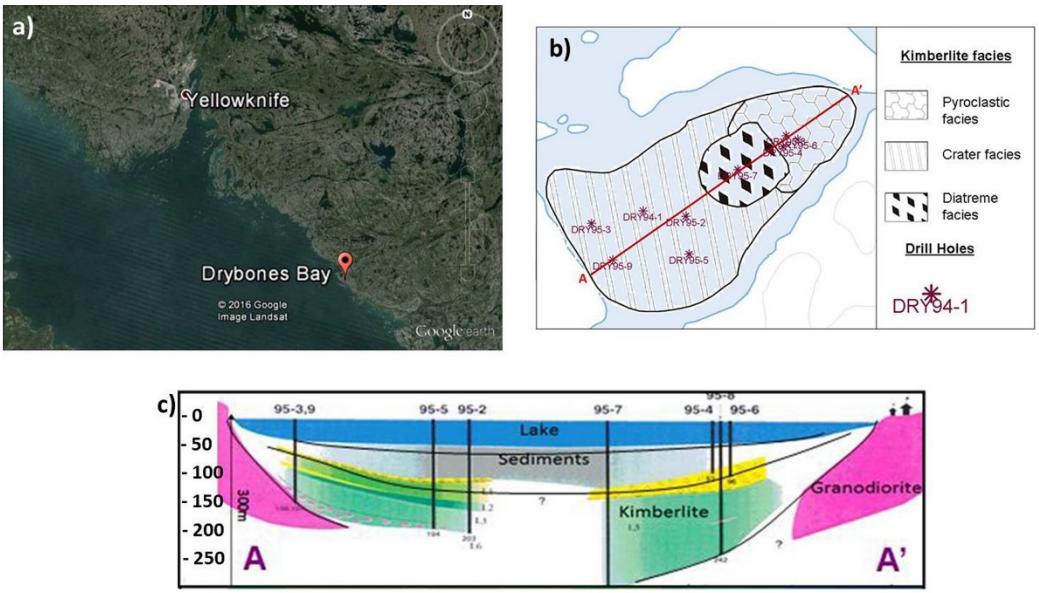

Fig. 6. (a) Geographic location of Drybones bay (Google Earth); (b) Schematic geology of the Drybones pipe below lake sediments and the locations of 1994–95 drilled wells (adapted from Kretchmar, 1995); (c) Geological cross-sections along the profile AA' based on drilling (adapted from Kretchmar, 1995).

depth and a reduction of the investigation depth. We refer to Appendix A for a brief description of the used algorithm.

The following starting model was used for the Cole-Cole inversion: $\rho = 300$ Ohm·m; $m_0 = 100$ mV/V; $\tau = 10^{-3}$ s; $C = 0.5$, where ρ is the resistivity (Ohm·m), m_0 is the chargeability (mV/V), τ is the relaxation time (s) and C is the frequency parameter (dimensionless).

The algorithm converged in 14 iterations with an average misfit of 1.29 (dimensionless, normalized by standard deviation), showing good overall data fit and so producing a model of electrical resistivity, chargeability, time constant and frequency parameter.

The inversion of VTEM data over Drybones kimberlite, carried out using Cole-Cole model is in better agreement with ZTEM inversions (Kaminski and Oldenburg, 2012, Fig. 8), than the inversion of VTEM data carried out without Cole-Cole modelling.

The comparison between the inversion results and previous inverse models recovered without considering the IP effects in TDEM data

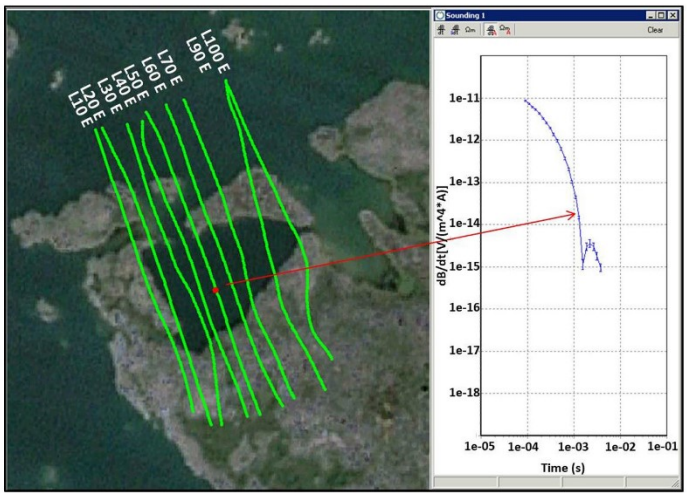

Fig. 7. evidence for IP effects in VTEM data, occurring in correspondence of the kimberlite.

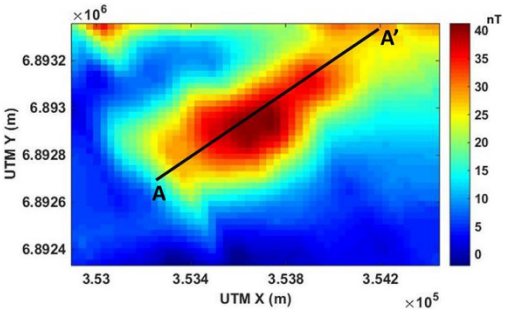

Fig. 8. Total field anomalies above the kimberlite of Drybones bay.

(Kaminski and Oldenburg, 2012, Fig. 6 and Fig. 8), confirmed the importance of modelling the IP effects. Conversely, in our case, where we have modelled the IP effects, retaining the negative voltage data, a significant increase of the recoverability of the resistivity distribution at depth is now achieved.

About magnetic data (Fig. 8), we have performed the inversion of the vertical soundings along the AA' profile located over the kimberlite. Each vertical sounding consists of magnetic data upward continued to 15 different altitudes, from the first level at 170 m above the ground up to the highest level at 240 m above the ground, with a 5 m constant vertical step (Fig. 9a).

For the calculation of the matrix kernel, we have defined a model volume with average horizontal dimensions estimated by the total horizontal derivative method (Cordell and Grauch, 1985). The total horizontal derivative method applied on the magnetic data of Fig. 8 shows complex edges for the magnetic sources (Fig. 9b). The maximum NW and SE estimated dimensions agree with what argued by Kretchmar (1995) for an elongated intrusion of 900 m by 400 m.

The vertical dimension of the model volume is defined to completely contain the source of anomaly by a maximum-depth rule (Fedi and Florio, 2013). In fact, no matter the kind of source distribution, Smith rules (Smith, 1959) or the recent method proposed by (Fedi and Florio, 2013), are very useful in determining the maximum possible depth to the source for a given anomaly.

The volume is then discretized with 100 layers of 10 m thickness to have a satisfactory depth resolution. Susceptibility constraints ($0 \le j \le 10^{-2}$) and a constraint on experimental data error ($0 \le \mathbf{dB} \le 0.5$ nT) are added to regularize the inversion.

The resistivity, the chargeability and the susceptibility models (Fig. 10) were verified against the known geology along the cross-section AA' (Fig. 6c).

The resistivity section (Fig. 10a) appears rather consistent with the outline of the different layers as determined by wells information. The yellow-red zone reflects the presence of water-saturated fine-grained sediments below the lake water, at the bottom of the bay, with low values of resistivity (< 100 Ωm). Below these formations, a lateral contact is marked between the kimberlite (yellow-green zone below the sediments, with resistivity values in the interval between 100 and 500 Ωm) and granodiorite (high values of resistivity, > 500 Ωm).

Thus, the resistivity section, obtained by modelling airborne IP produces results consistent with the available geological information. A good correlation with the shallowest part of the geological model is found, especially considering that the first time-gate of the system has a central time of 130 μs after the end of ramp, and therefore the near-surface resolution was expected to be limited.

The chargeability section (Fig. 10b) shows a high chargeable layer in correspondence to the lake sediments that, in fact, are expected to be very chargeable for the presence of fine-grained products (clay). The effect of these sediments does not allow an easy detection of the crater facies of the kimberlite that, usually, can produce an IP effect because of weathering, (Macnae, 1979).

The Vertical Soundings inversion of the magnetic data along the AA' profile allows recovering a model with high susceptibilities, possibly associated with the kimberlite body (Fig. 10c). In fact, the estimated depths (top of the kimberlite at about 50 m above sea level) are consistent with the geological information derived by the available drill holes, from which the top of the kimberlite was detected at depth of 100–110 m from the surface. The susceptibility model shows that the magnetized body is clearly separated from the overlying non-magnetic sediments and lake water.

The most magnetized material should mark the shallowest portion of the kimberlite that is subject to geochemical alteration (Kaminski and Oldenburg, 2012). In fact, the mineralogical analysis of the Drybones kimberlite samples revealed signs of alteration due to elevated contents of Cr and Nb, as well as due to low totals of TiO_2 in ilmenites (Dunn et al., 2001). This geochemical alteration may have a strong influence on the magnetic properties of the kimberlite, causing an increase of the magnetization (Dunn et al., 2001).

The comparison between the EM and the magnetic models revealed, in this case, the different sensitivity of the two methods with respect to

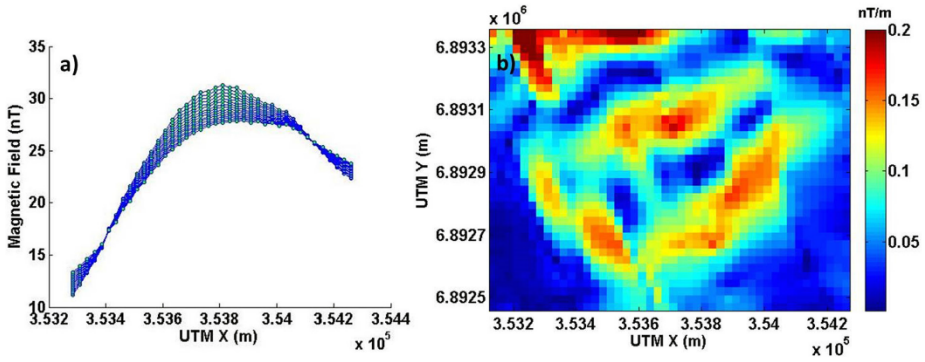

Fig. 9. (a) Behaviour of the magnetic data at different altitudes, along the AA' profile. The green dots represent, for each altitude, the horizontal positions of the data and then the individual vertical soundings; (b) total horizontal derivative of magnetic data above the kimberlite.

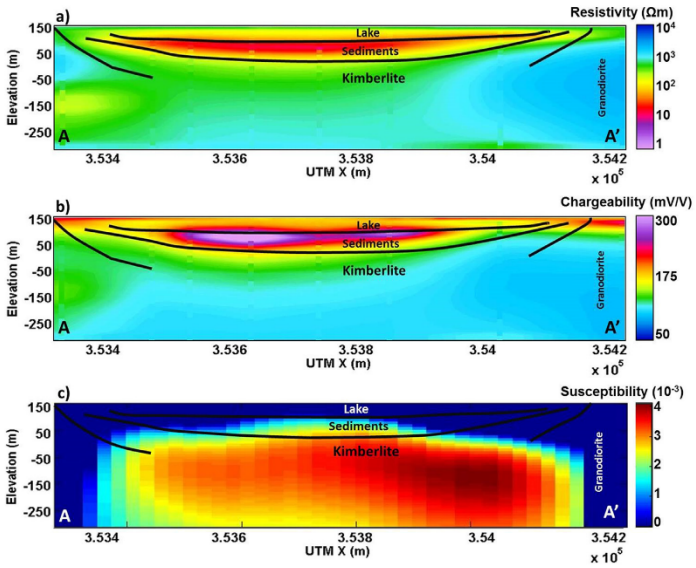

Fig. 10. (a) Resistivity section and (b) chargeability section recovered by SCI inversion using Cole-Cole model along the AA' profile; (c) susceptibility section recovered by Vertical Soundings inversion of aeromagnetic data along the AA' profile.

the investigated geological structures. This allowed a complete characterization of the studied area at Drybones kimberlite but, at same time, it could imply greater difficulty in setting up a true joint inversion, where the physical properties need to be linked in some way by means of petrophysical or empirical relationships (Dell'Aversana, 2014).

4. Conclusions

We showed and discussed the modelling of TDEM and aeromagnetic data related to a helicopter-borne survey flown in 2005 over Drybones Bay, Northwest Territories, Canada, where in 1994 a completely underwater kimberlite structure was discovered.

The evidence of IP effects in the measured EM data, mainly resulting in negative values of the voltage, leaded us using a modified AarhusInv code for their inversion, implementing a Cole-Cole modelling. The presented results suggest a correct hydrogeological interpretation of the cross-section, with lake water and clay-sediment thicknesses supported by drilling results. Clay material appears in our model as conductive and chargeable, while the lake water does not show any chargeable properties. The results presented in this paper appear to be more interpretable and provide better data fit than previous inversion attempts, where the inversion was carried out without considering the IP effects in the TDEM data. The inversions of TDEM data, including the Cole-Cole modelling, can provide an improved recovery of electrical resistivity and chargeability at depth. The extraction of chargeability may be a powerful tool in kimberlite exploration for its key role in mapping crater facies of kimberlites and clay alteration zones, which may be associated with kimberlites.

To better compare the results from magnetic inversion to that of EM data, usually performed on the basis of 1D inversion, the aeromagnetic data were also modelled by a new 1D method allowing the inversion of vertical data soundings. The vertical soundings consisted of magnetic data at different altitudes while the forward problem consisted in assuming a volume of layers of different magnetizations. The volume is finite vertically and horizontally. The inversion of the vertical soundings was performed including inequality constraints on the model parameters, well reflecting the a-priori knowledge on the studied area. This method presents a reduced computation complexity and even if the algorithm is dealing with a mono-dimensional vertical inversion and the 2D model is built approximating multi-set of 1D models, we obtained a good fitting between the measured and the estimated data along all the profiles.

The integrated study of the results obtained by separately inversion of the TDEM and the aeromagnetic data shows that the two methods have not the same sensitivity with respect to the geological structures in this area. In fact, while the most conductive/chargeable structures are found in correspondence of the water lake and the uppermost lake sediments, the most magnetized structure coincides with the depths to the top of the kimberlite sequence, showing susceptibility values much higher of the poorly-to-not magnetic overlying structures.

Nevertheless, their ability in characterizing sources at different depth ranges of the Drybones Bay, is definitely useful to improve the final interpretation model. All the geological structures at Drybones Bay are well retrieved by the inversion processes and are in very good agreement with the drill hole information available for this area.

Acknowledgements

The authors are highly thankful to Geotech, Ltd. for providing the VTEM data for research purposes.

Appendix A. Laterally constrained inversion for IP parameters

The induced polarization (IP) effects in TDEM data is usually observed in the data derived from coincident-loop systems, showing abnormal fast EM decay with the existence of negative values of the voltage. This phenomenon can significantly alter the shape of the transient and, if not considered, may lead to recover false structure, with incorrect conductivity-thickness parameters (Viezzoli et al., 2015).

Over the years, the handling of the IP effects in TDEM data has kept its relevance with a further interest from ground to airborne data (Smith and Klein, 1996; Kratzer and Macnae, 2012). For airborne data

the appearance of IP effects is closely related to the flight height and to the waveform shape (Viezzoli et al., 2013). The increase of flight height causes a delay in the appearance of the IP effects, which can also disappear if the transition occurs below the noise level. The duration of turn-off controls the injection time of the induced currents in the ground that in turn controls its effective charging. Therefore, a slower turn-off current causes the IP effects to dominate over the induced currents at earlier times.

Viezzoli et al., 2013 have also investigated the dependence of the IP effects in the AEM systems, varying the Cole-Cole parameters and they concluded that the values of resistivity and chargeability are positively correlated with an increase of IP effects, i.e. the IP effects appear at earlier times, while for C and τ they did not observe a similar behavior. The increase of their values is not always followed by an appearance of the IP effects at earlier times.

The possibility of extracting chargeability information from transient EM data, that can have a significant impact to mineral exploration, has provided several suggestions to handle the IP effect with Cole-Cole model.

A polarizable earth may be described using an impedance model derived from the empirical Cole-Cole model (Cole and Cole, 1942):

$$Z(\omega) = \rho\left[1 - \frac{m_0}{10^3}\left(1 - \frac{1}{1 + (i\omega\tau)^c}\right)\right] \tag{A.1}$$

Eq. A.1 introduces a complex impedance relationship, as a function of four parameters: ρ (Ωm) is the electrical resistivity, m_0 (mV/V) is the chargeability, C (dimensionless) is the frequency parameter, describing the variation of phase with frequency and τ (s) is the relaxation time.

Fiandaca et al., 2012) have introduced a 1D algorithm allowing to solve for complex impedance model; here the Cole-Cole model (eq. A.1) represents the forward mapping kernel. The four Cole-Cole parameters are the unknowns of the inverse problem which are simultaneously obtained in a unique inversion process, where the relationship between parameters is maintained at all times. The inversion has been implemented using the 1D laterally constrained inversion (LCI) scheme (Auken et al., 2005): a set of vertical and lateral constraints, tied together the parameters of the neighboring soundings along the flight lines for LCI, retrieving 2D sections in quasi-layered environments (Fig. A.1).

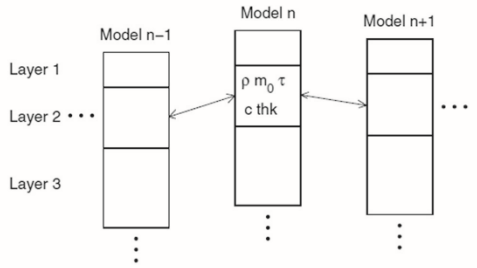

Fig. A.1. Model parameters with lateral constraints (adapted from Fiandaca et al., 2012).

The LCI inversion algorithm is described in detail in Auken and Christiansen (2004). It allows performing the inversion of large data set, where the parameters of the earth model for each sounding are connected laterally by means of lateral constraints, defining a specified variance of the model parameters. The lateral constraints can be considered as a-priori information on the geological variability in the area of measurements. In LCI, the connection of the soundings occurs along a profile, producing quasi-2D images of the subsurface with smooth lateral transitions. The constraints allow the migration of information from one model to neighboring models, helping to resolve areas with poorly constrained parameters or soundings particularly noisy.

The LCI is a full non-linear damped least squares inversion based on an exact forward solution, modelling the instrumentation's system transfer function (STF). The solutions developed by Ward and Hohmann (1988) are used as the basis for the forward modelling algorithm. Modelling the STF also includes low-pass filters (Effersø et al., 1999), and turn-on/turn-off ramps (Fitterman and Anderson, 1987).

The inversion problem can be written:.

$$\begin{bmatrix}\mathbf{G}\\ \mathbf{R}\end{bmatrix}\mathbf{dm_{true}} = \begin{bmatrix}\mathbf{D_{obs}}\\ \mathbf{dr}\end{bmatrix} + \begin{bmatrix}\mathbf{e_{obs}}\\ \mathbf{e_r}\end{bmatrix} \tag{A.2}$$

where dDobs denotes the observed data, eobs is the error on the observed data, G is the Jacobian and contains all partial derivatives of the mapping, dr are the constraints, er is the error on the constraints with 0 as expected value and R is the roughening matrix, containing 1's and − 1's for the constrained parameters, and 0 in all other places.

The covariance matrix for the joint observation error, which it is assumed to be a diagonal matrix, becomes:.

$$\mathbf{C'} = \begin{bmatrix}\mathbf{C_{obs}} & 0\\ 0 & \mathbf{C_R}\end{bmatrix} \tag{A.3}$$

if any a-priori information on model parameters, allowing to reduce the ambiguity on the inverse models, are available, they can be added, following Jackson (1979), as an extra row ($\mathbf{m_{prior}}$) to the system A.2 and the a-priori model variance ($\mathbf{C_{prior}}$) is described in covariance matrix.

In a compact form, Eq. A.2 is rewritten as:.

$$\mathbf{G'dm_{true}} = \mathbf{dD'} + \mathbf{e'} \tag{A.4}$$

the model estimate is (Menke, 1984):

$$\mathbf{dm_{est}} = \left(\mathbf{G'^T C'^{-1} G'}\right)^{-1}\mathbf{G'^T C'^{-1} dD'} \tag{A.5}$$

that minimizes the objective function:

$$\mathbf{Q} = \left(\frac{1}{N+A}\left[\mathbf{dD'^T C'^{-1} dD'}\right]\right)^{\frac{1}{2}} \tag{A.6}$$

The algorithm inverts all the soundings simultaneously, considering all the data and the lateral constraints. A common objective function is thus minimized. The output model, including all the 1D soundings, is balanced between the constraints, the physics and the data.

Following this approach, some experiments on synthetic AEM data were presented by Viezzoli et al. (2013), showing how 1D inversion is able to recover the unknown parameters and which is their standard deviation, for a chargeable half-space. These tests have highlighted that, in general, the resistivity and chargeability parameters are well-resolved, displaying also some degree of coupling. Low standard deviations are usually associated to the frequency parameter C, for which a low value of starting model is preferable to obtain better convergence and sensitivity. τ parameter is the worst resolved and in addition it has been noted that a starting value close to real value is needed to avoid a negative influence on all the other parameters.

References

Auken, E., Christiansen, A.V., 2004. Layered and laterally constrained 2D inversion of resistivity data. Geophysics 69, 752–761.
Auken, E., Christiansen, A.V., Jacobsen, B.H., Foged, N., Sørensen, K.I., 2005. Piecewise 1D laterally constrained inversion of resistivity data. Geophys. Prospect. 53, 497–506.
Baranov, W., 1975. Potential Fields and their Transformations in Applied Geophysics. Gebruder Borntraeger, Berlin.
Blakely, R.J., 1996. Potential Theory in Gravity and Magnetic Applications. Cambridge University Press, Cambridge.

Bowring, S.A., Housch, T., 1995. The Earth's early evolution. Science 269, 1535–1540.
Castaldo, R., Fedi, M., Florio, G., 2014. Multiscale estimation of excess mass from gravity data. Geophys. J. Int. 197, 1387–1398.
Cole, K.S., Cole, R.H., 1942. Dispersion and absorption in dielectrics. J. Chem. Phys. 9-4, 341–351.
Cordell, L., Grauch, V.J.S., 1985. Mapping basement magnetization zones from aeromagnetic data in the San Juan basin. In: Hinze, W.J. (Ed.), The Utility of Regional Gravity and Magnetic Anomaly Maps. Society of Exploration Geophysicists, New Mexico, pp. 181–197.
Dell'Aversana, P., 2014. Integrated Geophysical Models. EAGE Publications bv, HOUTEN The Netherlands.
Dunn, C.E., Smith, D., Kerr, D.E., 2001. Biogeochemical survey of the Drybones Bay area, NWT using outer bark of black spruce. Geological Survey of Canada, Open File. 3919.
Effersø, F., Auken, E., Sørensen, K.I., 1999. Inversion of band-limited TEM responses. Geophys. Prospect. 47, 551–564.
Fedi, M., Florio, G., 2013. Determination of the maximum-depth to potential field sources by a maximum structural index method. J. Appl. Geophys. 88, 154–160.
Fedi, M., Rapolla, A., 1995. Vertical Gravity an Magnetic Soundings: forward problem formulation and data inversion. Boll. Geofis. Teor. Appl. Vol. XXXVII, N.147.
Fiandaca, G., Auken, E., Christiansen, A.V., Gazoty, A., 2012. Time-domain induced polarization: full-decay forward modelling and 1D laterally constrained inversion of Cole-Cole parameters. Geophysics 77, E213–E225.
Fitterman, D.V., Anderson, W.L., 1987. Effect of transmitter turn-off time on transient soundings. Geoexpl. 24, 131–146.
Haggerty, S.E., 1986. Diamond genesis in a multiply-constrained model. Nature, Volume 320, 34–38.
Jackson, D.D., 1979. The use of a priori information to resolve non-uniqueness in linear inversion. Geophys. J. R. Astron. Soc. 57, 137–157.
Janse, A.J.A., 1993. The Aims and Economic Parameters of Diamond Exploration. Diamonds, Exploration, Sampling and Evaluation, Prospectors and Developers Association of Canada, pp. 173–184.
Kaminski, V., Oldenburg, D., 2012. The geophysical study of Drybones kimberlite using 3D time domain EM inversion and 3D ZTEM inversion algorithms: 22nd ASEG Geophysical Conference and Exhibition, Extended Abstracts. pp. 1–4.
Kaminski, V., Legault, J.M., Kumar, H., 2010. The Drybones kimberlite: a case study of VTEM and ZTEM airborne EM results, 21ST ASEG International Geophysical Conference and Exhibition, Extended Abstract (22-25 August 2010, 4 ppSydney, Australia).
Kjarsgaard, B.A., 1996. Kimberlites. In: LeCheminant, A.N., Richardson, D.G., DiLabio, R.N. W., Richardson, K.A. (Eds.), Searching for Diamonds in Canada. 3228. Geological Survey of Canada, Open File, pp. 29–37.
Kratzer, T., Macnae, J., 2012. Induced polarization in airborne EM. Geophysics 77 (5), E317–E327.
Kretchmar, U., 1995. Drill Report on the Drybones Bay Kimberlite Property. Drybones Bay, Great Slave Lake, District of MacKenzie, Northwest Territories, Canada.
Lane, R., Brodie, R., Fitzpatrick, A., 2004. Constrained inversion of AEM data from the lower Balonne area, southern Queensland, Australia. Lower Balonne airborne geophysical project. CRC LEME OPEN FILE REPORT 163.
Le Cheminant, A.N., van Breemen, O., 1994. U-Pb ages of Proterozoic dyke swarms, lac de Gras area, N.W.T.: evidence for progressive break-up of an Archean supercontinent. GAC Programs with Abstracts 19, p. 62.
Le Cheminant, A.N., Heaman, L.M., van Breemen, O., Ernst, R.E., Baragar, W.R.A., Buchan, K. L., 1996. Mafic magmatism, mantle roots, and kimberlites in the slave craton. In: Le Cheminant, A.N., Richardson, D.G., DiLabio, R.N.W., Richardson, K.A. (Eds.), Searching for Diamonds in Canada. 3228. Geological Survey of Canada, Open File, pp. 161–169.
Macnae, J.C., 1979. Kimberlites and exploration geophysics. Geophysics 44 (8), 1395–1416.
Menke, W., 1984. Geophysical data analysis, discrete inverse theory. 260. Academic Press.
Menke, W., 1989. Geophysical data analysis: Discrete inverse theory. Academic Press (Elsevier).
Pell, J.A., 1995. Kimberlites in the Slave Structural Province. Northwest Territories: A Preliminary Review. EGS 1995–12. NWT Geological Mapping, Indian and Northern Affairs Canada (20 pages).
Power, M., Hildes, D., 2007. Geophysical strategies for kimberlite exploration in northern Canada. Geophysical case histories. In: Milkereit, B. (Ed.), Paper 89. Proceedings of Exploration 07: Fifth Decennial International Conference on Mineral Exploration, pp. 1025–1031.
Reed, L.E., Witherly, K.E., 2007. 50 years of kimberlite geophysics, a review. In: Milkereit, B. (Ed.), Proceedings of Exploration 07: Fifth Decennial International Conference on Mineral Exploration, pp. p679–p689.
Scott Smith, B.H., 1996. Kimberlites. In: Mitchell, R.H. (Ed.), Undersaturated Alkaline Rocks: Mineralogy, Petrogenesis and Economic Potential. Vol. 24. Mineralogical Association of Canada, Short Course Volume, pp. 217–244.
Smith, R.A., 1959. Some depth formulae for local magnetic and gravity anomalies. Geophys. Prospect. 7, 55–63.
Smith, R.S., Klein, J., 1996. A special circumstance of airborne induced polarization measurements. Geophysics 61, 66–73.
Viezzoli, A., Christiansen, A.V., Auken, E., Sørensen, K., 2008. Quasi-3D modeling of airborne TEM data by spatially constrained inversion. Geophysics 73, 105–113.
Viezzoli, A., Fiandaca, G., Segio, S., Auken., E., 2013, Constrained Inversion of IP Parameters from Airborne EM Data , ASEG-PESA Expanded abstracts, Melbourne, Australia.
Viezzoli, A., Kaminski, V., Cooper, Y.L., Hardy, L., Fiandaca, G., 2015. Improving Modelling of AEM Data Affected by IP, Two Case Studies. ASEG-PESA Expanded abstracts, Perth, Australia.
Vitale, A., Fedi, M., Di Massa, D., Florio, G., 2016. A New Algorithm for Inversion of 1D Vertical Soundings of Potential Field Anomalies. 78th EAGE Conference & Exhibition 2016 Wien (Austria).
Ward, S.H., Hohmann, G.W., 1988. Electromagnetic theory for geophysical applications. In: Nabighian, M.N. (Ed.), Electromagnetic methods in applied geophysics: SEG. 131–311.
Witherly, K., Irvine, R., Morrison, E., 2004. The Geotech VTEM Time Domain helicopter EM System, In Expanded Abstract of 74th Ann. International meeting SEG, Denver. pp. 1217–1220 (Colorado (USA)).

4. IMAGING METHODS: the scaling function

This paragraph shows the theoretical background of the scaling function method, following the demonstration given by Fedi (2007) for the gravity field of a pole source. These quantities are important to understand the homogeneous properties of potential fields. Let us assume a cartesian coordinate system with the z-axis negative downward.

The gravity field $f(\mathbf{r})$ due to a homogeneous sphere at $\mathbf{r}_0(x_0, y_0, z_0)$ with density M=1 and normalized by the gravity constant k, can be expressed as:

$$f(\mathbf{r}) = \frac{(z - z_0)}{\|\mathbf{r} - \mathbf{r}_0\|_2^3} \tag{35}$$

If the source is at $r_0(0,0,z_0)$ and the field is measured at x=x_0, y=y_0 we have:

$$f(z) = \frac{1}{(z - z_0)^2} \tag{36}$$

The scaling function can be defined as the derivative of the logarithm of the field f with respect to log(z):

$$\tau(z) = \frac{\partial log[f(z)]}{\partial \log(z)} \tag{37}$$

For the above-mentioned example of the gravity field, the scaling function τ is:

$$\tau(z) = -\frac{2z}{z - z_0} \tag{38}$$

We note that the scaling function has the important property of not being dependent on the source property, such as density or magnetization intensity. If we now consider a k^{th} order of derivation for the field f we can express the scaling function as:

$$\tau_k(z) = \frac{\partial log[f_k(z)]}{\partial \log(z)} = -\frac{(k+2)z}{z - z_0} \tag{39}$$

From the equation 38 we can see that $\tau(z)$ is singular at $z=z_0$ in the source region, but at $z=-z_0$ we have that $\tau(z) = -1$, and it follows that:

$$\left.\frac{\partial\{log[f(z)] + \log(z)\}}{\partial z}\right|_{z=-z_o} = \left.\frac{\partial zf}{\partial z}\right|_{z=-z_o} = 0 \tag{40}$$

From equation 40 we can understand that the function zf has a maximum at $z=-z_0$. This means that, scaling the gravity field with a power law of the altitude z and exponent equal to 1, we can have a scaled gravity field, W_g:

$$W_g = fz \tag{41}$$

having a maximum at $x=x_0$, $y=y_0$ and $z=-z_0$. Obviously, the maximum is due to the fact that we have assumed a positive density contrast. If we choose a negative density contrast we will have a minimum at the point $\mathbf{r}(x=x_0, y=y_0, z=-z_0)$. Moreover, instead to express the function W_g as function of $\mathbf{r}$, we can express W_g as function of (x_0, y_0, z_0).

We can generalize the scaling function formula to any k^{th} order vertical derivative of the field f_k, and to any kind of homogeneous source; in fact, starting from the k^{th} order derivative of the gravity field, of homogeneity degree n,

$$f_k(x = x_0, y = y_0, z) = \frac{1}{(z - z_0)^{N+k}} \tag{42}$$

Where $N=-n$, we get:

$$\tau_k(z) = \frac{\partial log[f_k(z)]}{\partial \log(z)} = -\frac{(k + N)z}{z - z_0} \tag{43}$$

At $z=-z_0$ we will have:

$$\tau_k(-z_0) = -\frac{(k + N)}{2} \tag{44}$$

Hence, the general scaled function, W_k, which we call DEXP transformation, has an extreme point at the source position $x=x_0$, $y=y_0$ and $z=-z_0$ and it can be expressed as:

$$W_k = f_k z^{\frac{k+N}{2}} \tag{45}$$

We have described the DEXP transform for the field and its derivatives of a simple pole source. Obviously real sources generate a field that cannot be explained by something like a simple pole source, unless the field is measured at a great distance. So, we could define real sources as source distributions within finite volumes with arbitrary shapes (**Fedi, 2007**).

But, in the majority of the cases, the source complexity can be simplified to semi-infinite volume-less shapes. For example, we can see pipes, ridges, valleys, tunnels, volcanic necks as infinite cylinders. These simple shape bodies are generally defined as one-point sources, meaning that we need the coordinates of just one singular point, i.e. the center or the edge, to define them (**Stavrev, 1997; Fedi, 2007**).

4.1. Estimating the inhomogeneous depth weighting exponent β

Our main goal was to build an inhomogeneous depth weighting function (eq. 34). The key point is to estimate the depth weighting exponent β for every single point of our domain.

The insight from Cella and Fedi (2012), that links β to the homogeneity degree n and the scaling function method, will help

Assuming again, for the moment, an ideal source, it is easy to show that the scaling function τ (equation 37) could be written, in scalar notation, as:

$$\tau_k(\mathbf{r},\boldsymbol{\rho}^*) = \frac{\partial log f_k}{\partial \log(x-\xi^*)} + \frac{\partial log f_k}{\partial \log(y-\eta^*)} + \frac{\partial log f_k}{\partial \log(z-\zeta^*)}$$

$$\tau_k(\mathbf{r},\boldsymbol{\rho}^*) = \frac{1}{f_k}\frac{\partial f_k}{\partial x}(x-\xi^*) + \frac{1}{f_k}\frac{\partial f_k}{\partial y}(y-\eta^*) + \frac{1}{f_k}\frac{\partial f_k}{\partial z}(z-\zeta^*) \quad (46)$$

where $\mathbf{r}(x,y,z)$ and $\boldsymbol{\rho}^*(\xi^*,\eta^*,\zeta^*)$ are the positions of observation point P and source S.

Equation 46 could be written in a different form, as:

$$\tau_k(\mathbf{r},\boldsymbol{\rho}^*) = \boldsymbol{\nabla}\log(f_k)\cdot\mathbf{r} - \frac{\partial log f_k}{\partial x}\xi^* - \frac{\partial log f_k}{\partial y}\eta^* - \frac{\partial log f_k}{\partial z}\zeta^* = \quad (47)$$

$$= a - b\xi - c\eta - d\zeta$$

Where;

$$a = \nabla \log(f_k) \cdot \mathbf{r}, \quad b = \frac{\partial log f_k}{\partial x}, \quad c = \frac{\partial log f_k}{\partial y}, \quad d = \frac{\partial log f_k}{\partial z}.$$

Now, we can define the differential scaling function as the gradient Σ of the scaling function τ:

$$\Sigma = \nabla \tau \tag{48}$$

with components:

$$\Sigma_x = \frac{\partial \tau}{\partial x} = \frac{\partial a}{\partial x} - \frac{\partial b}{\partial x}\xi^* - \frac{\partial c}{\partial x}\eta^* - \frac{\partial d}{\partial x}\zeta^*$$

$$\Sigma_y = \frac{\partial \tau}{\partial y} = \frac{\partial a}{\partial y} - \frac{\partial b}{\partial y}\xi^* - \frac{\partial c}{\partial y}\eta^* - \frac{\partial d}{\partial y}\zeta^* \tag{49}$$

$$\Sigma_z = \frac{\partial \tau}{\partial z} = \frac{\partial a}{\partial z} - \frac{\partial b}{\partial z}\xi^* - \frac{\partial c}{\partial z}\eta^* - \frac{\partial d}{\partial z}\zeta^*$$

Or in matrix notation:

$$\Sigma = \boldsymbol{\alpha} + \boldsymbol{\Gamma}\boldsymbol{\rho}^* \tag{50}$$

Where:

$$\boldsymbol{\alpha} = \nabla a$$

$$\boldsymbol{\Gamma} = \begin{bmatrix} \frac{\partial b}{\partial x} & \frac{\partial c}{\partial x} & \frac{\partial d}{\partial x} \\ \frac{\partial b}{\partial y} & \frac{\partial c}{\partial y} & \frac{\partial d}{\partial y} \\ \frac{\partial b}{\partial z} & \frac{\partial c}{\partial z} & \frac{\partial d}{\partial z} \end{bmatrix} \tag{51}$$

Since that for homogeneous fields we have:

$$\tau_k(\mathbf{r}, \boldsymbol{\rho}^*) = -n \tag{52}$$

it will be:

$$\Sigma_k(\mathbf{r}, \boldsymbol{\rho}^*) = 0 \tag{53}$$

For this reason, we can solve the system deduced from equation 50 at every point $\mathbf{r}$ of our field domain, to estimate the source parameters ξ^*, η^*, ζ^*. For every position in the space $\mathbf{r}_i$ (x_i, y_i, z_i) we will assume $\xi^*=x_i$ and $\eta^*=y_i$, assuming that we are

estimating the homogeneity degree *n* due to a one-point source. Knowing them and substituting them in equation 52, we may estimate the degree of homogeneity *n* and β, according to Cella and Fedi (2012) who established the relationship of *β(x,y,z)* with the structural index *N as:*

$$\beta(x,y,z) = N(x,y,z) = -n(x,y,-z) \quad (54).$$

So, we can form a *β(x,y,z)* function, to be used to create a inhomogeneous depth weighting function *w(x,y,z)*, according to equation 34:

$$w(x,y,z) = \frac{1}{z^{\beta(x,y,z)/2}}.$$

For a given *k*-order field derivative of the magnetic field we will estimate the exponent of the weighting function β as

$$\beta(x,y,z) = N(x,y,z) = -(n(x,y,-z) + k) \quad (55)$$

Similar formulas occur in the gravity case, replacing the magnetic field and its *k*-order derivatives by the vertical (or horizontal) gradient of the gravity field and its k-order derivatives, respectively.

The flowchart below summarizes the whole new approach proposed.

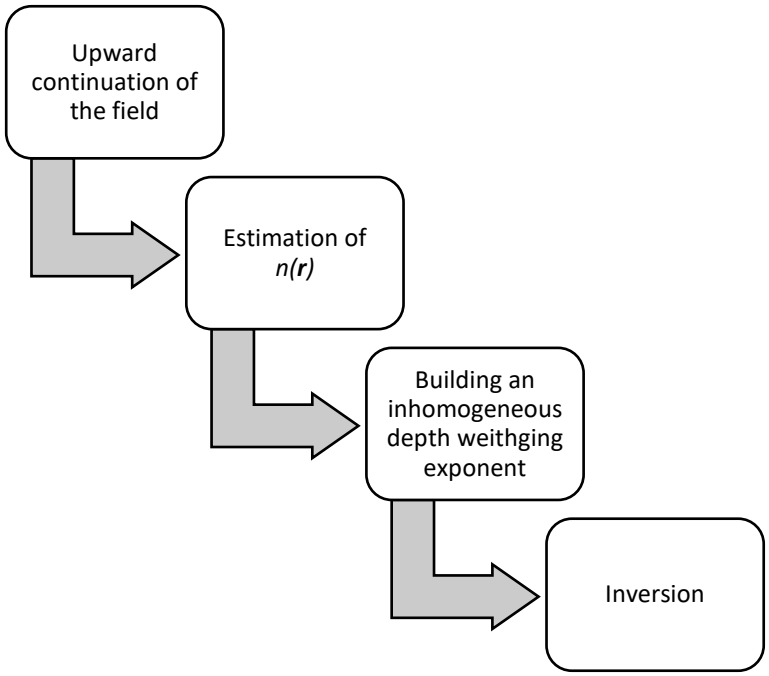

5. 2D Inversion with inhomogeneous depth weighting function

To test the effect of the inhomogeneous depth weighting function we started by running some 2D synthetic models.

Moreover, to be sure that the estimation of the homogeneity degree in every single point of our domain was correct, we started by using an analytical approach and then we moved to a numerical approach.

We considered the magnetic field, but we had same results by using gravity field.

The idea of using an inhomogeneous depth weighting function was, for the very first time, explored by Daniela Mastellone in her PhD thesis.

Our work started on replicate some of those 2D cases, while improving the estimates of $\beta(x,y,z)$, and then using the new approach to 3D domain.

5.1. 2D horizontal line of dipoles

We started by using a homogeneous 2D source: a horizontal line of dipoles. From now on, for the sake of graphical simplicity, we assume the z-axis positive downward.

The analytical formula that express the magnetic field due to this kind of source is well known (**Telford, 1990, pg.92**).

So, knowing a formula, is easier to calculate derivatives and the scaled field at several level.

According to the discussed workflow we calculated the scaling function in a 2D domain as:

$$\tau_k(\mathbf{r},\boldsymbol{\rho}^*) = \frac{1}{f_k}\frac{\partial f_k}{\partial x}(x-\xi^*) + \frac{1}{f_k}\frac{\partial f_k}{\partial z}(z-\zeta^*) \tag{56}$$

In the same way, equation 51 becomes:

$$\boldsymbol{\alpha} = \boldsymbol{\nabla} a = \frac{\partial a}{\partial x} + \frac{\partial a}{\partial z}$$

$$\boldsymbol{\Gamma} = \begin{bmatrix} \frac{\partial b}{\partial x} & \frac{\partial d}{\partial x} \\ \frac{\partial b}{\partial z} & \frac{\partial d}{\partial z} \end{bmatrix} \tag{57}$$

In this 2D case we will get $\beta(x,z)$ that is used to create a inhomogeneous depth weighting function $w(x,z)$ for a 2D domain.

The analytical example was built by a line of dipoles located at $\xi^* = 100$ m and $\zeta^* = -15$ m, with unitary magnetization intensity. Inclination and declination of the main and induced fields are the same (Inc = 90°; Dec = 0°). The 2D domain along x, goes from 1 to 200 m with 1 m step size and along z from 1 to 31 m.

The highest altitude was chosen according to the maximum depth that we want to investigate in the inversion process.

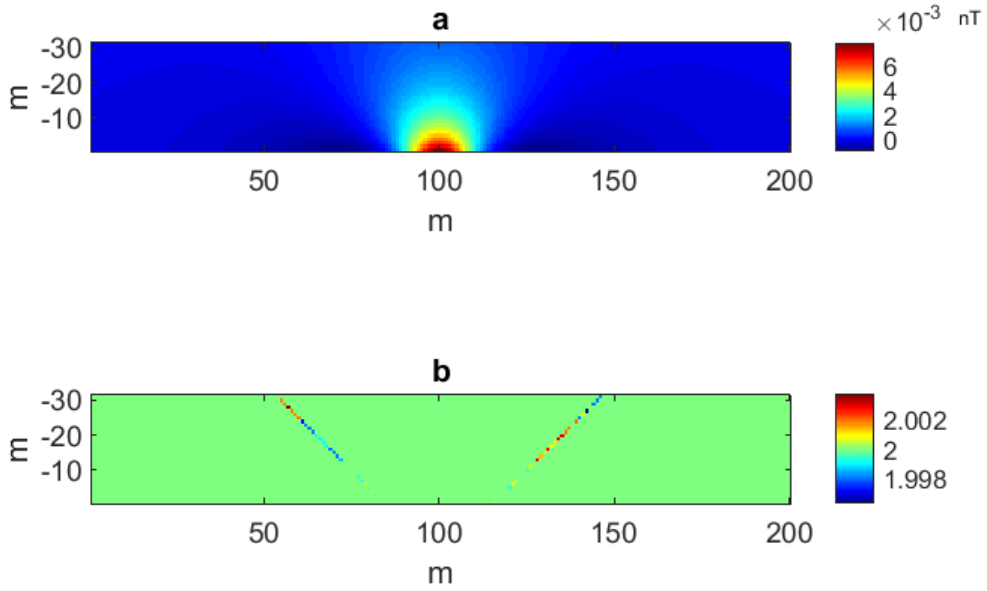

Figure 3: (a) Magnetic Field due to a line of dipoles, scaled at different altitudes, from 1 to 31 m. (b) β(x,z) function estimated for the entire domain.

In figure 3b, it is possible to notice some instability in the estimates of $\beta(x,z)$, along two lines. Even if the difference from those instabilities and the expected value is really small, these phenomena could be larger in numerical cases.

Anyway, looking at the estimates of the β values within our domain we can say that the approach is working properly, because we expected a constant value of 2 due to the homogeneity property of this particular field.

Obviously, in this case, we do not expect any difference in the inversion results by using homogeneous or inhomogeneous approach. In fact, as we can see from figure 4, the two different approaches lead to the same result.

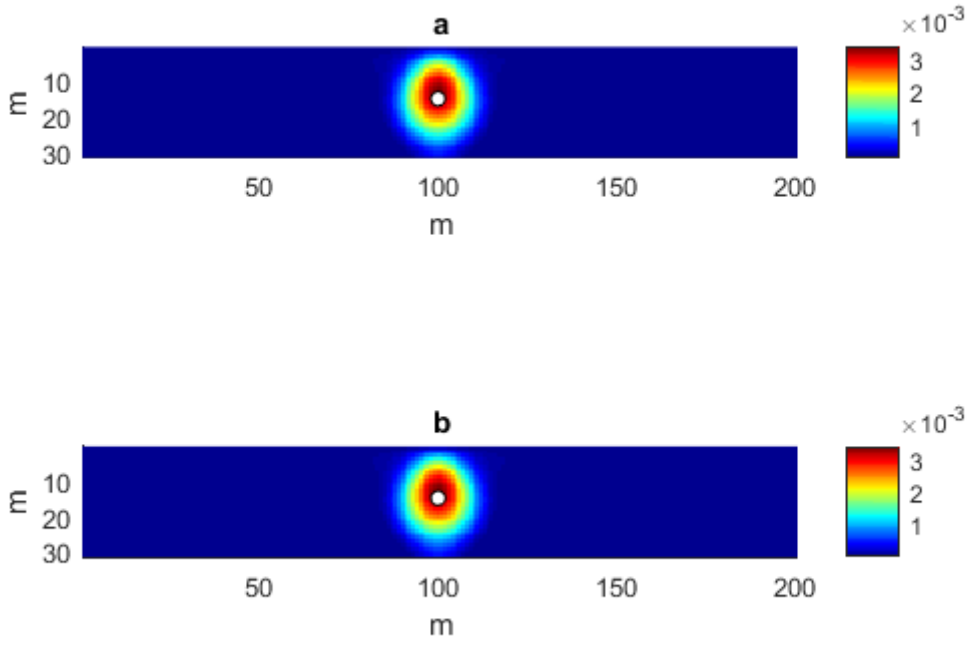

Figure 4: (a)Inversion model result by using β = 2. (b) Inversion model result by using β(x,z), shown in figure 1b. White dot highlight the true source position.

5.2. 2D Single buried body (prismatic source)

At this point we can move to numerical cases, applying the same procedure to a single buried body model. In this case we have no more a homogeneous field, so that *n* and therefore *β* values are expected to generally vary with the position of each point in our domain.

The source was built by a prism located along *x* between 95 and 105 m and along *z* between 5 and 10 m depth, with unitary magnetization. Inclination and declination of the main and induced fields are the same (Inc = 90°; Dec = 0°). The 2D domain along *x*, goes from 1 to 200 m with 1 m step size and along *z* from 1 to 41 m. In figure 5a is shown the field at 0 level.

The highest altitude was chosen according to the maximum depth that we want to investigate in the inversion process.

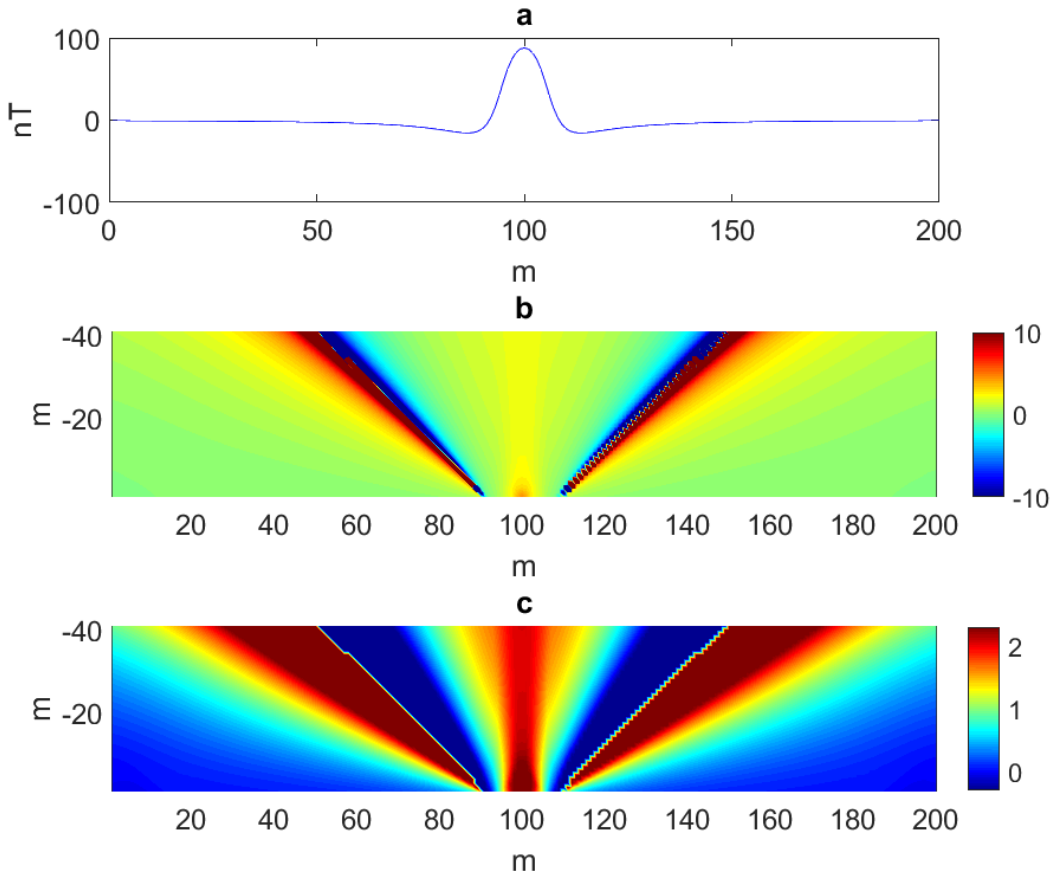

Figure 5: (a) Magnetic field due to a prismatic source. (b) $\beta(x,z)$ function estimated for the entire domain with instabilities due to numerical errors. (c) $\beta(x,z)$ function corrected by a 'brute force' approach considering a reasonable range of values from 0 to 2.1

Considering that in this case our field is not homogeneous, we can expect a not constant value of β within our domain.

As we expected, looking at figure 5b it is however plausible that the numerical process produces some instabilities. To reduce it, we used a 'brute force' approach on the estimates of β values, setting automatically those values outside a reasonable range to the limits of that range.

In particular, because we are considering a magnetic 2D field, we set this range from 0 to 2.1.

So, if the estimate of β at a position (x,z) is lower than 0.1, that β value is modified as 0; if the estimate of β in a position (x,z) is higher than 2.1, that β value is modified as 2.1.

We, then, performed the inversion using an inhomogeneous depth weighting function built with the estimated $\beta(x,z)$ function shown in figure 5c.

We ran two inversions for both approaches, homogeneous and inhomogeneous, with and without positivity constraint, meaning

that when we are using it, we are rejecting negative solutions of the model.

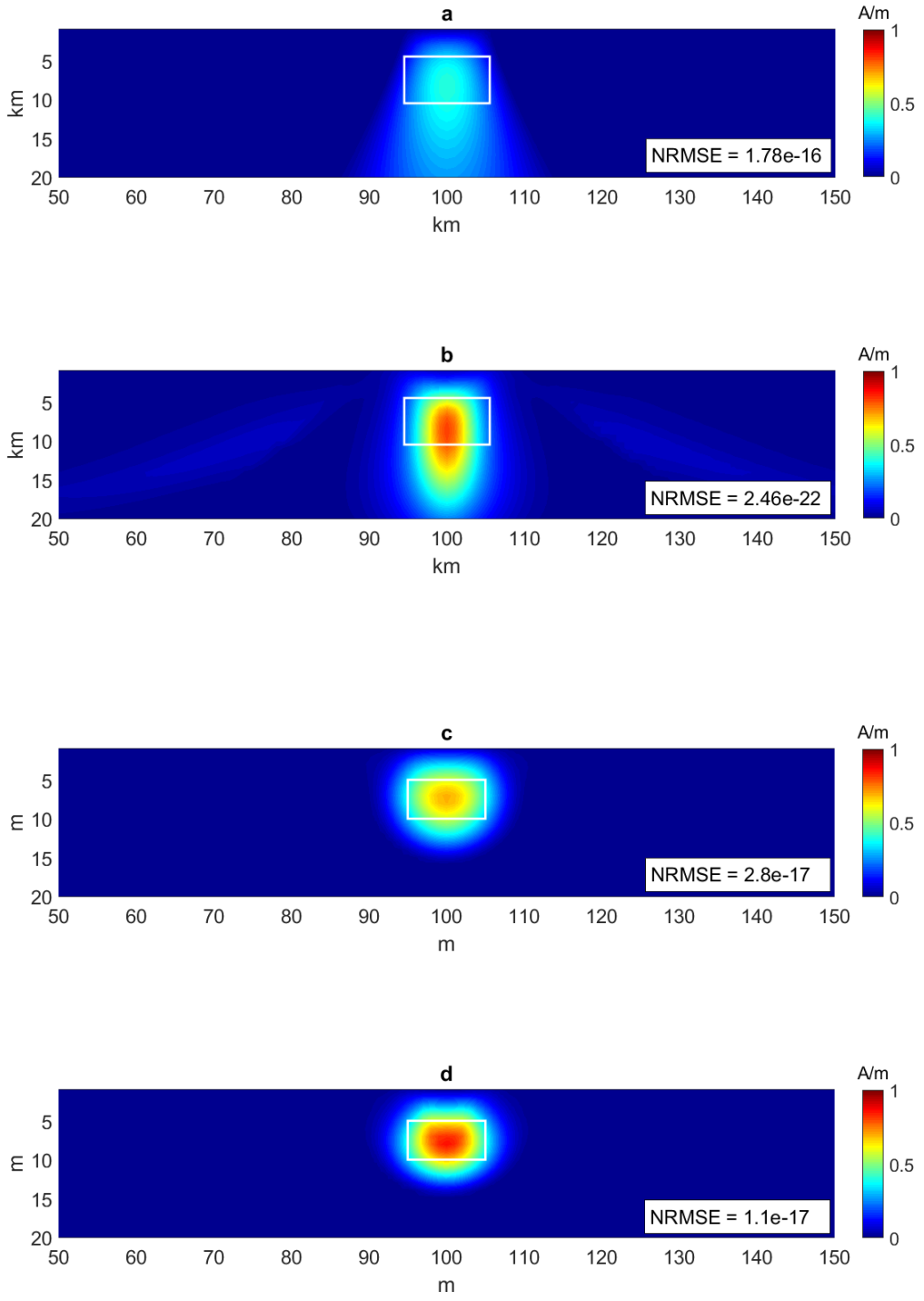

Figure 6: (a) Model obtained by using a homogeneous depth weighting function with β = 2. without positivity constraint(b) Model obtained by using an inhomogeneous depth weighting function (figure 4c) without positivity constraint (c) Model obtained by using a homogeneous depth weighting function with β = 2. with positivity constraint (d) Model obtained by using an inhomogeneous depth weighting function (figure 4c) with positivity constraint. White box highlights the true source limits.

Looking at the models obtained in figure 6a and figure 6b, with no positivity constraint and with an inhomogeneous depth weighting function, it is possible to recover a better information regards the magnetization distribution in depth, while the homogeneous approach is too smooth and the magnetization is highly underestimated.

Using positivity constraints, the main difference between the homogeneous (figure 6c) and the inhomogeneous (figure 6d) approach is that with a constant weighting exponent, the magnetization of the source is underestimated by a 31%, while in the other case it is underestimated by a 19% only.

Note also that, with our approach the NRMSE, with or without using positivity constraints, is lower.

The percentage is referred at the maximum value in the obtained model, so another advantage of using an inhomogeneous approach is that the model is representing better the whole source extent along *x* and *z*.

From now on, we will perform inversions with positivity, to compare the best homogeneous approach solution against our approach.

5.3. Two-body sources

The next step is to test the efficiency of the inhomogeneous approach in presence of two bodies.

The two prismatic sources are located along *x* between 55-65 m and 135-145 m, while along *z* between 5-15 m depth and between 10-20 m depth, with unitary magnetization both. Inclination and declination of the main and induced fields are the same (Inc = 90°; Dec = 0°) for both sources. The 2D domain along *x*, goes from 1 to 200 m with 1 m step size and along *z* from 1 to 41 m.

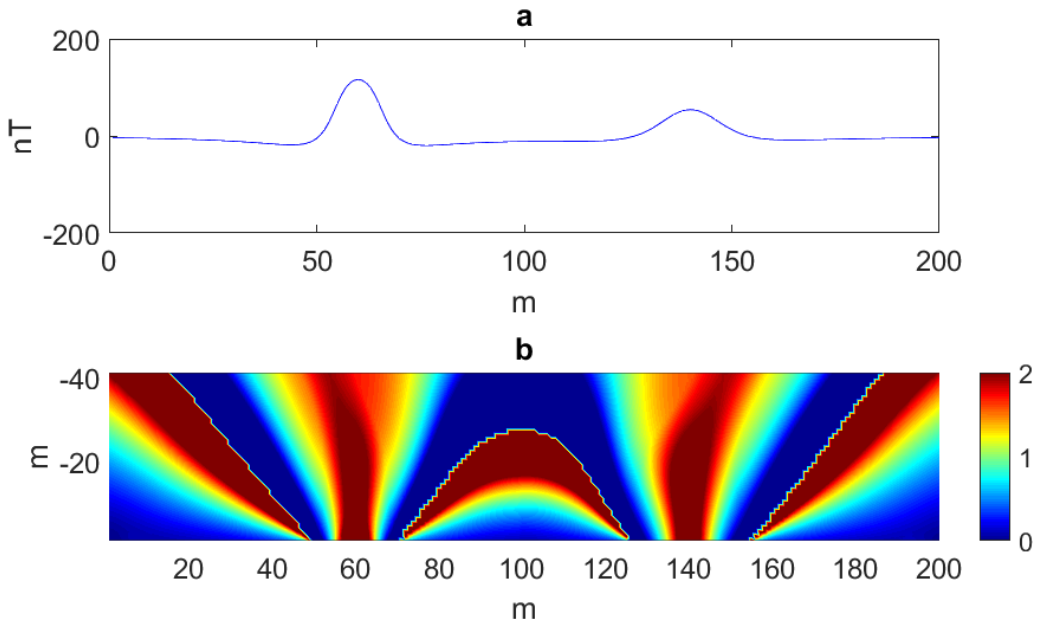

Figure 7: (a) Magnetic field due to two prismatic sources at different depth (see text for details). (b) β(x,z) function corrected by a 'brute force' approach considering a reasonable range of values from 0 to 2.1

Once again, the instabilities were treated with a brute force approach, so from the original estimates we can recover a $\beta(x,z)$ function with values within a range physically acceptable (figure 7b).

Considering the estimates due to one of the two sources, we can recover some similarities with the estimates in figure 5, while the difference in the central part is due to the interference between the two anomalies.

Positivity constrain is used to reject negative values of magnetization for both approaches.

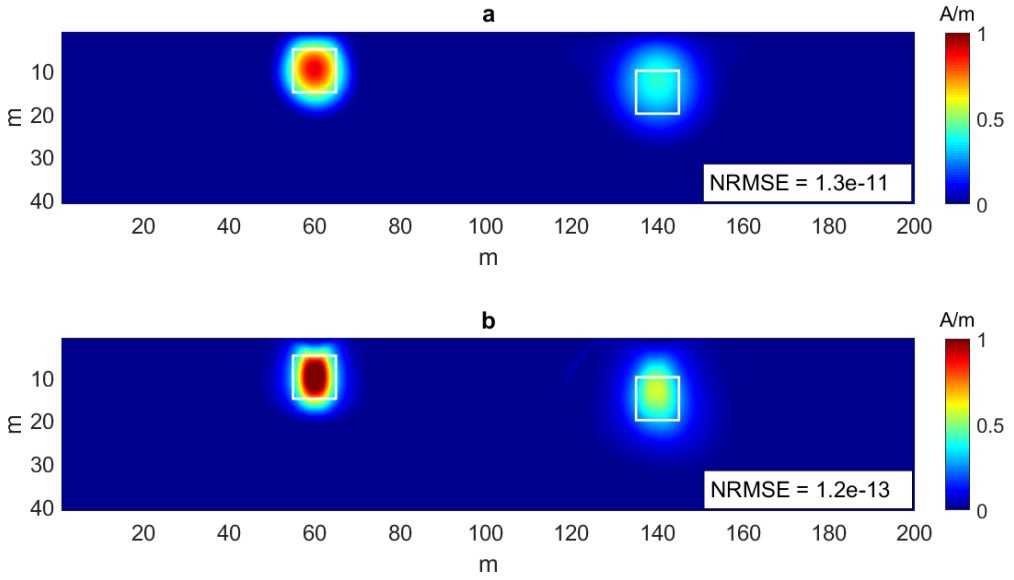

Figure 8: (a) Model obtained by using a homogeneous depth weighting function with β = 2. (b) Model obtained by using an inhomogeneous depth weighting function (figure 7b). White boxes highlight the true source limits.

The main difference between the homogeneous and the inhomogeneous approach is again linked to the under estimation of the magnetization of both sources.

Using a homogeneous depth weighting function with $\beta = 2$ (figure 8a) we confirm for the shallowest source the result of the previous case, in fact the magnetization is again underestimated by a 31%. However, the deepest source magnetization is underestimated by a 60%.

Instead, with our approach (figure 8b) both sources have a good position in depth and a magnetization close to the true value. The underestimation of the deepest source magnetization is reduced to 12%.

This case was also tested adding to the initial data a 5% random noise. This should affect also the estimation of beta values, especially because derivatives will enhance high frequencies.

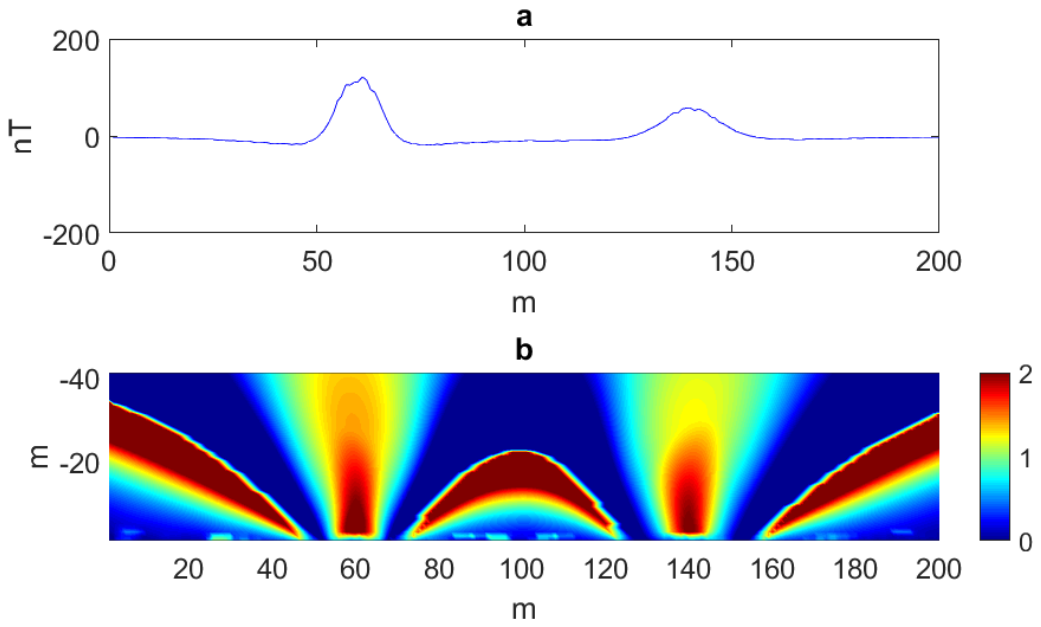

Figure 9: (a) Magnetic field due to two prismatic sources at different depth with a 5% random noise added (see text for details). (b) β(x,z) function corrected by a 'brute force' approach considering a reasonable range of values from 0 to 2.1

If we compare figure 9b and figure 7b is easy to spot some differences in the estimates of beta values, mainly at low altitudes, but the whole trend is pretty similar.

Positivity constraints are used to reject negative values of magnetization for both approaches.

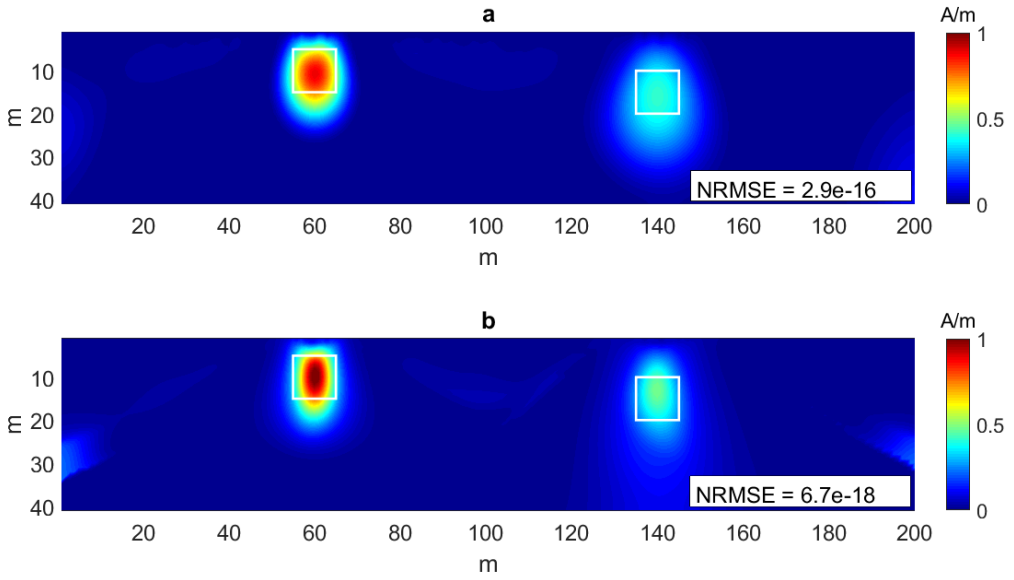

Figure 10: (a) Model obtained by using a homogeneous depth weighting function with β = 2. (b) Model obtained by using an inhomogeneous depth weighting function (figure 9b). White boxes highlight the true source limits.

However, the models obtained adding random noise to the original data are not so different from those in figure 8, and the main differences between the different approaches are still present. In fact, we recover a better estimate of the true magnetization value by the inhomogeneous approach, and the deepest source is more compact even if its magnetization is underestimated. By the way, if we compare the two solutions, using an inhomogeneous depth weighting function is helping to better recover the two body features.

We have seen here the case of two prism sources; we will see in the next section how different-homogeneity sources respond to the two different kinds of inversion.

6. 3D Inversion with inhomogeneous depth weighting function

In this section we will show the application of the same procedure that we used in 2D cases, to 3D synthetic cases, and then to 3D real data.

Obviously, the equations used to estimate the $\beta(x,y,z)$ function, are those expressed in the paragraph 4.1.

6.1. Polygonal source

A 3D polyhedral source (Tsoulis, 2012) was built and then we computed the first vertical derivative of its gravity field (Figure 11).

The maximum extent of the source is 20 km along x direction, 15 km along y direction and 10 km along z direction. Density contrast is 1 g/cm^3. We considered a source volume of 50 km by 50 km by 20 km, along x, y and z respectively, with cells sized 1 km^3. The dataset was formed computing the field on a 50 km by 50 km map, with a 1 km step size along both the horizontal directions. The data were then upward continued at altitudes from 1 km to 20 km, with 1 km step size.

Positivity was used in both inversion processes.

We then solved the system (45) and computed $\beta(x,y,z)$ and the inhomogeneous weighting function $w(x,y,z)$.

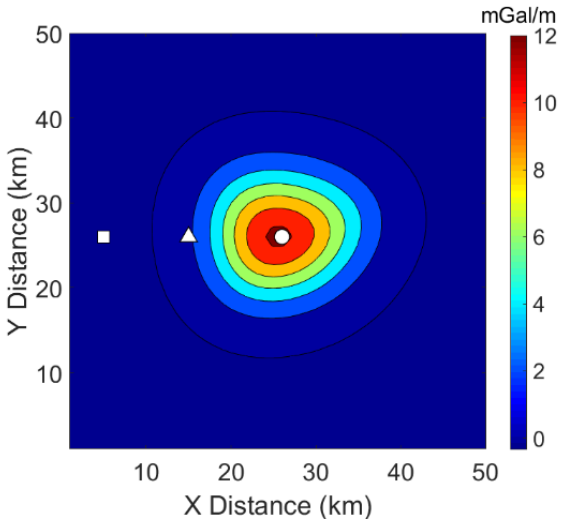

Figure 11: First vertical derivative of the gravity field of a polygonal body source along the zero-level plane. Square, triangle and circle symbols indicate the horizontal positions of the β estimates shown in Figure 12

To have an idea of the estimated values of β, we show in Figure 12 its values along vertical profiles corresponding to

the three positions described, by the same markers, in Figure 11.

We ran two inversion setups, by using a homogeneous and inhomogeneous depth weighting function, respectively.

Figures 13c and 13f show the model obtained by using a homogeneous depth weighting function, with $\beta = 3$, while figures 13b and 13e show the model obtained by using an inhomogeneous depth weighting function, with a variable exponent $\beta(x,y,z)$.

It is glaring, looking at the slices of both the models, that the inhomogeneous approach leads to a quite good definition of the body source, for either the top or the bottom, while the model obtained by using $\beta = 3$ produce a deeper source with a really bad definition of the bottom surface. Note that no other local constraints were used in the inversion process, except positivity.

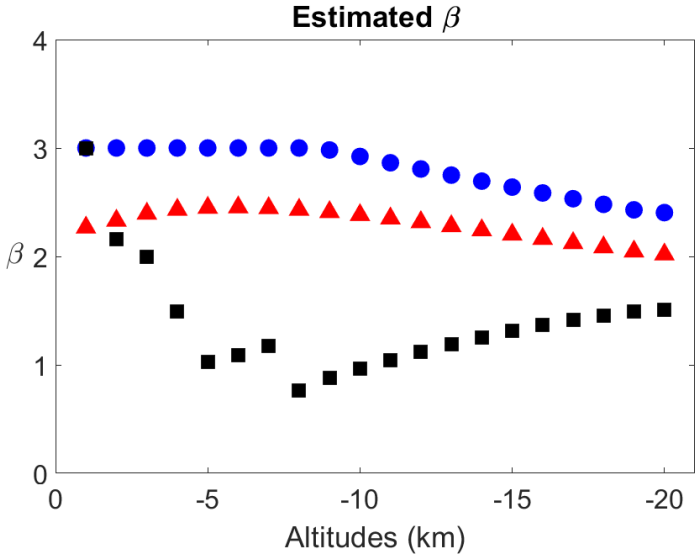

Figure 12: Estimated β values, using the scaling function method, along vertical profiles at the positions shown in Figure 11.

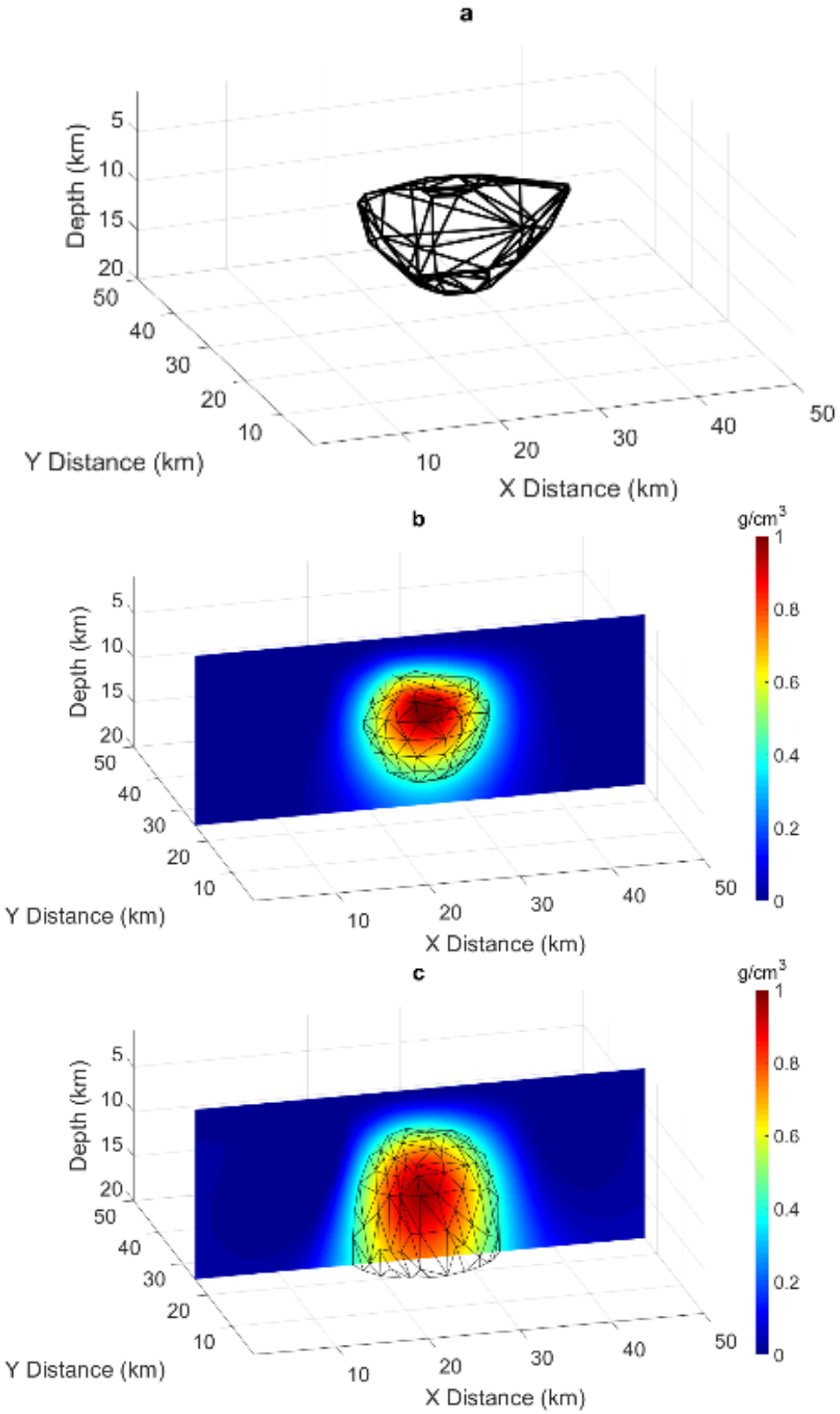

Figure 13.1: (a) W-E view of the true body (b) W-E slice of the model using an inhomogeneous depth weighting function β(x,y,z) and (c) using a homogeneous depth weighting function with β = 3.

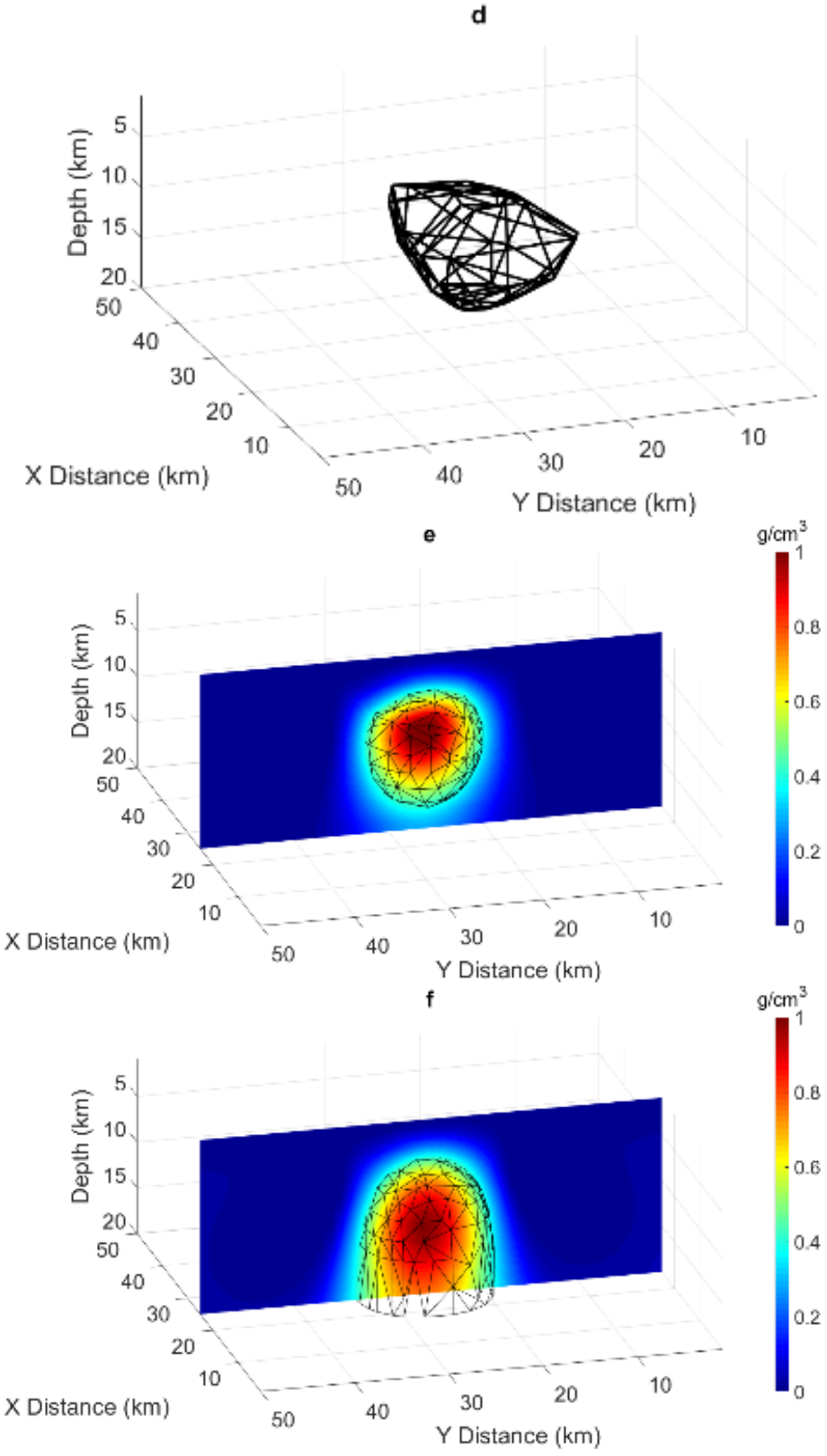

Figure 13.2: (d) N-S view of the true body (e) N-S slice of the model using an inhomogeneous depth weighting function β(x,y,z) and (f) using a homogeneous depth weighting function with β = 3.

Moreover, the density range of the inhomogeneous case is much better than that of the homogeneous inversion. Normalized RMSE are similar also in this case: $1.18*10^{-11}$ for the homogeneous approach and $5.02*10^{-10}$ for the inhomogeneous approach.

This case was also tested adding a 5% of random noise to the initial data (figure 14).

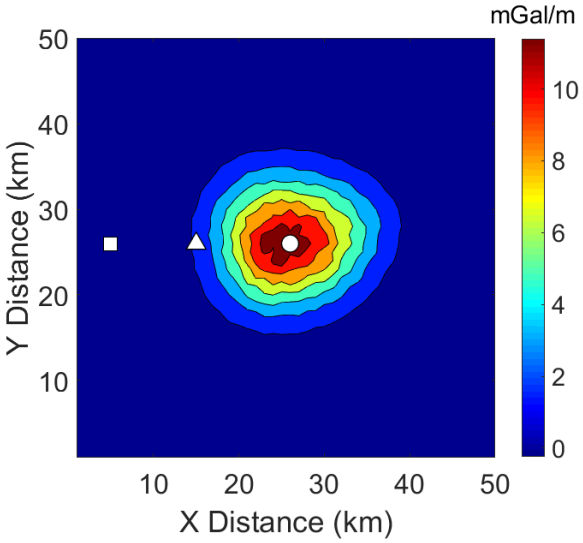

Figure 14: First vertical derivative of the gravity field of a polygonal body source along the zero-level plane. Square, triangle and circle symbols indicate the horizontal positions of the β estimates shown in Figure 15

As we expected, the presence of noise is not seriously affecting the estimates of beta (figure 14), because the upward continuation is acting like a low-pass filter, removing the effect of it, and even if the first one or two level of β are affected by this kind of noise, the estimates are almost the same as those presented in Figure 12.

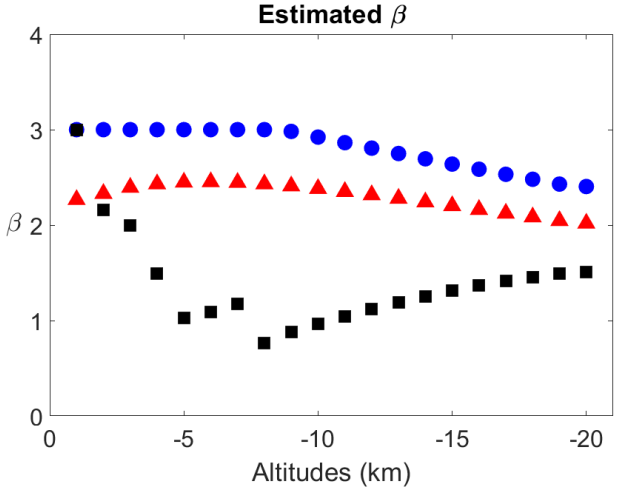

Figure 15: Estimated β values, using the scaling function method, along vertical profiles at the positions shown in Figure 14.

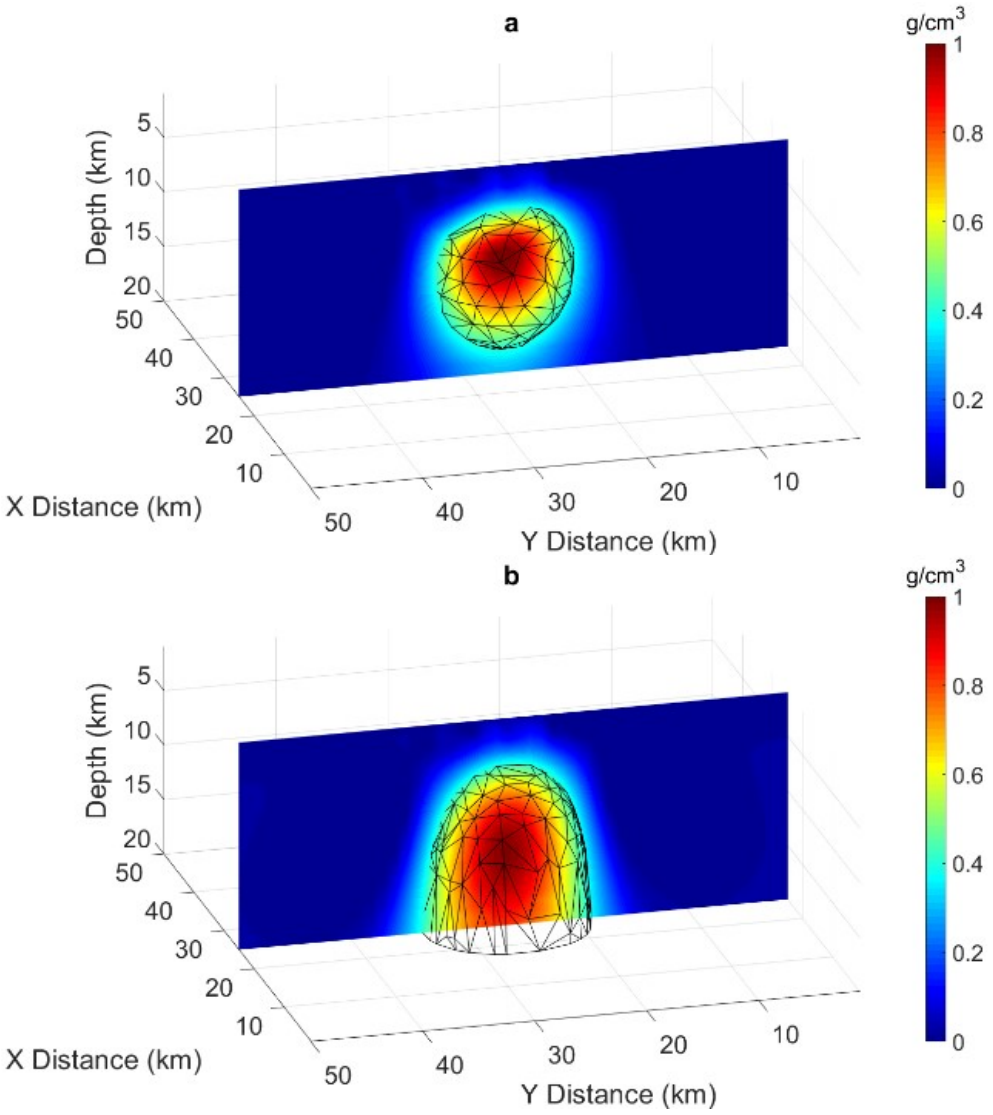

Figure 16.1: (a) N-S slice of the model using an inhomogeneous depth weighting function with β(x,y,z) and (b) using a homogeneous depth weighting function with β = 3.

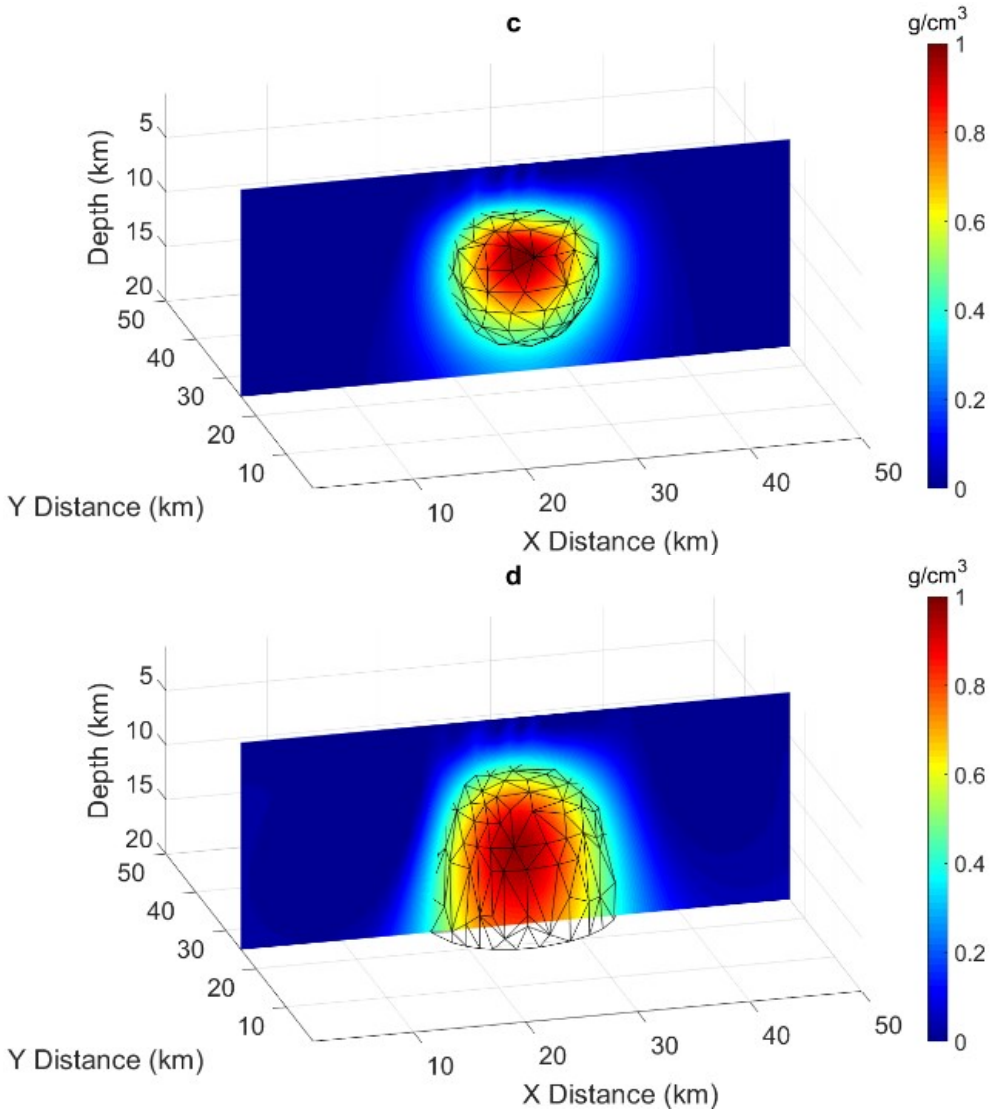

Figure 16.2: W-E slices of the model using (c) an inhomogeneous depth weighting function with β(x,y,z) and (d) homogeneous depth weighting function with β = 3.

The source-models obtained adding random noise to the original data (figure 16) are not so different from those in figure 13, and the main differences between the different approaches are still present.

Again, the inhomogeneous approach recovers better both the true density value and the geometry of the body.

Normalized RMSE are similar also in this case: $7.73*10^{-11}$ for the homogeneous approach and $5.02*10^{-11}$ for the inhomogeneous approach.

6.2. Two buried bodies: a prismatic source and a source like a vertical intrusion

The last synthetic 3D case that we discuss in this thesis is that of two sources: one prismatic body and the other one like

a vertical intrusion. This choice was made because, considering table 1, we expect different values of beta for the two sources.

The two prismatic sources are located along *x* between 11-14 km and 36-39 km, while along *y* between 24-26 km and along *z* between 4-6 km and 3-20 km depth. The magnetization is 1 A/m and inclination and declination of the main and induced fields are the same (Inc = 90°; Dec = 0°) for both sources. The 3D domain along *x* and *y*, goes from 1 to 50 km with 1 km step size and along *z* from 1 to 10 km. Figure 17 shown the observed field due to the two sources.

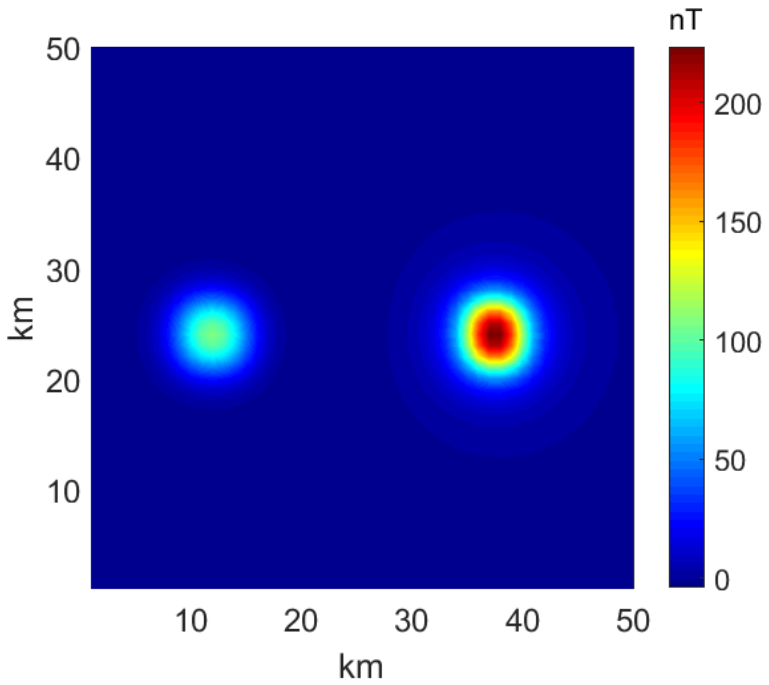

Figure 17: Magnetic field due to a prismatic source and a source like a vertical intrusion along the zero-level plane.

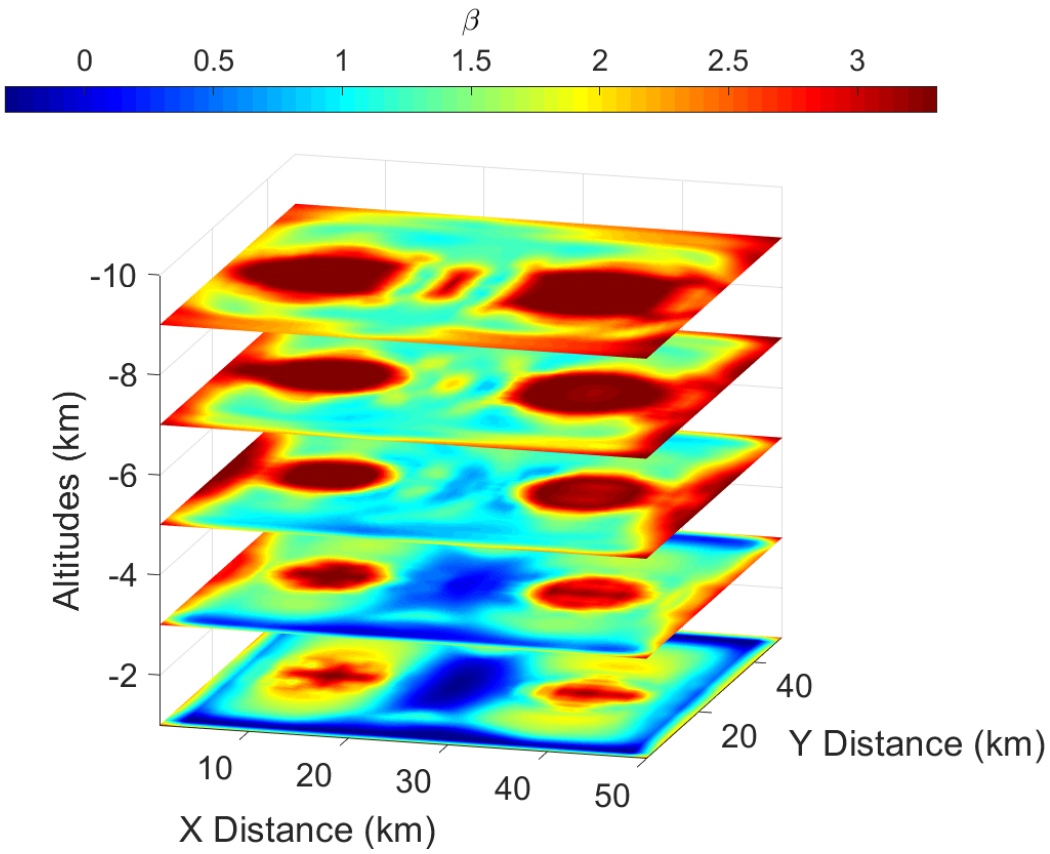

Figure 18: Slices at several altitudes of the β(x,y,z) function estimated for the entire domain.

In figure 18 we show the estimates of β at several altitudes. The β estimates in the area between the sources are not so strongly different. However, we have to consider that the intrusion-like source is finite in depth. Moreover, looking at figure 18 it is glaring that some information regarding the difference between the two sources is still present.

Positivity constraints are used to reject negative values of magnetization for both approaches.

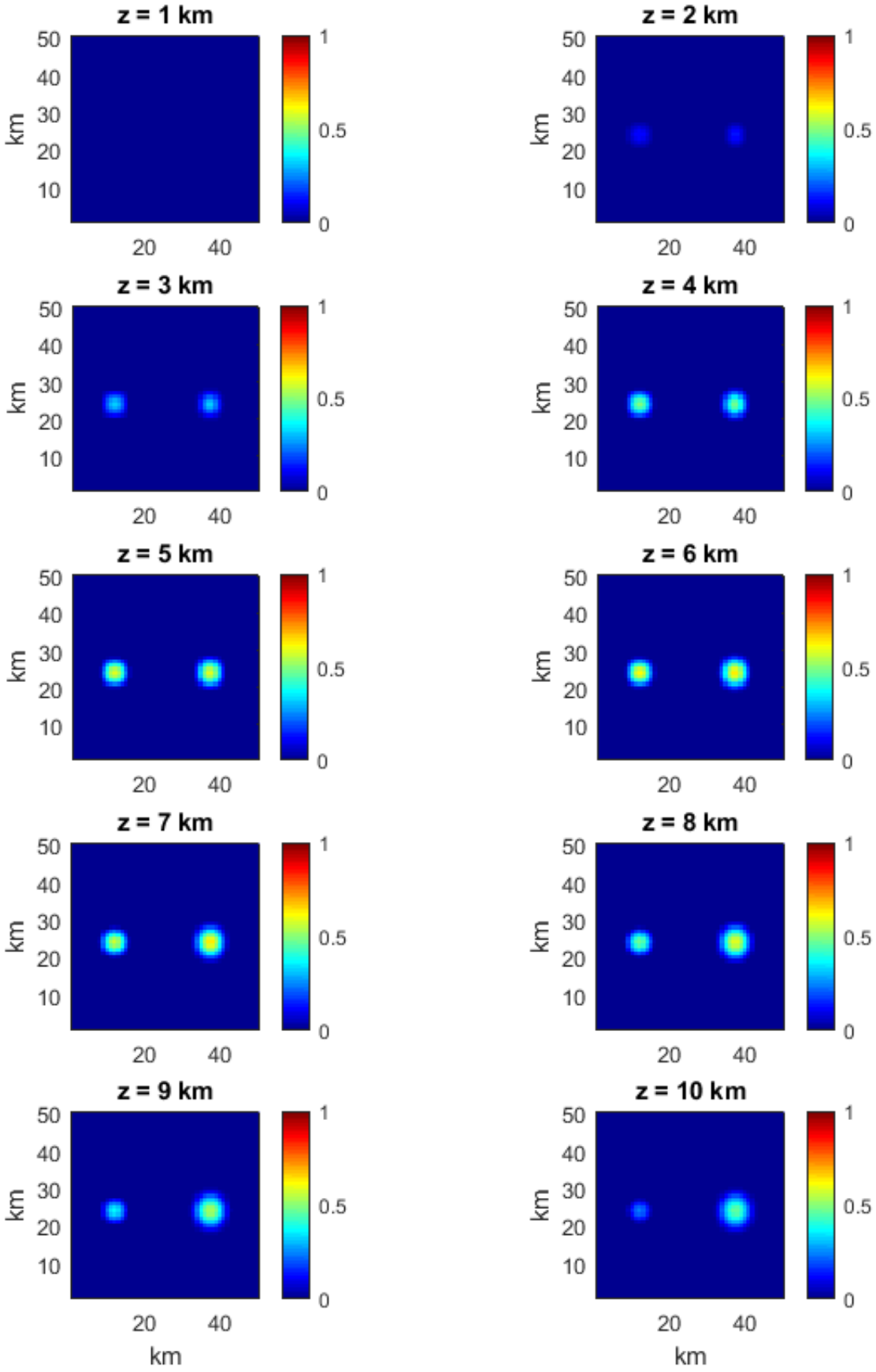

Figure 19: Slices of the model obtained by using a homogeneous depth weighting function with β = 3.

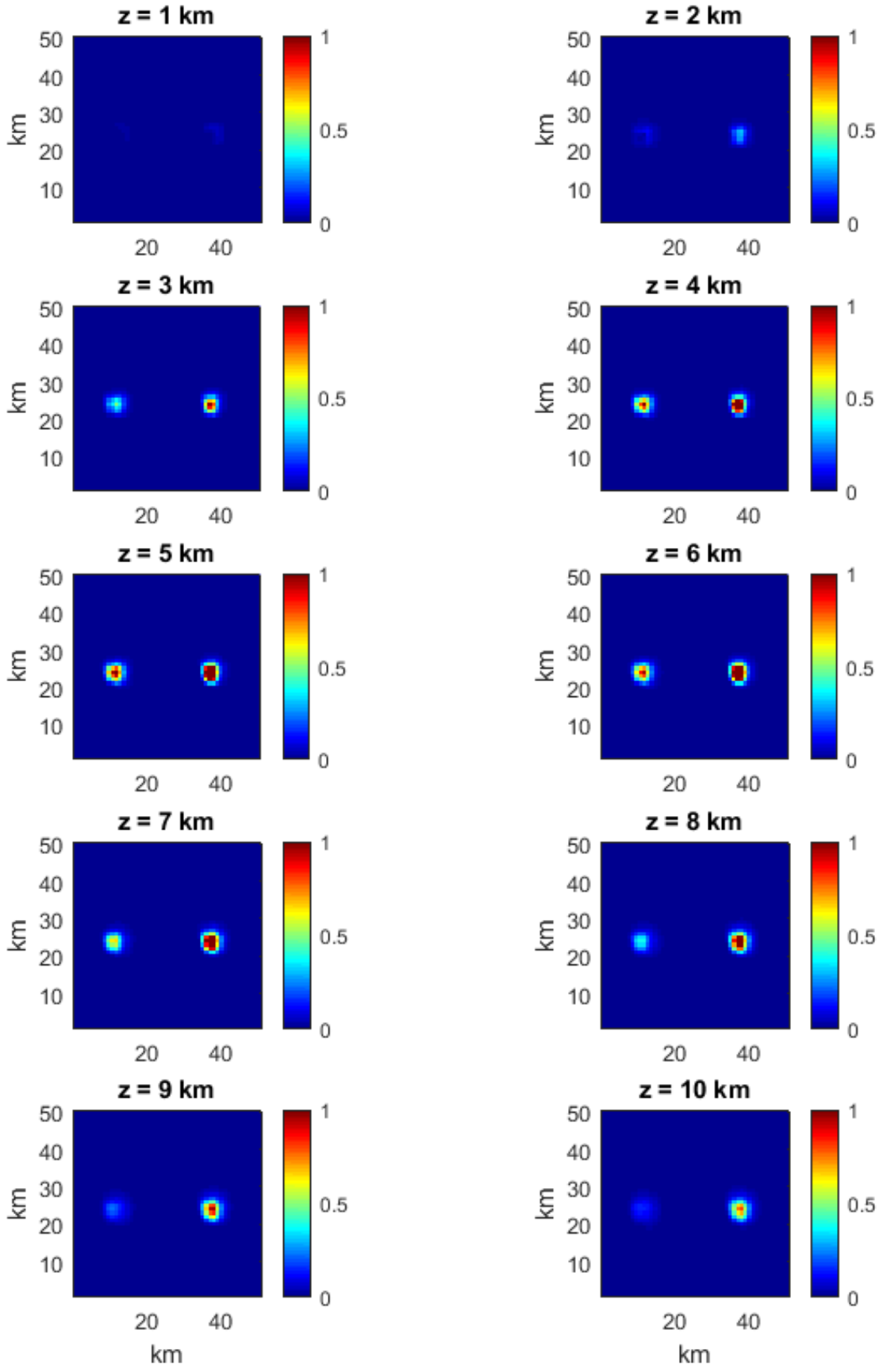

Figure 20: Slices of the model obtained by using an inhomogeneous depth weighting function (figure 18).

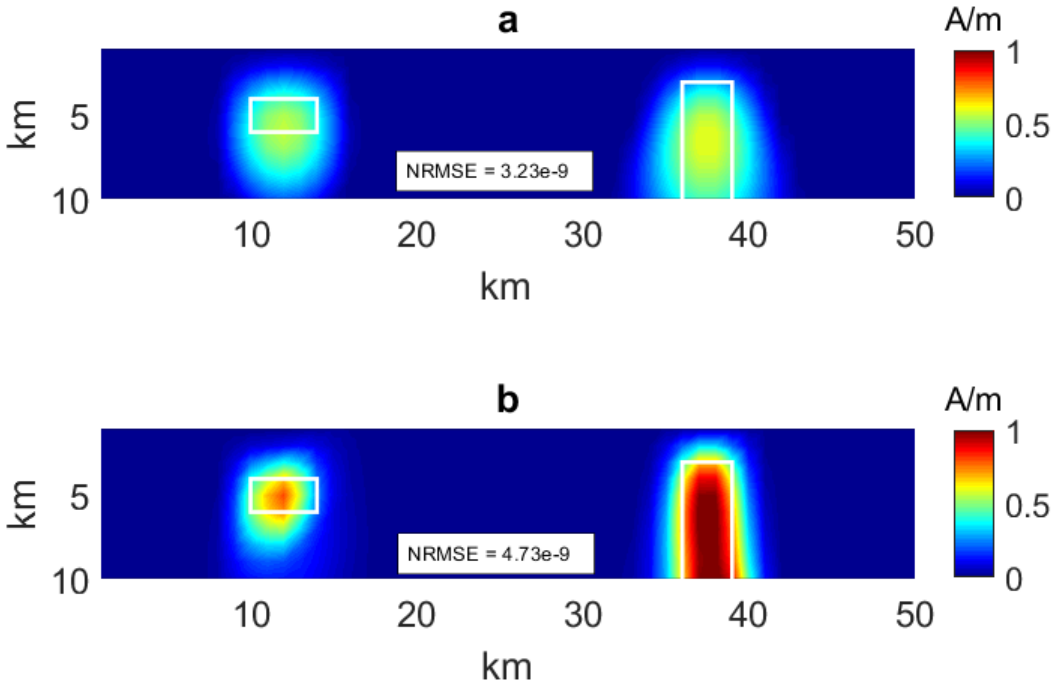

Figure 21: (a) Central section of the model using a homogeneous depth weighting function. (b) Central section of the model using an inhomogeneous depth weighting function. White boxes highlight the true source limits.

Figures 19, 20 and 21 clearly show that the results obtained by using the inhomogeneous approach are once more significantly improved. Comparing the two sections in figure 21, it is easy to understand that the main advantage in using an inhomogeneous depth weighting function is to obtain more concentrated magnetization distributions with values poorly underestimated. Moreover, the inhomogeneous approach leads to a better definition of both sources' shapes. The center of the prismatic source is very well recovered compared to the homogeneous approach, and the source like the vertical intrusion is more compact an elongated in depth, while in the other case it seems more like a thicker finite body.

Considering the results obtained by 2D and 3D cases, we can confirm that the inhomogeneous approach could give better information about the distribution of the sources parameters in the inversion of potential fields.

6.3. Real case: Vredefort impact site

The Vredefort structure is located within the Witwatersrand basin, South Africa. Boon & Albritton (1937) were the first to suggest an impact origin. In the early 1960s, Dietz (1961) and

Hargraves (1961) cited the occurrence of shatter cones at Vredefort as evidence of an impact origin. After nearly a century of debate, the ca. 80-km wide Vredefort Dome is now widely accepted as the central uplift of a much larger impact structure (**Gibson and Reimold, 2001**).

Kamo et al. (1996) dated the impact event at 2.023±0.004 Ga based on the estimated age of pseudotachylite in the core region.

The original diameter of this impact structure was in excess of 250 km (**Reimold and Gibson, 1996; Gibson and Reimold, 2000, 2001**) and the Vredefort crater is one of the largest and oldest impact structures on Earth.

Reimold and Gibson (1996) reported a synthesis of the geologic knowledge about the Vredefort dome. Following these authors, the near circular Vredefort Dome, 70 km in diameter, located about 120 km to the southwest of Johannesburg, consists of Archaean granitoids in a 40-km-wide central core and of metasediments and metavolcanics in an outer collar belonging to the 2.9-2.72 Ga Witwatersrand, the ca. 2.7 Ga Ventersdorp, and 2.5-2.25 Ga Transvaal Supergroups (Fig. 21). Locally, along the outer margin of the Witwatersrand Basin, felsic metasediments occur and mafic metavolcanics of the 3.074 Ga Dominion Group and 3.1-2.8 Ga basement granitoids. The crystalline core of the dome consists of an outer annulus of heterogeneous amphibolite-facies migmatites of the Outer Granite Gneiss (OGG) around the central Inlandsee Leucogranofels (ILG). The southeastern part of the Vredefort Dome is covered by Karoo (250-180 Ma) sediments and dolerites (**Reimold and Gibson, 1996**).

In 1990, McCarthy et al. mapped the presence of series of anticlines and synclines from the center to a radial distance of 150 km, arranged as concentric rings and clearly related to the formation of the Vredefort impact structure.

Dikes of the so-called Vredefort granophyre occur both in the central core and distal collar areas. In the core area, the dikes are radial with respect to the structure and are up to 20 m wide and 4–5 km long. In the collar, the dikes are concentric with respect to the structure and can be > 50 m wide and about 10 km long (**Grieve and Therriault, 2000**).

An integrated geophysical model of the Vredefort structure, based on refraction and reflection seismic, gravity, magnetic, and petrophysical data, was published by Henkel and Reimold (1996, 1998). This model demonstrated that the central uplift of this large impact structure, the Vredefort Dome, is deeply eroded, about 80 km wide, and still represents a structural uplift of about 12 km, at the present erosion level. This structural uplift is best illustrated by the rise of the lower parts of the upper crust (layers 3 and 4, Fig. 22).

The total uplift may originally have amounted to as much as 20 km (**Henkel and Reimold, 1998**).

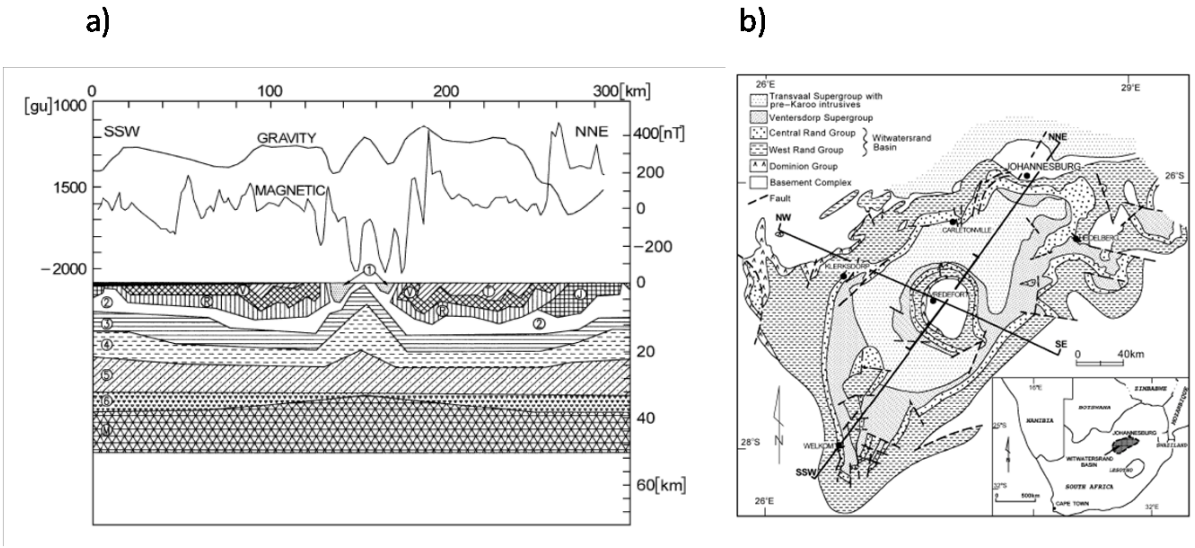

*Figure 22: (a) Geophysical model of the SSW–NNE section (see Figure 22b) through the Vredefort impact structure (from **Henkel and Reimold, 1996, 1998**).*

Hart et al. (1995) analyze the magnetic anomaly of the Vredefort area and claim that the data in the Vredefort basement are consistent with impact-related thermal remanent magnetization.

The aeromagnetic data over the structure (**Corner et al., 1990**) show strong, well-defined concentric patterns. In the outer rim, the pattern reflects the different sedimentary strata. About halfway between the outer collar structures and the central uplift there is a prominent negative magnetic anomaly that extends in a broad semi-circular belt; 2 to 4 km wide around most of the basement core. This anomaly is attributed to the contact of the ILG and OGG, the so-called Vredefort discontinuity (Hart et al., 1990).

Beiki and Pedersen (2010) analyzed the *Tzz* component of the GGT data of the Vredefort dome area using an eigenvector analysis to estimate the depth and a dimensionality (I) parameter of the source. The dimensionality is a parameter that lies between zero and unity for any potential field (**Beiki and Pedersen, 2010**). If the causative body is strictly 2D, then I is equal to zero and approaches unity when the causative body is 3D-like. Using this method, the authors show that quasi 2D geologic bodies are dominant specially in the outer rim, with depth to sources between 1000-1500 m or more than 1500, but in the central part of the dome the dimensionality approaches unity and the depth exceeds 1500 m. (Fig. 23).

Wilson et al., (2011) developed massively parallel software for inversion of gravity and gravity gradiometry data. They inverted simultaneously all components of GGT and used a very large number of cubic cells of just 25m side. These authors extended their model only to 2400 m depth and obtained results very similar to Beiki and Pedersen (2010).

Martinez and Li (2011) inverted the single component *Tzz* of the gravity gradient tensor (GGT) and performed a joint inversion of three components of the GGT tensor data: the two observed component (*Tuv* and *Txy*) and the calculated component *Tzz*.
They showed that the joint inversion of these three components improves the model resolution, providing a more focused central high-density structure. Their model shows the presence of dense rocks corresponding the central uplift at a depth of about 6000 m depth and also corresponding to the gravity highs in the outer collar at depths of about 2000 m.
Ialongo (2014) inverted the single component *Tzz* of the gravity gradient tensor (GGT) with two different setups, estimating before the homogeneity degrees for the main core of the impact site and for the distal ring structure, respectively. Then two homogeneous inversions were made using in turn such estimated homogeneity degrees.
His model shows the maximum depth for the distal ring structure, running an inversion with a depth weighting exponent of 1.4, around 10 km, while the maximum depth for the distal ring structure, running an inversion with a depth weighting exponent of 3, was around 16 km.

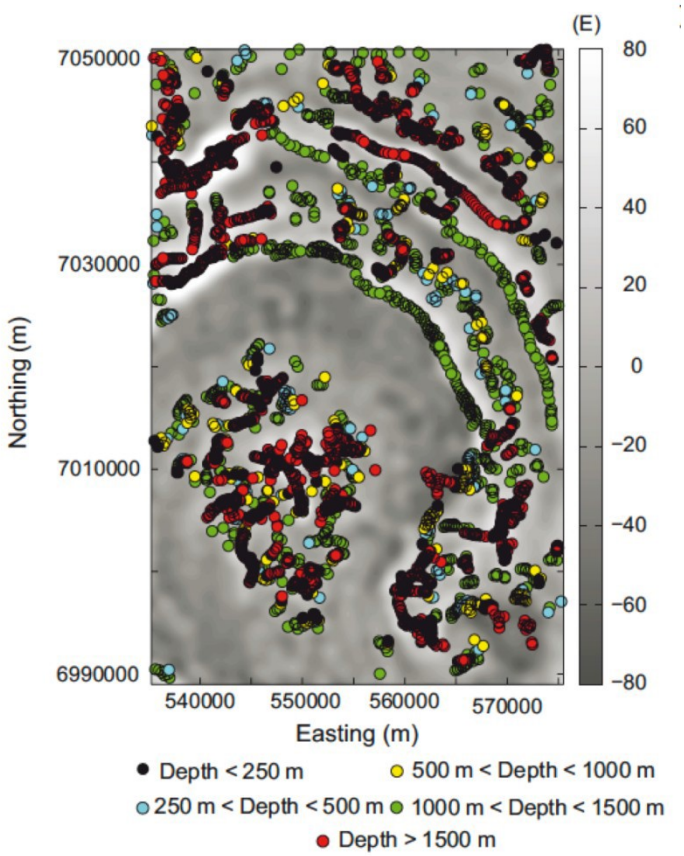

Figure 23 Location and depth to the center of mass of gravity sources as estimated by Beiki and Pedersen (2010)

According to our method the first step is building the inhomogeneous depth weighting function. We decided to estimated *n* from the vertical gradient of the field (figure 24b) instead than from the gravity field (figure 24a), in order to reduce the regional field effect.

The model volume reaches 20 km in depth, while along *x* and *y* its extension is respectively 41 by 63 km.

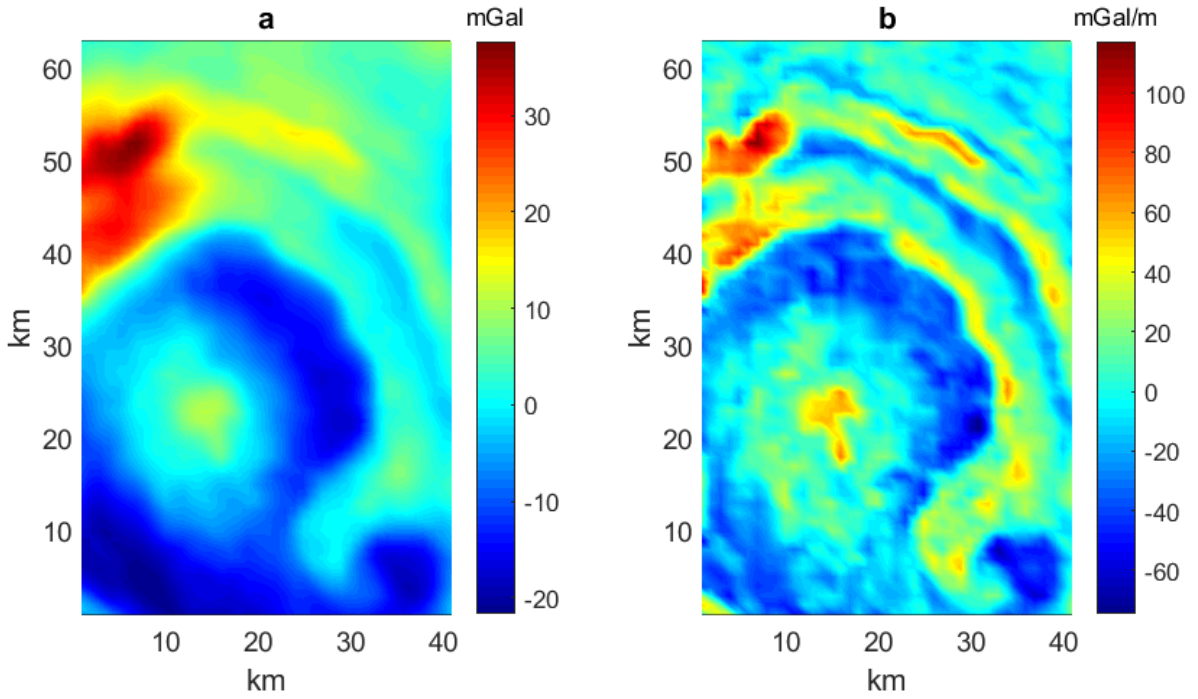

Figure 24 (a) Gravity map and (b) Tzz component of the Vredefort impact site area.

Estimates of β presents instabilities that are treated like the synthetic cases discussed before, considering a reasonable range between 0 and 3.1. These instabilities are probably due to the presence of several sources that, at higher altitudes, are interfering generating numerical singularities and on being some anomalies of the analyzed map truncated laterally.

However, looking at figure 25, we can see that at low and middle altitudes the β linked to the distal ring structure is lower than 2, while the values related to the core is higher, so confirming the results obtained by Ialongo (2014). At higher altitudes, the trend of β is however smoother. This difference is probably due to lack of resolution at higher altitudes, because the low frequency effects are the dominant contributes.

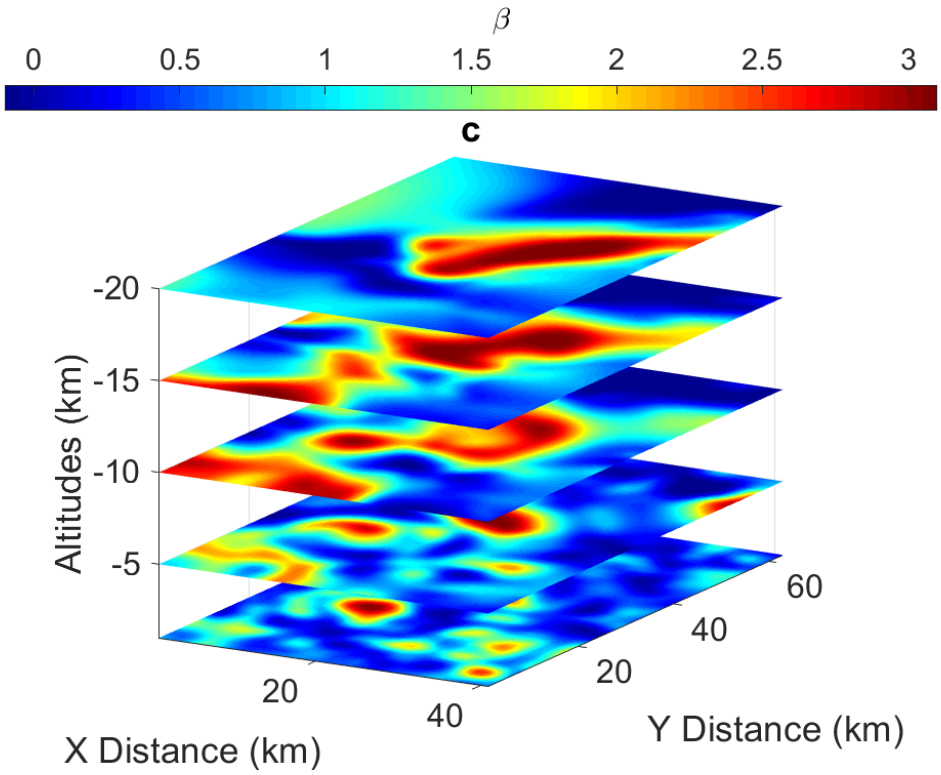

Figure 25: Slices of the β(x,y,z) function estimated for the entire domain at 1, 5, 10, 15 and 20 km.

However, the trend at low and middle altitudes of the estimated β related to the main structures is fitting the expectations because the results relate to two main structures, which are geometrically different: the core is like a spheroid body ($\beta \approx 3$) and the distal rings are like horizontal pipes or dykes ($1 < \beta < 2$).

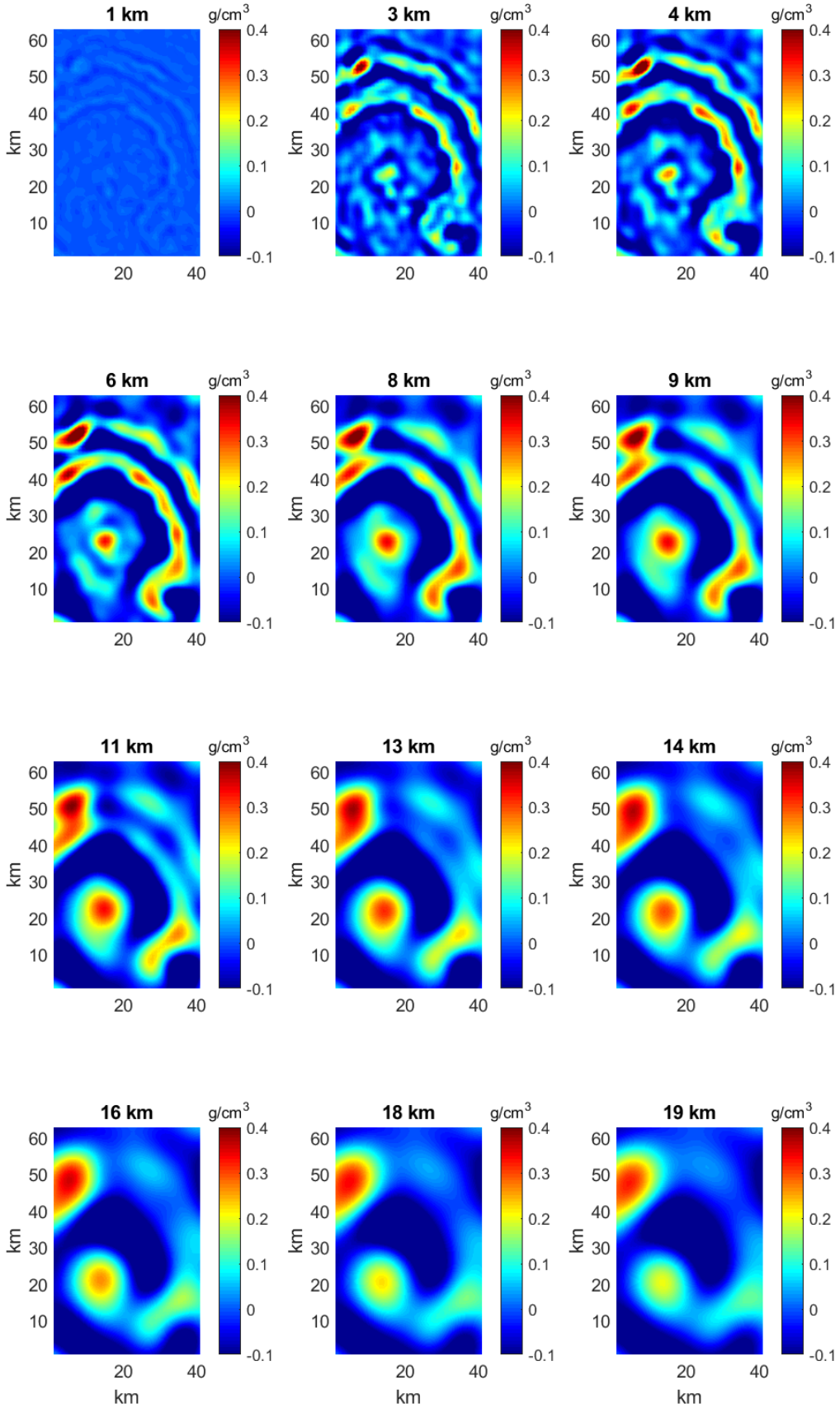

Figure 16: Density-model obtained by using a homogeneous depth weighting function ($\beta = 3$).

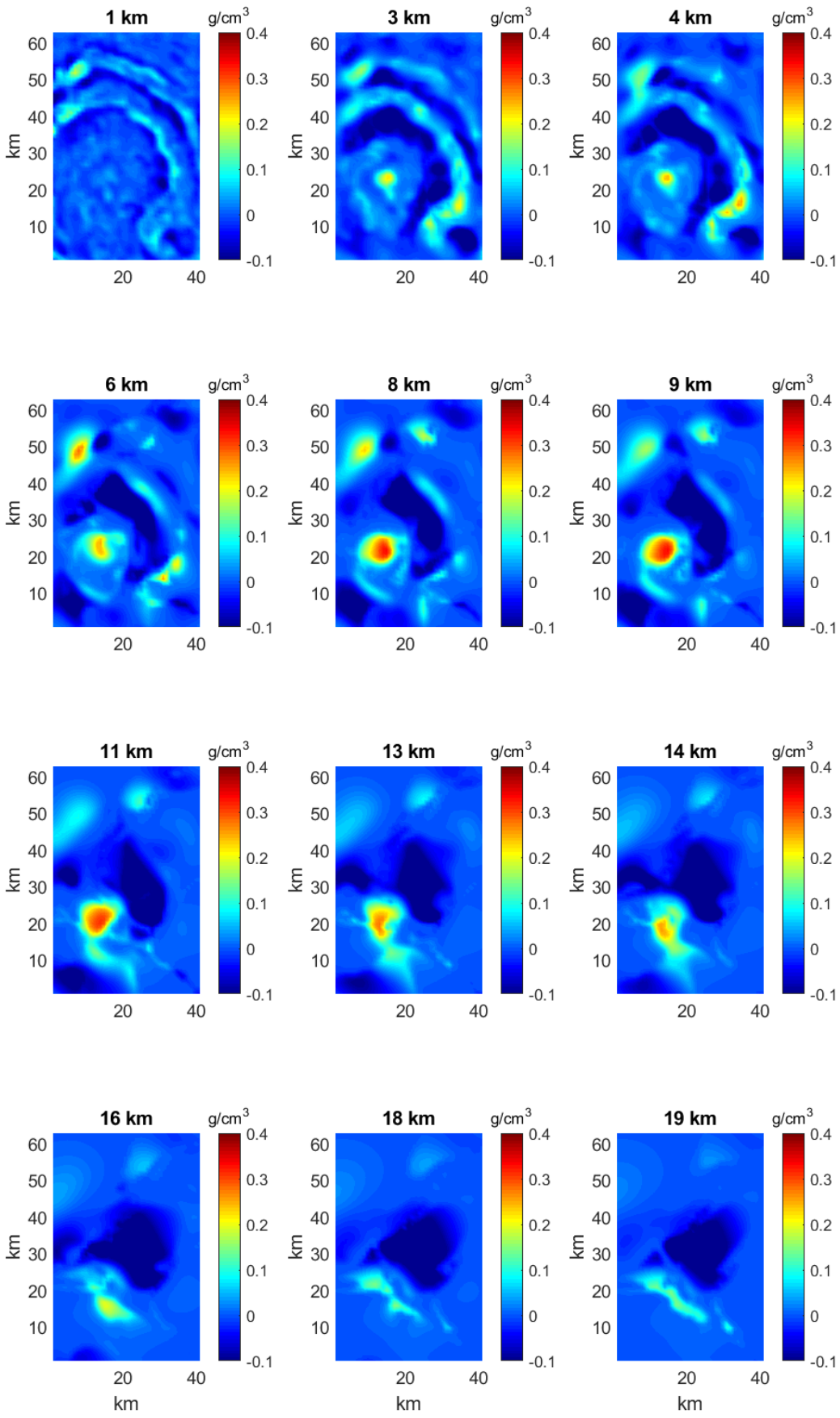

Figure 27: Density-model obtained by using an inhomogeneous depth weighting function (figure 25)

With a homogeneous depth weighting function (figure 26) we recover a smooth solution and both the main sources, the main core and the rings of the impact, are still visible at the bottom of the model (20 km). This is not in agreement with the result by Henkel and Reimold (1996, 1998), which, based on gravity and magnetic inversion supported by seismic data, proposed a model where the bottom of the rings is around 10 km and the density contrast effect due to the core structure loses its effectiveness around 15 km.

Instead, using an inhomogeneous depth weighting function (figure 27) we can retrieve information regarding the position at depth of both core and distal ring structures that better fits the above model. In fact, the bottom of the distal ring structure, that should be around 10 km according to Henkel and Reimold (1996, 1998), is recovered very well using an inhomogeneous depth weighting function, while in the homogeneous case we saw that the interpreted structure was still visible at large depths.

In addition, also the core structure is shallower compared to the homogeneous approach and seems more reliable if we compare it with the model of Henkel and Reimold (1996, 1998).

Note that the NRMSE are pretty similar in both cases (that are $1.6*10^{-3}$ for the homogeneous case and $1.9*10^{-3}$ for the inhomogeneous case).

If we compare our results with those obtained by Ialongo (2013) we note that the position at depth of both core and distal ring structures are in agreement. But we must note that this the main structures have different structural indexes N (as we said before,3 for the core and between 1 and 2 for the distal rings), so it is not possible to have good estimations of both sources running a single inversion with a constant depth weighting exponent only. For this reason, Ialongo (2013) ran two separated inversion with two estimated N, to joint interpret the solutions for each source.

Instead, the inhomogeneous approach presented in this paper leads naturally us to a better solution because it takes into account during the same inversion process of the inhomogeneous nature of the structural index within the entire domain.

6.4. Real case: Mt. Vulture (Southern Italy)

The magnetic field of the volcanic district of Mt. Vulture (Southern Italy) is mainly characterized by two dipolar anomalies, one of shorter wavelength, possibly related to the edifice Mt. Vulture, and the other of greater extent, which should originate by a deeper source distribution. The field was

already analyzed by Cella and Fedi (2012) using first a homogeneous approach, with $\beta = 3$. But the resulting model was not able to account for the two sources and resulted in a non-realistic and too deep source model, concentrating, by the way, the magnetization not on the volcanic edifice but at a greater depth. Then they improved the quality of the solution by using $\beta = 0.25$ for the shallowest source and $\beta = 2$ for the deepest one. In practice, their final source-model was estimated by analyzing two filtered maps, using a method based on the discrete wavelet transform to separate the field in two main components at respectively a small-scale and a large-scale. So, the depth weighting exponent was not varying in the whole volume but assumed constant specific values in two different regions of the source volume.

It is clear that the interpretation of the data in this area is an intriguing task, because the shallowest source (the high amplitude anomaly about 140 nT, in correspondence of the Mt. Vulture volcano), and the deepest source anomaly are strongly overlapping one each other (Figure 28b).

The aeromagnetic dataset sized 74 km by 74 km (Figure 28b), with a step size along both the horizontal directions of 2 km and an acquisition elevation of 2.5 km a.s.l. Inclination and declination of both inducing field and total magnetization were estimated by Cella and Fedi (2012) as equal respectively to 57° and 15°.

The model volume dimensions are 76 km by 76 km by 30 km, with a step size of 1 km along x and y directions and 1 km along z direction.

As we did before, we performed two inversions, using a homogeneous depth weighting function with $\beta = 3$ and then using an inhomogeneous depth weighting with β values estimated from the field.

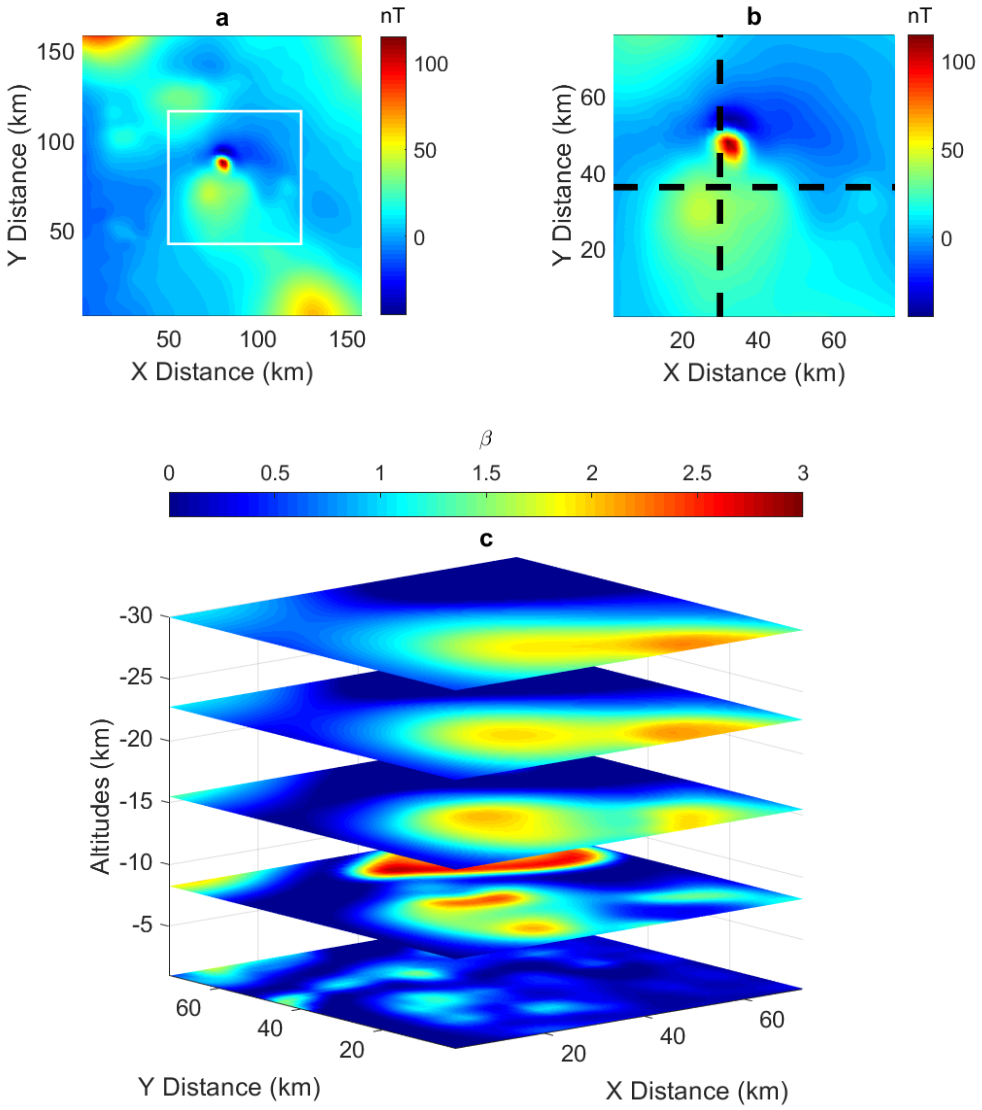

Figure 28: (a) Aeromagnetic map of the Mt. Vulture area. A white box outlines the analyzed area, whose data are shown also in (b). (c) Slices of β at 1, 8, 15, 22 and 30 km height, estimated using the scaling function method.

We show in Figure 30c the estimated β at several altitudes from 1 km to 30 km. We used downward continuation to level the dataset at the maximum high of the topography (around 1400 a.s.l.) and then upward continued it from that level to form the system (45).

Positivity constraints are used to reject negative values of magnetization for both approaches.

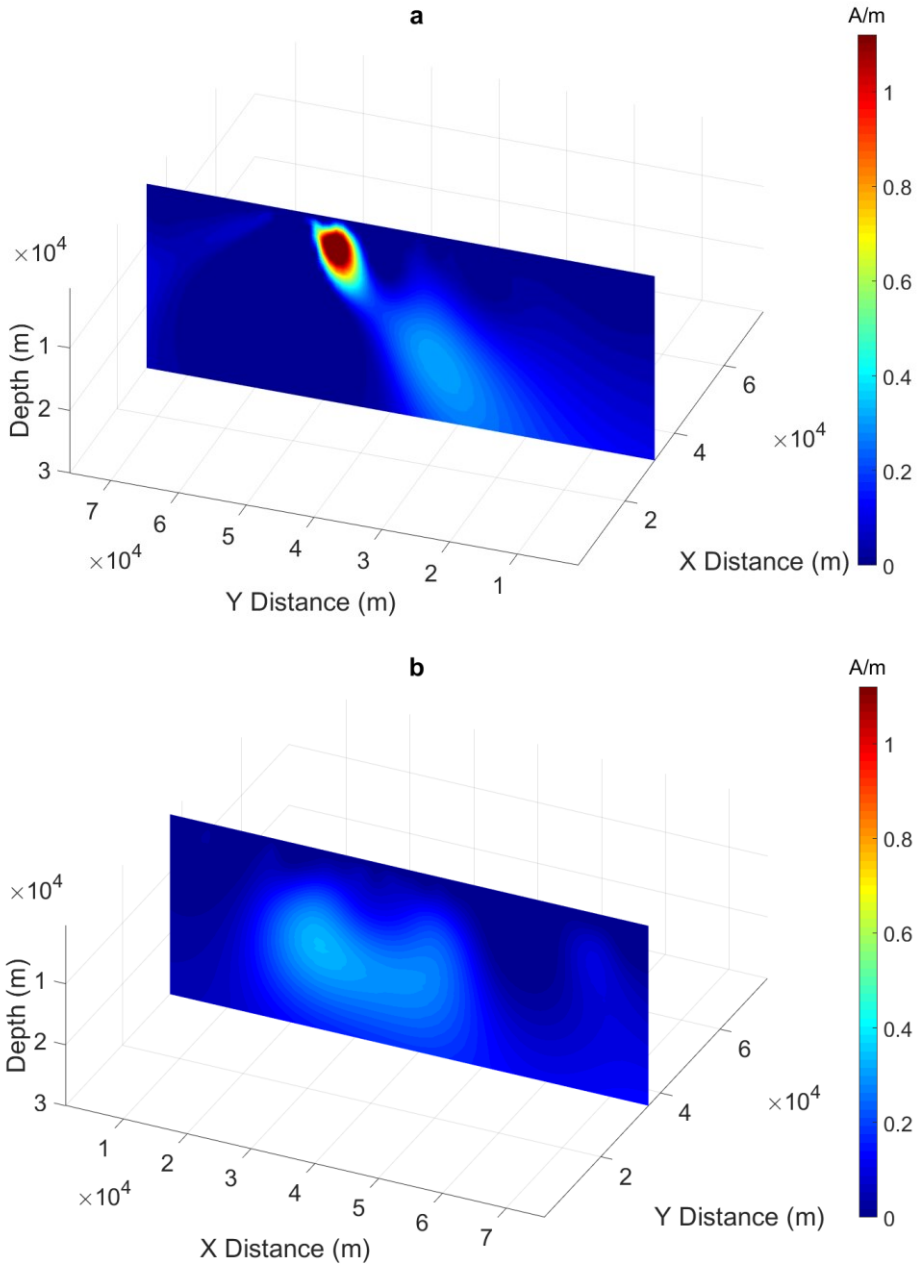

Figure 29.1: Model obtained (a and b) by using a homogeneous depth weighting function with β = 3, and (c and d) by using an inhomogeneous depth weighting function, with β(x,y,z) as shown in Figure 28c. The slices are referred to the black dashed lines in Figure 28b

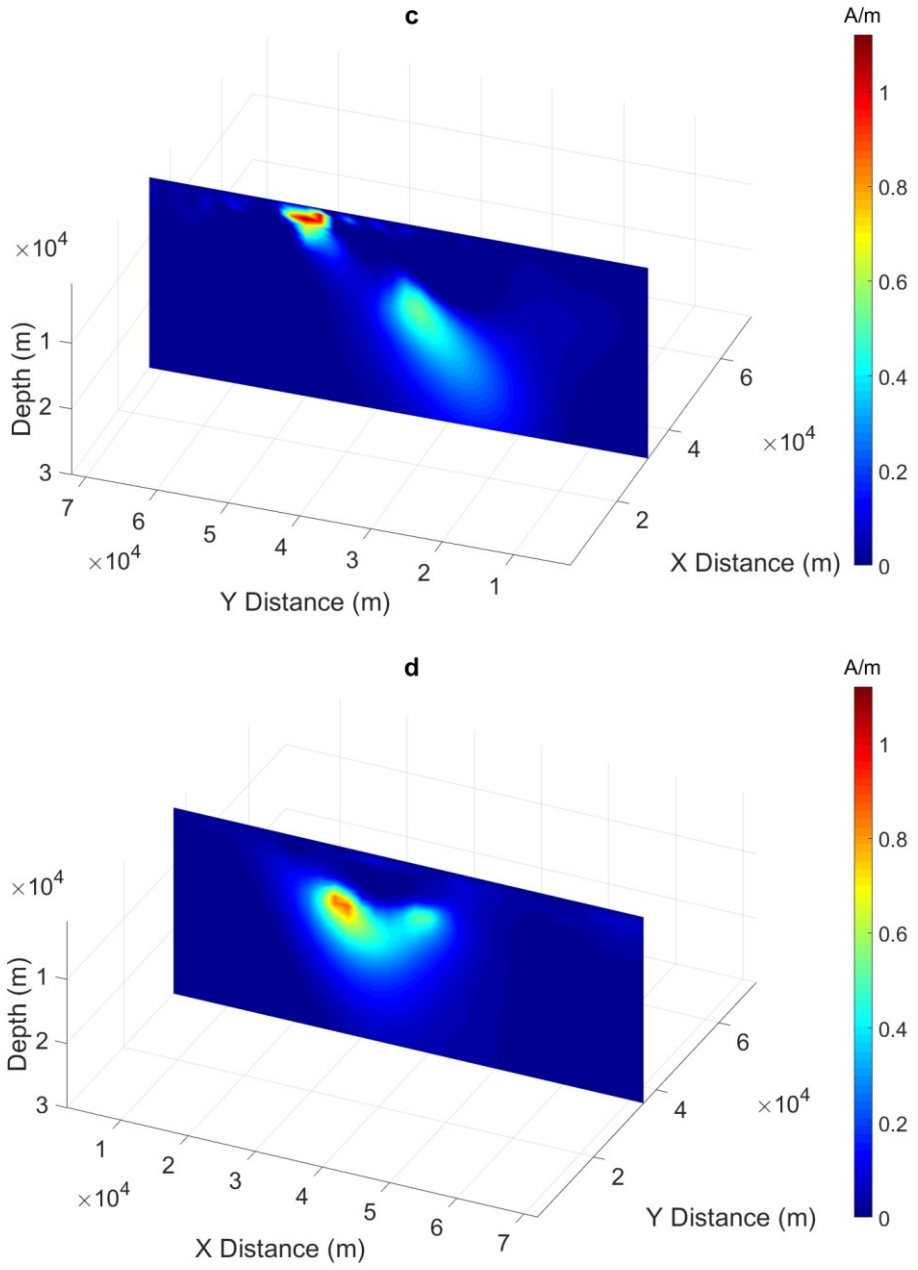

Figure 29.2: Model obtained (a and b) by using a homogeneous depth weighting function with β = 3, and (c and d) by using an inhomogeneous depth weighting function, with β(x,y,z) as shown in Figure 28c. The slices are referred to the black dashed lines in Figure 28b

Figure 29 shows the source model obtained by using the two different approaches; the vertical slice corresponds to the black dashed line in Figure 28b.

The results of both models are in good agreement with those obtained by Cella and Fedi (2012). The main difference is that we did not apply any filter to the original data to obtain estimates of β of the two main sources, as they did.

Moreover, it is glaring that using an inhomogeneous depth weighting it is possible to collect more solid information about the distribution in the subsurface of the magnetization (or

density in the gravity case). In fact, looking at the vertical section in figure 29.2 the two sources are described very well and they are both collocated at reasonable depths, as it results surely for the shallow source which now realistically characterizes the Mt. Vulture volcano. On the contrary, using a constant value of 3 for the depth weighting exponent (figure 29.1), we are not obtaining a very good information about the deepest source and the shallower source is surely too deep, being the mt. Vulture an outcropping volcanic structure.

We can conclude that this new approach brings two main advantages on inversion of potential fields:

1) there is no need to filter the dataset in order to separate different wavelength component and analyse those separately, instead it is possible to retrieve information about the different sources directly at the same time by performing only one inhomogeneous depth weighted inversion;

2) sources with different geometry, that should have different structural indices, are treated at the same time without the need of performing separated inversion processes with different constant depth weighting exponent.

7. Conclusions

We developed two different inversion methods of potential fields, based on a multiscale approach, that is they involve the inversion of data at different scales or altitudes. This is a not common approach in inversion of potential fields, but we proof that the insight of multiscale fields could help to retrieve better information about the distribution of physical properties in the subsurface.

We have described a 1D method for inverting potential field data, which has several aspects of interest. One relevant feature is that it is, to my knowledge, the only one allowing 1D inversion of potential fields.

At the moment the method will produce an approximate characterization of the underground source distribution, which should be better interpreted with more refined 2D/3D algorithms. However, our examples show the usefulness of producing this kind of source distribution model. The main difficulty is to have a good estimate of the horizontal dimensions of the source, necessary for building a reasonable model volume and we tried to outline a valid strategy for its estimation based on two steps:

1) boundary analysis, to have our first estimate of the source extent;
2) a Markov chain approach, to search for the optimal value of the horizontal extent along the strike-length direction, which yields the best data misfit for each sounding.

Once both conditions are relatively well satisfied for the whole depth extent of the source, bounds for the density constraints are not critical and wide bounds may be safely adopted.

Considering that these soundings are built through upward-continued data, the second problem is due to continuation errors, which increase versus the altitude. A rather good strategy to alleviate this error is subtracting to each sounding a third-order polynomial function of the altitude. Synthetic cases of a single buried body provided good results for either the geometry and the density contrast of the source, even if we use upward-continued data and relatively wide bounds for the density.

We tested this new method on synthetic case of a single buried body and a real case of a sedimentary basin in the USA (Frenchman Flat basin, Nevada), obtaining good results, also having used wide bounds for the density contrast.

The same 1D method was tested on two magnetic real cases for a joint interpretation. The integrated study of the results obtained by inverting the TDEM and the magnetic data separately

showed that not always the two methods have the same sensitivity with respect to the geological structures. In the case of the Broken Evil prospect (Ontario) the 1D inversion method solution fits the results conducted by another method with other dataset.

The inversion model is also in agreement with the information derived from a drill hole which confirms that the magnetic anomaly is due by graphitic sediments with seams and heavy disseminations of pyrrhotite. So, in this case, the use of the 1D method helps in increasing the confidence in the geophysical models.

About the Drybones kimberlite case (Northwest Territories), the 1D method revealed a different sensitivity to the geological structures. In this case the integration of the inverse models improved the interpretation of the area. All the geological structures at Drybones bay are well retrieved by the inversion processes and are in good agreement with the drill hole information available for this area.

About the 2D/3D inversion method developed in the second part of my PhD, it can certainly be said that the inhomogeneous approach improves the modelling of potential fields, adding a constraint that is entirely deducible from the data and not from a priori information.

This is a significant step forward, especially in the analysis of areas where there is no other information. It is a method that could be even more improved in the future, especially to adopt even more efficient mathematical/numerical tools for reducing the various instabilities during the estimation of the β.

The main difference compared to standard and standard (homogeneous) method resides in using a depth weighting function variable in its exponent, while in the homogeneous case it assumes a single constant value for the exponent in the whole subsurface volume. Our approach reflects the inhomogeneous nature of the homogeneity degree, for source distributions of potential fields, which cannot be characterized by a single value. Also, either integer or fractional values of the homogeneity degree are accepted, according to recent research (Fedi et al., 2015).

The approach was tested on 2D and 3D sinthetic data, for perfect or noisy data, showing a better respose compared to standard methods that are using a homogeneous approach: density/magnetization estimates and the depth resolution are more consistent compared to the standard approach.

Then two 3D real cases were studied, shown the advantage of using an inhomogeneous approach to recover a realistic information of the subsurface density and magnetization distributions.

For the gravity case of an impact site (Vredefort), the inhomogeneous depth weighting function helps us to recover a better estimates of the bottom for both the sources, the inner

core of the stucture and the distal rings, that are consistent with the available geological and other geophysics information of the area.

Also for the Mt. Vulture magnetic anomaly, this new approach allows us obtaining a valid and realistic information on the source distribution, starting directly from the original data, that is without needing any kind of filtering to separate the components. This is clearly shown comparing our result with those of the standard inversion, which, for example, lead to the absurd result of a non-magnetized volcanic edifice. The distribution at large depth confirms the one obtaine by previous research, but in that case it was necessary to perform the inversion on low-pass filtered data.

Regards the computational time involved with this method, we did not find any sensitive difference between the two approaches, but it should be taken into account that in addiction to the inversion algorithm time, the estimation time of β should be added. However, the β estimation is not time consuming, if compared to that due to the inverison algorithm, especially when big dataset are involved.

Future prospectives for both methods could be:

1) optimization of the 1D method, using different solvers for the inversion process, with a possible deep learning adaptation.

2) optimization of the estimates of β by finding tools allowing even more stable results.

3) Probably, the most important feature of the method is that the constraints used to perform an inhomogeneous depth weighted inversion, i.e. the homogeneity degree n and the consequent inhomogeneous depth-weighting function, are estimated directly from the dataset and not obtained from other sources. This feature could be used to improve also algorithms of joint inversion of different geophysical quantities

Acknowledgements

First of all, I would like to express my sincere gratitude to my advisor professor Maurizio Fedi for the continuous support of my Ph.D. study and related research, especially for his patience and motivation.

I would like to express my sincere gratitude also to advisor professor Giovanni Florio for the advices and support during these years.

Simone Ialongo helped me in yielding his original Li-Oldenburg code, developed under his doctorate thesis, so that I was easily allowed to modify his code accordingly to my multiscale approach.

I would like to thank Ivano Pierri that helped me in yielding his code for the gravity polyhedron forward model used in the paragraph 6.1.

I thank Domenico di Massa for both the papers we have written together and that are also part of his Ph.D. thesis.

I also thank ENI for making available the Mt. Vulture aeromagnetic data, and Mike Dransfield and Fugro for making available the Vredefort gradient tensor dataset.

I want also sincerely to thank the professor Ettore Cardarelli and the other reviewer for the insightful comments and criticism that helped me to improve the final versions of this work.

APPENDIX A

We ran a sensitivity test on the 3D synthetic model described in paragraph 6.1.

Since the analytical expression of sensitivity is hard to be obtained, we turned to a numerical approach. So, we decided to study the model perturbations caused by applying a random perturbation to the estimates of β. We used the case of a polyhedron previously illustrated in Figure 13. So, we compared it against the model obtained by using a depth weighting function built with the perturbed values of β.

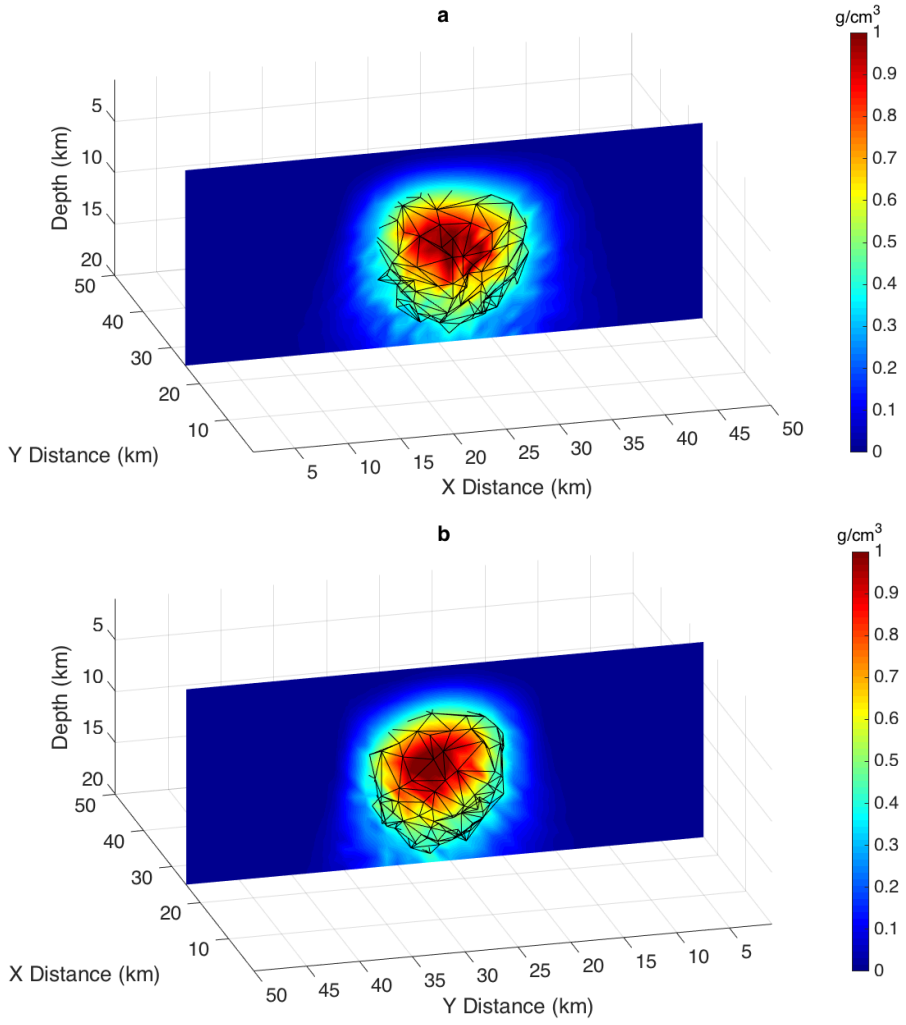

Figure A.1: (a) W-E slice and (b) N-S slice of the model using an inhomogeneous depth weighting function with β(x,y,z) perturbed by a random Gaussian noise with μ = 0.2 and σ = 1.

The perturbation was performed by adding to every estimate a Gaussian random noise with $\mu = 0.2$ *and* $\sigma = 1$; then the obtained values of β were adjusted according to fit the allowed range of 0 - 3. So, β lower then 0 were assigned to 0 and β higher then 3 were assigned to 3.

The new model obtained by the inversion process using the perturbed depth weighting exponent is giving the same information about the source, even if the solution seems to be a little bit noisy, compared to that described in paragraph 6.1.

Considering that the perturbation applied is pretty high, we can conclude that our approach is quite robust.

References

Barbosa, V. C. F., Silva, J. B. C., Medeiros, W. E., 1999, Stability analysis and improvement of structural index estimation in Euler deconvolution. *Geophysics*, 64, 48-60.

Barbosa V. C. F. & Silva J. B. C. , 1994. Generalized compact gravity inversion, *Geophysics*, 59, 57–68.

Barnes G. & Barraud J., 2012. Imaging geologic surfaces by inverting gravity gradient data with depth horizons. *Geophysics*, 77, G1–G11.

Bhattacharyya, B.K., 1964, Magnetic anomalies due to prism-shaped bodies with arbitrary polarization: *Geophysics* 29, 517-31.

Blakely, R.J., 1996, Potential theory in gravity and magnetic applications; Cambridge University Press, New York, 441 p.

Boon, J. D., and C. C. Albritton, 1937, Meteorite scars in ancient rocks. *Field lab*, 5-53.

Bott M. H. P., 1962, A Simple Criterion for Interpreting Negative Gravity Anomalies, *Geophysics*, VOL. XXVII, No. 3, P. 376-381.

Castaldo R., Fedi M., Florio G., 2014, Multiscale estimation of excess mass from gravity data, *Geophysical Journal International,* 197, 1387–1398.

Cella F., Fedi M. and Florio G., 2009, Toward a full multiscale approach to interpret potential fields: *Geophysical Prospecting* 57, 543–557.

Cella, F. and Fedi, M., 2012, Inversion of potential field data using the structural index as weighting function rate decay. *Geophysical Prospecting*. 60, 313-336.

Corner, B., Durrheim, R. J., and Nicolaysen, L. O., 1990, Relationships between the Vredefort structure and the Witwatersrand basin within the tectonic framework of the Kaapvaal craton as interpreted from regional gravity and aeromagnetic data: *Tectonophysics*, v. 171, p. 49–61.

Cribb J. B., 1976; Application of the generalized linear inverse to the inversion of static potential data. *Geophysics*, VOL. 41, no. 6, 1365-1369.

Dietz RS., 1961, Vredefort ring structure: meteorite impact scar? J. Geol. 69:499–516

Di Massa, D., Fedi, M., Florio, G., Vitale, A., Viezzoli, A., Kaminski, V., 2018, Joint interpretation of AEM and aeromagnetic data acquired over the Drybones kimberlite, NWT (Canada), *Journal of Applied Geophysics*, 158, 48-56

Fedi M., and Abbas M.A., 2013, A fast interpretation of self-potential data using the depth from extreme points method: *Geophysics*, 78, no. 2, E107-E116.

Fedi M. and Pilkington M., 2012: Understanding imaging methods for potential field data. *Geophysics*, 77, 1, G13-G24.

Fedi, M., Florio, G. and Paoletti, V., 2015, MHODE: a local-homogeneity theory for improved source-parameter estimation of potential fields, *Geophysical Journal International*, 202 (2): 887-900 doi:10.1093/gji/ggv185.

Fedi M., Cella F., Quarta T., Villani A., 2010, 2D continuous wavelet transform of potential fields due to extended source distributions. Appl. Comput. Harmon. Anal.; 28(3):320-337.

Fedi M. and Cascone L., 2011, Composite continuous wavelet transform of potential fields with different choices of analyzing wavelets. J. geophys. Res. 2011;116(B7). doi:10.1029/2010JB007882.

Fedi M., Cella F., Florio G. and Rapolla A., 2005. Multiscale derivative analysis of the gravity and magnetic fields of Southern Apennines (Italy). In: "CROP Project, Deep seismic exploration of the Central Mediterranean and Italy (Atlases in Geoscience, Volume 1)", I. Finetti, ed., Elsevier Science, 281-318.

Fedi, M., & Florio, G., 2001, Detection of potential fields source boundaries by enhanced horizontal derivative method. *Geophysical Prospecting*, 49(2001), 40–58.

Fedi M. and Florio G., 2006, SCALFUN: 3D analysis of potential field scaling function to determine independently or simultaneously Structural Index and depth to source. *76° SEG Annual Meeting, New Orleans*, 1-6 October, 2006, pp. 963-967.

Fedi, M., Rapolla, A., 1993. I metodi gravimetrico e magnetico nella geofisica della Terra solida, Liguori Editore, 322 pp.

Fedi, M., Rapolla, A., Vertical Gravity an Magnetic Soundings: forward problem formulation and data inversion, *Bollettino di*

Geofisica Teorica ed Applicata, Vol.XXXVII, N.147 – September 1995.

Fedi, M., 2007, DEXP: a fast method to determine the depth and the structural index of potential fields sources. *Geophysics* 72, I1-I11.

Fedi, M., Florio G., Paoletti, V., 2012, Local homogeneity of potential fields and fractional homogeneous functions: a new theory for improved source parameter estimation, *82° SEG Annual Meeting, Las Vegas*.

Florio G., Fedi M., Cella F. & Rapolla A., 1999, The Campanian Plain and Phlegrean Fields: structural setting from potential field data, *Journal of Volcanology and Geothermal Research*, 91, 361–379.

Florio G., Fedi M., Rapolla A., 2009, Interpretation of regional aeromagnetic data by the scaling function method: the case of Southern Apennines (Italy). *Geophysical Prospecting*, 57, 479-489.

Gerovska, D., Stravrev, P., Araúzo-Bravo, M. J., 2005, Finite-difference Euler Deconvolution Algorithm Applied to the Interpretation of Magnetic Data from Northern Bulgaria, *Pure and applied geophysics*, 162, n°3, 591-608.

Gibson, R.L., and Reimold, W.U., 2000, Deeply exhumed impact structures: a case study of the Vredefort Structure, South Africa. In: Gilmour, I., Koeberl, C. (Eds.).

Gibson, R.L., and Reimold, W.U., 2001, The Vredefort impact structure, South Africa (the scientific evidence and a two-day excursion guide), Counc. Geosci., Pretoria, Mem, 92 (111 pp.).

Gibson, R.L., Reimold W. U., Ashley A. J., Koeberl C., 2002, Metamorphism on the Moon: A terrestrial analogue in the Vredefort dome, South Africa?: Geology, 30, 475-478.

Gill, P. E., Murray, W., Ponceleon, D. B., and Saunders, M., 1991, Solving reduced KKT systems in barriermethods for linear and quadratic programming. Technical Report SOL 91–7, Stanford University. Kearey P., Brooks M. and Hill I., 2002, An Introduction to Geophysical Exploration. Blackwell Publishing, Oxford.

Grieve, R. A. F., and A. Therriault, 2000, Vredefort, Sudbury, Chicxulub: Three of a kind? *Annual Review of Earth Planetary Science*, 28: 305-338.

Guillen A. & Menichetti V., 1984. Gravity and magnetic inversion with minimization of a specific functional, *Geophysics*, 49, 1354–1360.

Hart, R. J., Andreoli, M. A. G., Tredoux, M., and De Wit, M. J., 1990, Geochemistry across an exposed section of Archaean crust at Vredefort, with implications for mid-crustal discontinuities: *Chemical Geology*, v. 82, p. 21–50.

Hart, R.J., Hargraves, R.B., Andreoli, M.A.G., Tredoux, M., and Doucoure , C.M., 1995. Magnetic anomaly near the center of the Vredefort structure: implications for impact related magnetic signatures: *Geology* 23, 277– 280.

Henkel, H., and Reimold, W.U., 1996, Integrated gravity and magnetic modeling of the Vredefort impact structure—reinterpretation of the Witwatersrand basin as the erosional remnant of an impact basin: *Econ. Geol. Res. Unit Inf. Circ.*, vol. 299. University of the Witwatersrand, Johannesburg. 89 pp.

Henkel, H., and Reimold, W.U., 1998, Integrated geophysical modeling of a giant, complex impact structure: anatomy of the Vredefort Structure, South Africa, *Tectonophysics* 287, 1– 20.

Ialongo S., Fedi M., Florio G., 2014, Invariant models in the inversion of gravity and magnetic fields and their derivatives, *Journal of Applied Geophysics*, v.110, p.51-62

Ialongo S., 2014, Depth resolution in potential field inversion: theory and applications, *PhD Thesis*

Kamo, S.L., Reimold, W.U., Krogh, T.E., and Colliston, W.P., 1996, A 2.023 Ga age for the Vredefort impact event and a first report of shock metamorphosed zircons in pseudotachylitic breccias and granophyre: *Earth and Planetary Science Letters*, v. 144, p. 369–388.

Keating P. & Pilkington M., 2004, Euler deconvolution of the analytic signal and its applicationto magnetic interpretation, Geophysical Prospecting, 52, 165–182.

Last B.J. & Kubik K., 1983, Compact gravity inversion, Geophysics, 48, 713–721.

Li, Y. and Oldenburg, D. W., 1996, 3-D inversion of magnetic data. Geophysics, 61, no. 02, 394-408.

Li Y., and Oldenburg D., 1998, 3D inversion of gravity data: Geophysics, 63, 109– 119.

Li Y., and Oldenburg D., 2003, Fast inversion of large-scale magnetic data using wavelet transform and logarithmic barrier method: Geophysical Journal International, 152, 251-265.

Martinez C., Li Y., 2011, Inversion of regional gravity gradient data over the Vredefort Impact Structure, *South Africa: 81st Annual Meeting, SEG*, Expanded Abstract.

McCarthy, T. S., I. G. Stanistreet, and L. J. Robb, 1990, Geological studies related to the origin of the Witwatersrand Basin and its mineralization: an introduction and a strategy for research and exploration: *South African Journal of Geology*, 93, 1-4.

Menke, W., 1984, Geophysical data analysis: Discrete inverse theory; Academic Press (Elsevier).

Phelps G. A. & Graham S. E., 2002. Preliminary gravity inversion model of Frenchman Flat basin, Nevada Test Site, Nevada, U.S. *Geological Survey Open-File Report* 02-363.

Reid, A. B., J.M.Allsop, H. Granser, A. J. Millett, and I.W. Somerton, 1990, Magnetic interpretation in three dimensions using Euler deconvolution: *Geophysics*, 55, 80–91.

Reimold, W.U., and Gibson, R.L., 1996, Geology and evolution of the Vredefort impact structure, South Africa: *J. S. Afr. Earth Sci*. 23, 152– 162.

Reynolds J. M., 1997, An introduction to applied and environmental geophysics, John Wiley & Sons Ltd, Chichester, West Sussex.Sailhac, P.

Sen, M. K., and Stoffa, P. L., 1991, Global Optimization Methods in Geophysical Inversion, Cambridge.

Silva J.B.C. & Barbosa V.C.F., 2006. Interactive gravity inversion, Geophysics, 71, J1–J9.

Vadim A. Litinsky, 1989, Concept of effective density: Key to gravity depth determinations for sedimentary basins, Geophysics, Vol. 54, No. 11; P. 1474-1482.

Vitale, A., Di Massa, D., Fedi, M., Florio, G., 2018, A method for inversion of 1D vertical soundings of gravity anomalies, *Geophysics*, Vol.83, No.2, P.G15-G23

Wijns, C. & Kowalczyk, P., 2007. Interactive geophysical inversion using qualitative geological constraints, *Exploration Geophysics*, 38, 208–212.